University of South Florida
Scholar Commons

6-1-2009

Digital holography applications in ophthalmology, biometry, and optical trapping characterization

Mariana Camelia Potcoava
University of South Florida

Digital Holography Applications in Ophthalmology,

Biometry, and Optical Trapping Characterization

by

Mariana Camelia Potcoava

A dissertation submitted in partial fulfillment
of the requirements for the degree of
Doctor in Philosophy
Department of Physics
College of Arts and Sciences
University of South Florida

Major Professor: Myung K. Kim, Ph.D.
Dennis K. Killinger, Ph.D.
Martin Muschol, Ph.D.
George S. Nolas, Ph.D.
David W. Richards, Ph.D.

Date of Approval:
June 12, 2009

Keywords: Three-dimensional tomography, digital interference holography, retina, fingerprinting, optical tweezers, Gabor holography

Dedication

To my family.

Acknowledgements

There are many people to whom I owe gratitude and I hope I have included all of them below. First and foremost I am indebted to my advisor Dr. Myung K. Kim who gave me the opportunity to work on very challenging experiments. Under his guidance I have learned about digital holography, digital interference holography (DIH), wavelength scanning, optical coherence tomography (OCT), optical trapping, and developed optical imaging instrumentation requiring the integration of various electro-optic subsystems to probe new physics.

I would especially like to thank the people who worked closely with me on the DIH project within the last two years: Dr. David Richards, Christine Kay, and Dr. Curtis Margo from the Ophthalmology department at USF. This thesis would not have been possible but for their help.

I wish to thank all of my committee members, Dennis Killinger, Martin Muschol, George Nolas, and David Richard, for their comments. I especially thank Dr. Richards for all of his suggestions, kind encouragement to write grant proposals. Thanks are also due to the support of Dr. Kim for signing all documents related to the grant proposals submission. I greatly appreciate all of them help in proofreading the final copy of this thesis, as well. I would also like to thank Dr. Manoug Manougian for chairing my defense examination.

I also thank to Dr. Hwang from NIST for valuable discussions about the dynamical imaging of erythrocytes.

I would like to thank the whole DHML group members who were working on various other experiments in the lab and with me at the same time. These members are Leo Krzewina, Lingfeng Yu (Frank), Christopher Mann, Nilanthi Warnasooriya, Alexander Khmaladze, and William Ash.

Thanks are also due to the support staff at USF; their help over the years was invaluable.

Much thanks to my dear friends Mihaela Popa-McKiver and Richard McKiver for their real help when it was needed.

Finally, I owe special gratitude to my family members for their constant love and support: To my father for his hard work in choosing good schools for me, to my mom, and my sister who were always there for me, to my husband George, for all his kind support, encouragement, and to my daughter, Ana - Karina, for the joy she brings.

TABLE OF CONTENTS

LIST OF FIGURES

vii

Digital Holography Applications in Ophthalmology,

Biometry, and Optical Trapping Characterization

Mariana Camelia Potcoava

ABSTRACT

This dissertation combines various holographic techniques with application on the two- and three-dimensional imaging of ophthalmic tissue, fingerprints, and microsphere samples with micrometer resolution.

Digital interference holography (DIH) uses scanned wavelengths to synthesize short-coherence interference tomographic images. We used DIH for in vitro imaging of human optic nerve head and retina. Tomographic images were produced by superposition of holograms. Holograms were obtained with a signal-to-noise ratio of approximately 50 dB. Optic nerve head characteristics (shape, diameter, cup depth, and cup width) were quantified with a few micron resolution (4.06 $-4.8\,\mu m$). Multiple layers were distinguishable in cross-sectional images of the macula. To our knowledge, this is the first report of DIH use to image human macular and optic nerve tissue.

Holographic phase microscopy is used to produce images of thin film patterns left by latent fingerprints. Two or more holographic phase images with different wavelengths

are combined for optical phase unwrapping of images of patent prints. We demonstrated digital interference holography images of a plastic print, and latent prints. These demonstrations point to significant contributions to biometry by using digital interference holography to identify and quantify Level 1 (pattern), Level 2 (minutia points), and Level 3 (pores and ridge contours).

Quantitative studies of physical and biological processes and precise non-contact manipulation of nanometer/micrometer trapped objects can be effectuated with nanometer accuracy due to the development of optical tweezers. A three-dimensional gradient trap is produced at the focus position of a high NA microscope objective. Particles are trapped axially and laterally due to the gradient force. The particle is confined in a potential well and the trap acts as a harmonic spring. The elastic constant or the stiffness along any axis is determined from the particle displacements in time along each specific axis. Thus, we report the sensing of small particles using optical trapping in combination with the digital Gabor holography to calibrate the optical force and the position and of the copolymer microsphere in the x, y, z direction with nm precision.

CHAPTER 1

GENERAL INTRODUCTION

This chapter presents a brief history of holography and an overview of existent imaging techniques for biomedical optics, biometry, and optical trapping. A brief review of holography and three-dimensional imaging is presented in Section 1.1. Ophthalmic imaging devices overview and the structure of the retina are given in Section 1.2. In Section 1.3 fingerprint characteristics and biometry imaging techniques designated for fingerprint imaging are presented. Optical trapping imaging and the relation to holography are described in Section 1.4. The motivation for this research and a summary of the original contributions in this dissertation are presented in Section 1.5. Finally, Section 1.6 outlines the organisation of this thesis.

1.1 Holography and Three-Dimensional Imaging

The principle of holography was introduced by Denis Gabor [1] in 1948, as a technique where wavefronts from an object were recorded and reconstructed in such a way that not only the amplitude but also the phase of the wave field were recovered. Gabor called this interference pattern a „hologram", from the Greek word "holos'‘-the whole, because it contained the whole information, the entire three-dimensional wave field as amplitude and phase. In 1967, J. Goodman demonstrated the feasibility of

1

numerical reconstruction of holographic images using a densitometer-scanned holographic plate [2]. Schnars and Jueptner, in 1994, were the first to use a CCD camera connected to a computer as the input, completely eliminating the photochemical process, in what is now referred to as digital holography [3–5]. Various useful and special techniques have been developed to enhance the capabilities and to extend the range of applications. Phase-shifting digital holography allows elimination of zero-order and twin-image components even in on-axis arrangement [6-8]. Optical scanning holography can generate holographic images of fluorescence [9]. Three-channel color digital holography has been demonstrated [10]. Application of digital holography in microscopy is especially important, because of the extremely narrow depth of focus of high-magnification systems [11, 12]. Numerical focusing of holographic images can be accomplished from a single exposed hologram. Direct accessibility of phase information can be utilized for numerical correction of various aberrations of the optical system, such as field curvature and anamorphism [13].

Digital holography has been particularly useful in metrology, deformation measurement, and vibrational analysis [14-16]. Microscopic imaging by digital holography has been applied to imaging of microstructures and biological systems [14, 17-18]. Digital interference holography for optical tomographic imaging [19-24], as well as multiwavelength quantitative phase contrast digital holography for high resolution microscopy [25-28], was demonstrated.

1.2 Ophthalmic Imaging

Examples of noninvasive ocular imaging technologies are scanning laser polarimetry (Retinal Nerve Fiber Analyzer GDx), [29, 30], confocal scanning laser tomography (Heidelberg Retinal Tomograph) [31], and optical coherence tomography (OCT), [29-44]. For purposes of this discussion, OCT will be described in order to serve as a comparison to our technology, digital interference holography (DIH). OCT is a non-contact, non-invasive optical imaging technique that uses a low-coherence source to determine the retinal thickness and to image optic nerve by means of cross-sectional images. OCT is probably the most significant development in ophthalmic imaging in the past decade [32-36]. The most basic form of OCT, time domain OCT (TDOCT), is based on the interference of low coherence light in a Michelson interferometer, and the reference mirror mechanically moves in order to scan the z axis. TDOCT generates an interference signal only when the reference mirror is at the same distance as the object's reflecting surface. The distances need to match within the coherence length of the light, which therefore determines the axial resolution. OCT uses a low coherence, i.e. broadband, light source, such as a tungsten lamp or superluminescent diode (SLD). OCT is used in clinical practice to create cross-sectional images of in vivo retina at a resolution of approximately 10-15 microns, taking advantage of the fact that various layers of the retina vary in their reflectivity [44]. The highest reflection occurs in layers of the retina with cell surfaces and membranes. This includes the internal limiting membrane and the retinal pigment epithelium (RPE). Less reflective layers include the inner and outer nuclear layers. OCT imaging has become an important tool in the imaging and evaluation of retinal cross-sectional anatomy, allowing retinal specialists to diagnose diseases such

as epiretinal membrane and macular hole, and to monitor conditions such as macular edema with objective measurements. It also supplies reproducible estimates of retinal thickness with accuracy not previously possible. New developments in OCT, with resolution under $10 \mu m$, include spectral-domain OCT (SD-OCT), where the mechanical z-scanning of the TDOCT is replaced with spectral analysis, and swept-source OCT (SS-OCT), where the spectral analysis is replaced with wavelength scanning of the light source [37-43]. An axial resolution of 1-2 μm has been reported using a femtosecond laser [39]. TDOCT provides the necessary resolution, but images are two dimensional only. The newer developments of FDOCT and SSOCT can now generate B-scan (cross-sectional) images at video rate, but to image one square centimeter of the posterior pole of the retina without interpolation, at least 1000 linear OCT scans are required, and these have to be re-assembled by computer to give a 3D volume image.

In our lab [45], this method was demonstrated for surface and sub-surface imaging of biological tissues, based on the principle of wide field optical coherence tomography (WFOCT) and capable of providing full-color three-dimensional views of a tissue structure with about 10 μm axial resolution, about $100 \sim 200$ μm penetration depth, and $50 \sim 60$ db dynamic range. WFOCT technique is similar to OCT, but without x-y scanning provides full color information. Also, the experiments were performed in three color channels (3 LED, red, blue, green) and the results were combined to generate the contour and the tissue structures of the specimen in their natural color.

Digital Interference Holography (DIH) technique is based on an original numerical method developed in DHM Laboratory of the Physics Department at USF,

where a three-dimensional microscopic structure of a specimen can be reconstructed by a succession of holograms recorded using an extended group of scanned wavelengths. DIH technology will be explained more elaborately in Chapter 3.

1.2.1 Structure of the Retina

Glaucoma is a group of eye diseases where vision is lost due to damage of the optic nerve. More precisely, the pathologic process results in the loss of retinal ganglion cells and their axons in the retinal nerve fiber layer resulting in thinning of the retinal nerve fiber layer (RNFL), [46, 47] . A yellowish white ring surrounding the optic disk, indicating atrophy of the choroid in glaucoma is called glaucomatous. Measurement of macular thickness is not only important in the diagnosis and monitoring of macular diseases; it has also been found to be useful in evaluating glaucomatous changes since up to seven layers of retinal ganglion cells are located at the macula, [48, 49]. In Figure 1.1A, from top to bottom, the layers are**:** Inner Limiting Membrane, Nerve Fiber Layer, Ganglion Cell Layer, Inner Plexiform Layer, Inner Nuclear Layer, Outer Plexiform Layer, Outer Nuclear Layer, Inner and Outer Segments of Photoreceptors, Retinal Pigment Epithelium, and Choroid. The ganglion cell layer is the layer with dark red nuclei (second blue arrow from the top). Another arrangement of the retinal layers, showing the basic circuitry of the retina, is illustrated in Figure.1.1B and Figure 1.1C [50]. OCT cannot image these nuclei. The best that current OCT can do is measure the thickness of the "ganglion cell complex", which consists of the top three layers (top 3 blue arrows of Figure 1.1A). Adaptive optics cannot do it either. For the diagnosis and management of glaucoma, we would like to have maps of the density of ganglion cells as

function of location in the back of the eye. The challenge for the future will be to develop a 3D imaging technology to identify what percent of cells are lost due to the retinal damage.
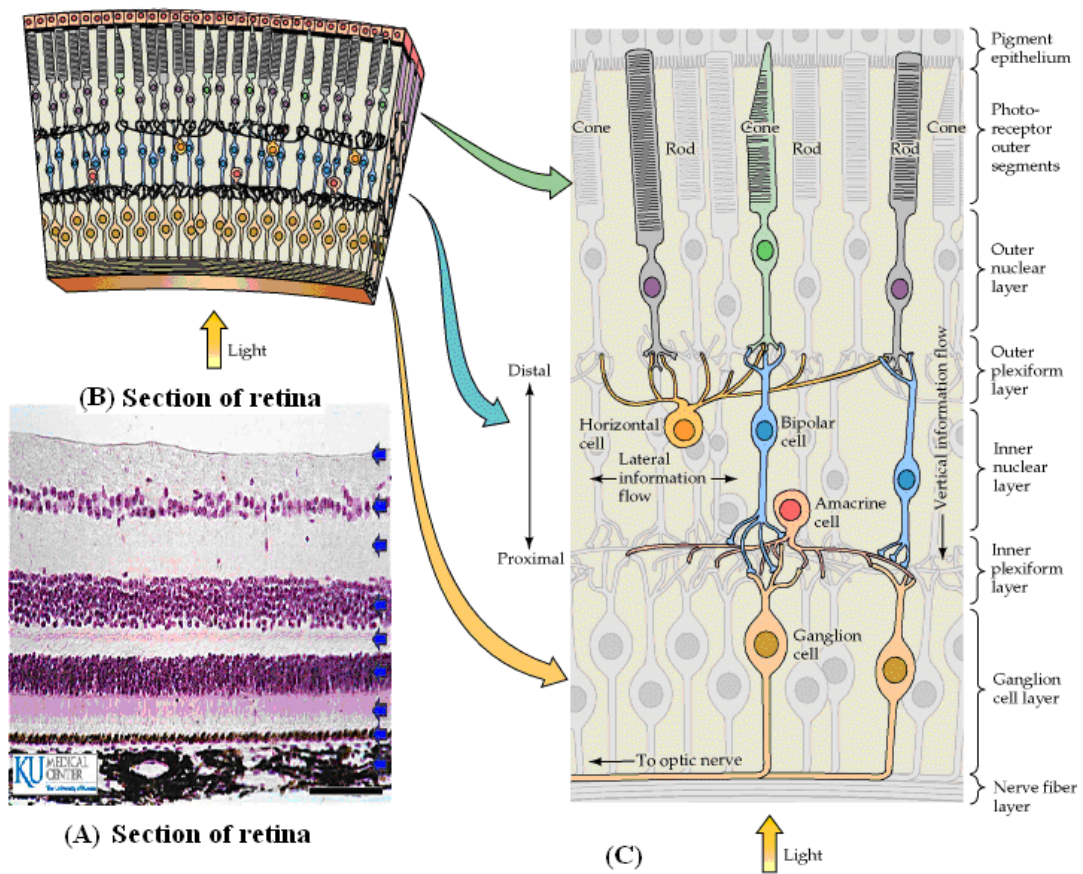
Figure 1.1. Structure of the Retina. (A) Section of retina (Kansas University, Medical Center), (B) Section of the retina showing overall arrangement of retinal layers. (C) Diagram of the basic circuitry of the retina. A three-neuron chain—photoreceptor, bipolar cell, and ganglion cell—provides the most direct route for transmitting visual information to the brain. Horizontal cells and amacrine cells mediate lateral interactions in the outer and inner plexiform layers, respectively. The terms *inner* and *outer* designate relative distances from the center of the eye (inner, near the center of the eye; outer, away from the center, or toward the pigment epithelium).

6

1.3 Biometry Imaging

Available biometric technologies rely on the recognition of DNA residue, face, voice, iris, signature, hand geometry, and fingerprints. Depending on the complexity of the sensing method, these technologies may be classified in terms of accuracy, simplicity, acceptability, and as well as stability. One of the simplest and most acceptable human authentification methods is fingerprint recognition. Ancient Babylonian and Chinese civilizations used the fingerprint impressions as a method to sign documents. Later in the 1880's, the first fingerprint considerations were published by Henry Faulds in Nature [51]. He collected fingerprints from different nationalities and made the conclusion that the copy of the forever unchangeable finger furrows may assist in the identification of criminals. After a few years of experimental work, the Galton-Henry system of fingerprint classification was published and quickly introduced in the USA in 1901 for criminal-identification records [52].

Fingerprint recognition systems can be classified in four main methods as follows: ink-technique, solid-state, ultrasonic, and optical. The traditional ink technique is based on using liquids and powder to enhance the contrast of the prints template [53]. The solid- state sensors method uses an array of sensing elements such as: pyro-electric material (thermal-type), piezoelectric material (pressure-type), or capacitor electrodes (capacitance-type) covered with a hard protective layer. For example, the thermal-type sensing technique is based on the temperature differences between the surface of the finger (ridges/ valleys) and each thermo-element sensor. The temperature difference data is read by a sensor that performs an 8-bit analog-to-digital (AD) conversion to output an image of the fingerprint. The cross-sectional reconstruction of a silicone rubber

fingerprint model was performed with a valley width of 100 μm and a height of 50 μm [54]. Ultrasonic scanners [55], use sound waves to see through skin fat and tissue. The difference in acoustic impedance between the finger pattern and the plate is obtained and the echo signal is recorded by the receiver and transformed into ridge depth data. This technology allows creating images of difficult prints because the quality of the images is not affected by the dirt, grease, and grime. Fingerprint sensing by optical sensors has been used since 1970. The first optical sensor was based on the total internal reflection (TIR). The finger is illuminated through a prism and a reflectance profile of the object is built based on reflected light from the fingerprints. For instance, the LightPrint[TM], developed by Lumidigm, uses an optical sensor based on TIR. The skin layers are scanned by a range of wavelengths to improve the quality of the images due to different skin condition and to improve spoofing protection of the scanners [56]. An application of optical polarization was demonstrated [57] to enhance the visibility of the latent fingerprint without using any chemical treatment. A novel optical coherence tomography-based system was demonstrated for depth-resolved 2-D and 3-D imaging to provide information of both artificial and natural ridge and furrow patterns simultaneously [58-60]. More recently, another scanner, full-field swept-source optical coherence tomography, uses a combination of a superluminescent broadband light source and an acousto-optic tunable filter. The light source is tuned to operate at different wavelengths. This scanner was used in forensic science to image the three-dimensional structure of latent fingerprints [61-63].

1.3.1 Fingerprint Patterns

Features of fingerprints can be classified in three levels [53, 64-69]. Level 1 feature refer to the pattern type, such as arch, tented arch, left loop, right loop, double loop, and whorl. Level 2 features are formed when the ridge flow is interrupted by some irregularities, known as minutiae. Examples of minutiae are bifurcation, ending, line-unit, line-fragment, eye, and hook. Level 3 features include other dimensional characteristics like pores, creases, line shape, incipient ridges, scars, and warts.

1.4 Optical Trapping Imaging

Matter-light interaction reveals physical phenomena and object characteristics by monitoring optically trapped object fluctuations about equilibrium. Optical trapping microscopes can be classified by function of the illumination method, optical trapping schemes, optical detection modes, and applications. Position -tracking algorithms and trapping light (laser) are integral part of the applications and they are chosen as a function of the object being characterized.

Commercial optical trapping systems are preferable due to the flexibility to be attached to any microscope arm, but home-made systems are more convenient giving possibility to upgrade the system easily at a low cost.

Starting from a simple configuration, one or two trapping laser beams [70-72] to cool and trap neutral atoms, the optical trapping systems have become sophisticated devices. The invention of laser and the ability to control object position applying picoNewton forces have found applications in physics and biology.

The main use for the optical trap is the manipulation of biological structures to study molecular motors and the physical properties of DNA [73, 74]. Optical sorting tweezers use an optical lattice to sort cells by size and by refractive index [75, 76]. The evanescent field and more recently surface plasmon waves propel microparticles along their propagating path [77, 78]. Optofluidics is a joint technology between microfluidics and micro-photonics. Optical control of the microfluidic elements using optical tweezers was also reported [79]. Another application of optical trapping techniques includes integrated lab-on-a-chip technologies where optical force landscapes are highly desirable to manipulate multiple microparticles in parallel [80].

Position detection, trapping beam alignment and high NA microscope are the most challenging parts of the trapping system. The position detection [81] is possible using: video-based position detection (CCD) [82, 83], imaging position detection (QPD), laser based-position detection (QPD and back-focal laser beam), and axial position detection technologies. The video-based position detection is limited due to unavailability of a camera with high video acquisition rates. The benefit of this method is that the trapped sample can be imaged onto a CCD camera and make it desirable holography uses.

1.5 Research Contribution

The motivation of this work has been to develop and characterize optical imaging instruments for ophthalmology, biometry, and optical trapping, based on the latest development of digital holography.

My early work focused primarily on developing a retinal scanner, based on Digital Interference Holography. The development of this instrument requires electro-optic system integration including software development, as well as an understanding of biological specimens' behavior, morphology, and physiology. Holograms acquisition, optical field reconstruction, and optical field superposition programs were developed to characterize the sample under study. This instrument uses high-speed, non-contact, non-invasive technology, has no mechanical moving parts, has an axial resolution better than 5 μm, and signal-to-noise ratio (SNR) of about 50 dB. To achieve these characteristics, the calibration scheme was modified by introducing a phase-matching technique that accounts for the dispersion in the system. A phase variable was introduced that minimizes the errors resulting from phase mismatch.

Calibration experiments using a resolution target demonstrates improvement of SNR with increasing number of holograms consistent with theoretical prediction. Imaging experiments on pig retinal tissue reveal topography of blood vessels as well as optical thickness profile of the retinal layer [84, 94]. We reported for the first time the use of DIH to image human macular and optic nerve tissue [85-93, 95, 96]. This might be of significance to researchers and clinicians in the diagnosis and treatment of many ocular diseases, including glaucoma and a variety of macular diseases.

DIH also offers phase unwrapping capability. By choosing appropriate wavelengths, the beat wavelength can be made large enough to cover the range of optical thickness of the object being imaged. Together with various techniques such as low coherence tomography and digital holography microscopy, we also demonstrated the use of DIH for imaging fingerprints [86].

11

Most recently, I have focused primarily on the design and characterization of holographic optical tweezers for trapping and manipulating microspheres undergoing Brownian motion [87]. Hologram acquisition, optical field reconstruction, particle tracking, and statistics programs were developed to characterize the trapped particle. The future goal of this project is to develop a new tool to study how cells ingest foreign particles through the process known as phagocytosisa or to understand a variety of biophysical processes.

1.6 Thesis Organization

This dissertation is organized in the following way. Chapter 2 presents scalar field theory and discusses the reconstruction of the optical field by the angular spectrum and the Fresnel approximation. Chapter 3 discusses in more detail the theoretical background of the digital interference holography, the experimental apparatus, and calibration. Chapter 4 covers the optimization methods of the digital interference holography system. In Chapter 5, the in-vitro imaging of ophthalmic tissue by digital interference holography is presented. The application of digital interference holography in biometry is presented in Chapter 6. The digital Gabor holography microscope together with the optical trapping apparatus is described and experimental results are presented in Chapter 7. Major conclusions and future directions are summarized in Chapter 8.

1.7 Bibliography

[1] Gabor D 1971 Holography *Nobel Lecture*

http://nobelprize.org/nobel_prizes/physics/laureates/1971/gabor-lecture.pdf

[2] Goodman J W and Lawrence R W 1967 Digital image formation from electronically detected holograms *Appl. Phys.Lett.* **11** 77-79

[3] Schnars U 1994 Direct phase determination in hologram interferometry with use of digitally recorded holograms *J. Opt. Soc. Am*. A **11** 2011-5

[4] Schnars U and Jueptner W 1994 Direct recording of holograms by a CCD target and numerical reconstruction *Appl.Opt.* **33** 179–181

[5] Schnars U and Jueptner W 2002 Digital recording and numerical reconstruction of holograms *Meas. Sci. Technol.* **13** R85-R101

[6] Yamaguchi I, Kato J, Ohta S and Mizuno J 2001 Image formation in phase-shifting digital holography and applications to microscopy *Appl. Optics* **40** 6177-86

[7] Yamaguchi I and Zhang T Phase-shifting digital holography 1997 *Opt. Lett*. **22** 1268

[8] Zhang T and Yamaguchi I 1998 Three-dimensional microscopy with phase-shifting digital holography *Opt. Lett.* **23** 1221

[9] Poon T C 2003 Three-dimensional image processing and optical scanning holography *Adv. Imaging & Electron Phys*. **126** 329-50

[10] Yamaguchi I, Matsumura T and Kato J 2002 Phase-shifting color digital holography *Opt. Lett*. **27** 1108

[11] Barty A, Nugent K A, Paganin D and Roberts A 1998 Quantitative optical phase microscopy *Opt. Lett*. **23** 817

[12] Cuche E, Bevilacqua F and Depeursinge C 1999 Digital holography for quantitative phase-contrast imaging 1999 *Opt. Lett*. **24** 291

[13] Ferraro P, De Nicola S, Finizio A, Coppola G, Grilli S, Magro C and Pierattini G 2003 Compensation of the inherent wave front curvature in digital holographic coherent microscopy for quantitative phase-contrast imaging *Appl. Opt.* **42** 1938-46

[14] Xu M L, Peng X, Miao J and Asundi A 2001 Studies of digital microscopic holography with applications to microstructure testing Appl. Opt. 40 5046-51

[15] Pedrini G and Tiziani H J 1997 Quantitative evaluation of two-dimensional dynamic deformations using digital holography *Opt. Laser Technol*. **29** 249–56

[16] Picart P, Leval J, Mounier D and Gougeon S 2005 Some opportunities for vibration analysis with time averaging in digital Fresnel holography *Appl. Opt*. **44** 337–43

[17] Haddad W S, Cullen D, Solem J C, Longworth J W, McPherson A, Boyer K and Rhodes C K 1992 Fourier-transform holographic microscope *Appl. Opt.* **31** 4973-8

[18] Xu W, Jericho M H, Meinertzhagen I A and Kreuzer H J 2001 Digital in-line holography for biological applications *Proc. Natl. Acad. Sci. USA* **98** 11301-05

[19] Kim MK 1999 Wavelength scanning digital interference holography for optical section imaging *Opt. Letters* **24** 1693

[20] Kim MK 2000 Tomographic three-dimensional imaging of a biological specimen using wavelength-scanning digital interference holography *Opt. Express* **7** 305-10

[21] Dakoff A, Gass J and Kim M K 2003 Microscopic three-dimensional imaging by digital interference holography *J. Electr. Imag*. **12** 643-647

[22] Yu L, Myung M K 2005 Wavelength scanning digital interference holography for variable tomographic scanning *Opt. Express* **13** 5621-7

[23] Yu L, Myung M K 2005 Wavelength-scanning digital interference holography for tomographic 3D imaging using the angular spectrum method *Opt. Lett.* **30** 2092

[24] Kim M K, Yu L and Mann C J 2006 Interference techniques in digital holography *J. Opt. A: Pure Appl. Opt.* **8** 512-23

[25] Gass J, Dakoff A and Kim M K 2003 Phase imaging without 2-pi ambiguity by multiwavelength digital holography *Opt. Lett*. **28** 1141-3

[26] Mann C J, Yu L, Lo C M and Kim M K 2005 High-resolution quantitative phase-contrast microscopy by digital holography *Opt. Express* **13** 8693-98

[27] Parshall D and Kim M K 2006 Digital holographic microscopy with dual wavelength phase unwrapping *Appl. Opt.* **45** 451-59

[28] Mann C, Yu L and Kim M K 2006 Movies of cellular and sub-cellular motion by digital holographic microscopy *Biomed. Engg. Online* **5** 21

[29]. Chiseliță D, Danielescu C and Apostol A. Correlation between structural and functional analysis in glaucoma suspects. *Oftalmologia*. 2008; 52:111-8.

[30]. Zaveri MS, Conger A, Salter A, et al. Retinal imaging by laser polarimetry and optical coherence tomography evidence of axonal degeneration in multiple sclerosis. *Arch Neurol*. 2008; 65:924-8.

[31]Yücel YH, Gupta N, Kalichman MW, et all. Relationship of Optic Disc Topography to Optic Nerve Fiber Number in Glaucoma. *Arch Ophthalmol.* 1998;116:493-497.

[32]. Huang D, Swanson EA, Lin CP, et al. Optical coherence tomography. *Science* 1991; 254:1178-1181.

[33]. Brezinski M. *Optical Coherence Tomography. Principles and Applications.* Burlington, MA: Elsevier; 2006.

[34]. Wojtkowski M, Bajraszewski T, Targowski P, et al. Real-time in vivo imaging by high-speed spectral optical coherence tomography. *Opt. Lett*. 2003; 28: 1745-1747.

[35]. Podoleanu AG, Rogers JA, Jackson DA, Dunne S. Three-dimensional OCT images from retina and skin. *Opt Exp.* 2000;7:292–298.

[36]. Rogers JA, Podoleanu AG, Dobre GM, Jackson DA, Dunne S. Topography and volume measurements of the optic nerve using en-face optical coherence tomography. *Opt Exp.* 2001;9:533–545.

[37]. Schuman JS, Puliafito CA, Fujimoto JG. *Optical Coherence Tomography of Ocular Diseases.* 2. Thorofare, NJ: SLACK Inc; 2004: 21–53.

[38]. Wojtkowski M, Srinivasan V, Fujimoto JG et all. Three-dimensional Retinal Imaging with High-Speed Ultrahigh-Resolution Optical Coherence Tomography. *Ophthalmology*. 2005; 112: 1734-1746.

[39]. Drexler W, Morgner U, Ghanta RK, Schuman JS, Kärtner FX, Fujimoto JG. Ultrahigh resolution ophthalmologic optical coherence tomography. *Nat Med.* 2001;7:502–507.

[40]. Srinivasan VJ, Gorczynska, and Fujimoto GJ. High-speed, high-resolution optical coherence tomography retinal imaging with frequency-swept laser at 850 nm. *Opt. Lett.* 2007:32: 361-363.

[41]. Srinivasan VJ, Ko TH, Wojtkowski M, et al. Noninvasive Volumetric Imaging and Morphometry of the Rodent Retina with High-Speed, Ultrahigh-Resolution Optical Coherence Tomography. *Invest. Ophthalmol.Vis. Sci.* 2006; 47:5522-5528.

[42]. Yasuno Y, Hong Y, Makita S, et al. In vivo high-contrast imaging of deep posterior eye by 1-μm swept source optical coherence tomography and scattering optical coherence angiography. *Opt. Express*. 2007; 15: 6121-6139.

[43]. Wollstein G, Paunescu LA, Ko TH. Ultrahigh-resolution optical coherence tomography in glaucoma. *Ophthalmology*. 2005;112:229–237.

[44]. Dubois A, Vabre L, Boccara AC and Beaurepaire E. High-resolution full-field optical coherence tomography with Linnik microscope. *Appl. Opt.* 2002; 41: 805-812.

[45]. Lingfeng Yu and M.K. Kim"Full-color three-dimensional microscopy by wide-field optical coherence tomography, Vol. 12, No. 26 / OPTICS EXPRESS 6632` 2004

[46]. Quigley HA, Dunkelberger GR, Green WR. Retinal ganglion cell atrophy correlated with automated perimetry in human eyes with glaucoma. Am J Ophthalmol. 107, 453-467 (1989).

[47]. Cense B, Chen TC, Pierce MC, De Boer JF. Thickness and Birefringence of Healthy Retinal Nerve Fiber Layer Tissue Measured with Polarization-Sensitive Optical Coherence Tomography. Investigative Ophthalmology & Visual Science, 45, 2606-2612 (2004).

[48]. Leung CK, Chan WM, Yung WH, et al. Comparison of macular and peripapillary measurements for the detection of glaucoma: an optical coherence tomography study. *Ophthalmology* 112, 391-400 (2005).

[49]. Wollstein G, Ishikawa H, Wang J, et al. Comparison of three optical coherence tomography scanning areas for detection of glaucomatous damage. *Am J Ophthalmol.* 139, 39–43 (2005).

[50]. Dale Purves et al. ,"Neuroscience, second edition," 2001.

[51]. H. Faulds, "On the Skin-furrows of the Hand," Nature **22**, 605 (1880).

[52]. F. Galton, "Personal Identification and Description," Nature **38**, 201-202 (1888).

[53]. A. M Knowles, "Aspects of physicochemical methods for the detection of latent fingerprints," *Phys. E: Sci. Instrum.* **11,** 713-721 (1978).

[54]. J. Han, Z. Tan, K Sato and M Shikida, "Thermal characterization of micro heater arrays on a polyimide film substrate for fingerprint sensing applications," J. Micromech. Microeng. **15**, 282-289 (2005).

[55]. M. Pluta, W. Bicz, "Ultrasonic Setup for Fingerprint Patterns Detection and Evaluation," Acoustical Imaging **22**, Plenum Press (1996).

[56]. R. K. Rowe, S. P. Cocoran, K. A. Nixon, and R. E. Nostrom, "Multispectral Fingerprint Biometrics," Proc. SPIE **5694**, 90 (2005).

[57]. S. S. Lin, K. M. Yemelyanov, E. N. Pugh Jr., N. Engheta, "Polarization- and Specular-Reflection-Based, Non-contact Latent Fingerprint Imaging and Lifting," J. Opt. Soc. Am. A **23**, 2137-2153 (2006).

[58]. S. Chang, Y. Mao, S. Sherif and C. Flueraru, "Full-field optical coherence tomography used for security and document identity," Proc. of SPIE, **6402**, 64020Q (2006).

[59]. Y. Cheng and K. V. Larin, "Artificial fingerprint recognition by using optical coherence tomography with autocorrelation analysis," Appl. Opt. **45**, 9238-9245 (2006).

[60]. Y. Cheng and K. V. Larin, "*In Vivo* Two- and Three-Dimensional Imaging of Artificial and Real Fingerprints With Optical Coherence Tomography," Photonics Technology Letters, **19**, 1634-1636 (2007).

[61]. S. Chang, Y. Cheng, K.V. Larin, Y. Mao1, S. Sherif, and C. Flueraru, "Optical coherence tomography used for security and fingerprint-sensing applications," IET Image Process., **2**, 48–58 (2008).

[62]. S. K. Dubey, T. Anna, C. Shakher, and D. S. Mehta, "Fingerprint detection using full-field swept-source optical coherence, Tomography," Appl. Phys. Lett. **91**, 181106 (2007).

[63]. S. K. Dubey, D. S. Mehta, A. Anand and C. Shakher, "Simultaneous topography and tomography of latent fingerprints using full-field swept-source optical coherence tomography," J. Opt. A: Pure Appl. Opt. **10**, 015307 (2008).

[64]. L. O'Gorman, "Overview of fingerprint verification technologies," Elsevier Information Security Technical Report **3**, (1998).

[65]. A. K. Jain, L. Hong, S. Pankanti, and R. Bolle, "An Identity-Authentication System Using Fingerprints," Proc. of the IEEE **85**, 1365-1388 (1997).

[66]. A. K. Jain, J. Feng, A. Nagar and K. Nandakumar, "On Matching Latent Fingerprints," Workshop on Biometrics, CVPR, (2008).

[67]. U. Park, S. Pankanti and A. K. Jain, "Fingerprint Verification Using SIFT Features," Proc. of SPIE Defense and Security Symposium, (2008).

[68]. Y. Zhu, S.C. Dass and A.K. Jain, "Statistical Models for Assessing the Individuality of Fingerprints", IEEE Transactions on Information Forensics and Security, **2**, 391-401 (2007).

[69]. A. K. Jain, Y. Chen, M. Demirkus, "Pores and Ridges: High-Resolution Fingerprint Matching Using Level 3 Features," IEEE Transactions on Pattern Analysis and Machine Intelligence **29**, 15-27 (2007).

[70]. A. Ashkin, "Acceleration and trapping of particles by radiation pressure," Phys. Rev. Lett. **24**, 156-159, (1970).

[71]. A. Ashkin and J..M. Dziedzic, "Optical levitation by radiation pressure," Appl. Phys. Lett., 1971.

[72]. A. Ashkin, J..M. Dziedzic, J.E. Bjorkholm, and S. Chu, "Observation of a single-beam gradient force optical trap for dielectric particles," Optics Lett., (1986).

[73]. J.C.H. Tan and R.A. Hitchings, *Invest. Ophthalmol.Vis. Sci.* **44** 1132 (2003).

[74]. K.H. Min, G.J. Seong, Y.J. Hong, *et al*. *Kor. J. Ophthalmol*. **19** 189 (2005).

[75]. J. Xu, H. Ishikawa, G. Wollstein, *et al*. *Invest. Ophthalmol.Vis. Sci.* **49** 2512 (2008).

[76]. O. Geyer, A. Michaeli-Cohen, D.M. Silver, *et al*. *Br. J. Ophthalmol.* **82** 14 (1998).

[77. F.S. Mikelberg, *Can. J. Ophthalmol.* **42** 421 (2007).

[78]. J.B. Jonas, G.C. Gusek, and G.O.H. Naumann, *Invest. Ophthalmol.Vis. Sci.* **29** 1151 (1998).

[79]. N.V. Swindale, G. Stjepanovic, A. Chin, et al. *Invest. Ophthalmol.Vis. Sci.* **41** 1730 (2000).

[80]. C. Bowd, L.M. Zangwill, E.Z. Blumenthal, et al. *J. Opt. Soc. Am. A*. **19** 197 (2002).

[81]. K. C. Neuman and S. M. Blocka, "Optical trapping," *Rev Sci Instrum*. 2004 September ; 75(9): 2787–2809.

[82]. Gosse C, Croquette V. Biophys J 2002;82:3314. [PubMed: 12023254]

[83]. Keller M, Schilling J, Sackmann E. Rev Sci Instrum 2001;72:3626.

[84]. M. C. Potcoava and M.K. Kim, "Optical tomography for biomedical applications by digital interference holography" Meas. Sci. Technol. Vol. 19**,** 074010 (2008).

[85]. Mariana C. Potcoava, Christine N. Kay, Myung K. Kim, and David W. Richards, "Digital Interference Holography in Ophthalmology", Journal of Modern Optics. (Accepted).

[86]. M. C. Potcoava and M.K. Kim, "Fingerprint Biometry Applications Digital Interference Holography and Low-Coherence Interferography", Applied Optics (In Review).

[87]. M. C. Potcoava, L. Krewitza and M.K. Kim, "Brownian motion of optically trapped particles by digital Gabor holography" (In preparation).

[88]. Myung K. Kim and Mariana Potcoava, "Fingerprint Biometry Applications of Digital Holography and Low-Coherence Interference Microscopy" in Digital Holography and Three-Dimensional Imaging, (Optical Society of America, 2009).

[89]. M. C. Potcoava and M.K. Kim, "Fingerprints scanner using Digital Interference Holography ", in Biometric Technology for Human Identification VI, (SPIE Defense, Security, and Sensing 2009), paper presentation 7306B-80.

[90]. Mariana C. Potcoava, Myung K. Kim, Christine N. Kay, "Wavelength scanning digital interference holography for high-resolution ophthalmic imaging", in Ophthalmic Technologies XIX, (SPIE 2009 BiOS), paper presentation 7163-10.

[91]. Kay CN, Potcoava M, Kim MK, Richards DW. "Digital Holography Imaging of Human Macula", Florida Society of Ophthalmology Resident Symposium. Palm Beach, FL, 2008 (Second place), paper presentation.

[92]. M.C. Potcoava, C.N. Kay, M.K. Kim, D.W. Richards." Digital Interference Holography in Ophthalmology", ARVO 2008, paper presentation 4011.

[93]. M. C. Potcoava and M. K. Kim, "3-D Representation of Retinal Blood Vessels through Digital Interference Holography," in Digital Holography and Three-Dimensional Imaging, OSA Technical Digest (CD), (Optical Society of America, 2008), paper presentation DMB2.

[94]. M. C. Potcoava and M. K. Kim, "Animal Tissue Tomography by Digital Interference Holography," in Adaptive Optics: Analysis and Methods/Computational Optical Sensing and Imaging/Information Photonics/Signal Recovery and Synthesis Topical Meetings on CD-ROM, OSA Technical Digest (CD) (Optical Society of America, 2007), paper presentation DWC6.

[95]. C. Potcoava,"Digital Interference Holography in the 21 st Century", USF Graduate Research Symposium 2008, poster presentation, (First Place).

[96]. Kay CN, Potcoava M, Kim MK, Richards DW, Pavan PR. "Digital Holography Imaging of Human Macula", ASRS (American Society of Retina Specialists 2008), poster presentation.

CHAPTER 2

SCALAR DIFRACTION THEORY AND OPTICAL FIELD RECONSTRUCTION METHODS

This chapter reviews numerical reconstruction algorithms for digital holography with emphasis on the angular spectrum method and Fresnel approximation method. A brief review of the diffraction principles are presented in Section 2.1. Numerical reconstruction methods are reviewed in Section 2.2. In Section 2.3 a comparison between the angular spectrum method and the Fresnel transform is presented. Results of the two reconstruction methods are shown in Section 2.4. Conclusions are presented in Section 2.5.

2.1. Introduction

The first definition of the *diffraction* has been made by Sommerfeld [1] as "any deviation of light rays from rectilinear paths which cannot be interpreted as reflection or refraction." The explanation of this phenomenon was made by Christian Huygens, as an answer to the question why the transition from light to shadow was gradual rather than abrupt [2]. After Thomas Young introduced the concept of interference, progress on further understanding diffraction was made in 1818 by Fresnel who made assumptions about the amplitude and phase of Huygens' secondary sources. He also calculated the

distribution of light in diffraction pattern with excellent accuracy and introduced the obliquity or inclination factor, in order to account for the deficiency in the back wave propagation.

Both Huygens and Fresnel ideas were put together by Kirchhoff in a mathematical description of the boundary values of the light incident on the surfaces [3]. Kirchhoff formulated the so-called Huygens-Fresnel principle that must be regarded as a first approximation. The difficulties of this theory occurred when the boundary conditions must be imposed both on the field strength and its normal derivative. The Rayleigh – Sommerfeld diffraction theory eliminates the use of the light amplitude at the boundary, by making use of the theory of Green's function [4, 5]. The Kirchhoff and Rayleigh-Sommerfeld theories require the electromagnetic field to be treated as a scalar phenomenon, the diffraction aperture must be large compared with a wavelength, and the diffraction fields must not be observed too close to the aperture [6].

This study will be presented as a scalar theory, ignoring the vectorial nature of the electric and magnetic fields that make up light waves. The vectorial nature becomes important in dealing with polarization and non-isotropic media. On solving Maxwell's wave equation, the electromagnetic wave has the form, $\psi(x,y,z;t) = u(x,y,z)e^{-iwt}$, where $u(x,y,z)$ is the complex amplitude of the wave and e^{-iwt} is the wave absolute phase time variation (see Appendix A).

To apply the scalar theory, one needs to assume the polarization direction of the field with the unit vector, $\vec{\varepsilon}$, is constant and the vector field $\vec{u}(x,\vec{y},z) = \vec{\varepsilon}u(x,y,z)$ transforms to the scalar field, and consequently the spatial part of the electromagnetic wave , $u(x,y,z)$, satisfies the scalar Helmholtz equation:

$$(\nabla^2 + k^2)u(x,y,z) = 0 \qquad (2.1)$$

where $k = w/c$ is the wavevector, w is the frequency of the light, c is the speed of light in vacuum, and ∇^2 is the Laplacian operator. This equation can be used to derive the equation for a general diffraction problem (i.e. an equation for the light field and, hence, the intensity, as a function of position behind an obstacle which is between the observation point and a given source).

2.2. Green Functions. The Integral Theorem of Helmholtz and Kirchhoff. The Rayleigh-Sommerfeld Diffraction Formula

Let U and V be any two complex-valued functions of position, and let S be a closed surface surrounding a volume V. If U, V, and their first and second partial derivatives are single-valued and continuous within and on S, Figure 2.1, the Gauss theorem can be applied to the vector fields U and V,

$$\int_V \left(U\nabla^2 V - V\nabla^2 U \right) dv = \oint_S \left(U\nabla V - V\nabla U \right) ds \qquad (2.2)$$

where $\nabla = \dfrac{\partial}{\partial n}$ is the partial derivative in the outward normal direction at each point on S.

This theorem is the prime foundation of scalar diffraction theory. A Green function is chosen to be a scalar function for the Equation (2.1) and the derivative of the outgoing Green function over the small sphere has the expression,

$$\frac{\partial}{\partial n} G(r - r') = 4\pi \qquad (2.3)$$

Within the volume V',G is forced to satisfy the Helmholtz equation,

$$(\nabla^2 + k^2)G = 0 \qquad (2.4)$$

Substituting the two Helmholtz equations (2.1) and (2.4) in (2.2) in the left-hand side of the Green's theorem, we find,

$$\int_{V'} \left(U\nabla^2 V - V\nabla^2 U \right) dv = \int_{V'} \left(UGk^2 - GUk^2 \right) dv = 0 \tag{2.5}$$

The right member of Equation (2.5) cancels, so the theorem reduces to,

$$\oint_{S'} (U\nabla V - V\nabla U) ds = 0 \tag{2.6}$$

or,

$$-\oint_{S'} (U\nabla V - V\nabla U) ds = \oint_{S} (U\nabla V - V\nabla U) ds \tag{2.7}$$

For a general point r' on S', we have, $G(r-r') = \dfrac{\exp(ik \mid r-r' \mid)}{\mid r-r' \mid}$ and

$$\int_{S'} \frac{\partial}{\partial n} G(r-r') ds = 4\pi \tag{2.8}$$

Letting ε become arbitrarily small or at the limit of S' approaching P', Equation (2.6) will become:

$$\oint_{S} (U\frac{\partial}{\partial n}G - G\frac{\partial}{\partial n}U) ds - U(r') \cdot 4\pi = 0 \tag{2.9}$$

and therefore,

$$U(r') = \frac{1}{4\pi} (\oint_{S} (U\frac{\partial}{\partial n}G - G\frac{\partial}{\partial n}U) ds \tag{2.10}$$

Considering a volume V" complimentary to V,

$$\frac{1}{4\pi} (\oint_{S''} (U\frac{\partial}{\partial n}G + G\frac{\partial}{\partial n}U) = 0 \tag{2.11}$$

Substitution of this result in Equation (2.7) and taking account of negative sign, yields,

$$U(r') = \frac{1}{4\pi} (\oint_S (\exp\frac{(ik\,|r-r'|)}{|r-r'|}\frac{\partial}{\partial n}U - U\frac{\partial}{\partial n}[\exp\frac{(ik\,|r-r'|)}{|r-r'|}]ds) \tag{2.12}$$

The result is known as the integral theorem of Helmholtz and Kirchhoff. It allows the field at any point P' to be expressed in terms of boundary values of the wave on any closed surface surrounding that point. The final expression of the field $U(r')$ is,

$$U(r') = \frac{1}{2\pi}\oint_S (U\frac{\partial}{\partial n}G)ds = -\frac{1}{2\pi}\oint_S (G\frac{\partial}{\partial n}U)ds . \tag{2.13}$$

These results are known as the Rayleigh-Sommerfeld diffraction formula of the first and second kind respectively (Goodman). If a potential function and its normal derivative vanish at the same time, along any finite curve segment, then the potential function must vanish on the entire plane.
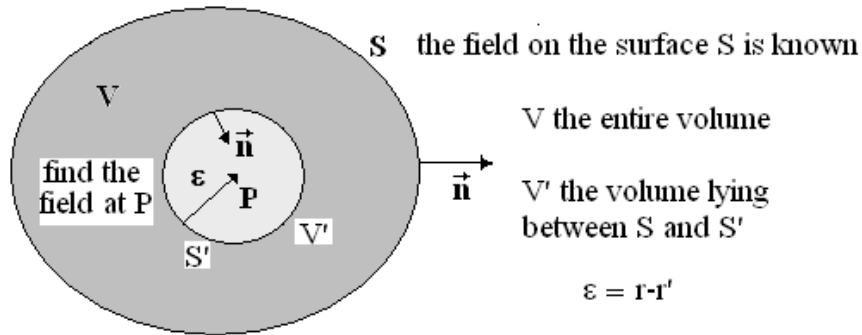
Figure 2.1. Geometric Illustration for Helmholtz–Kirchhoff Integral Theorem.

Now, we want to calculate the field U at point P' diffracted by a semi-transparent window S_A cut in an opaque screen.

$$\frac{\partial G(r-r')}{\partial n} = (ik - \frac{1}{|r-r'|})G(r-r')\cos(n,(r-r')) \approx (-ik)G(r-r') \tag{2.14}$$

and finally,

$$U(r') = \frac{1}{2\pi} \oint_{S_A} (U \frac{\partial}{\partial n} G) = -\frac{ik}{2\pi} \oint_{S_A} (U(r)G(r-r'))ds =$$

$$-\frac{i}{\lambda} \oint_{S_A} (U(r)G(r-r'))ds$$

(2.15)

This is known as the Huygens-Fresnel integral. The field $U(r')$ in plane z' can be calculated from the field in plane z, $U(r)$.

Let's consider two parallel planes (x, y, z) and $(x_0, y_0; z = 0)$ at normal distance z from each other. The diffracting aperture (source) lies in the (x_0, y_0) plane and the observation plane (reconstruction) lies in the (x, y).
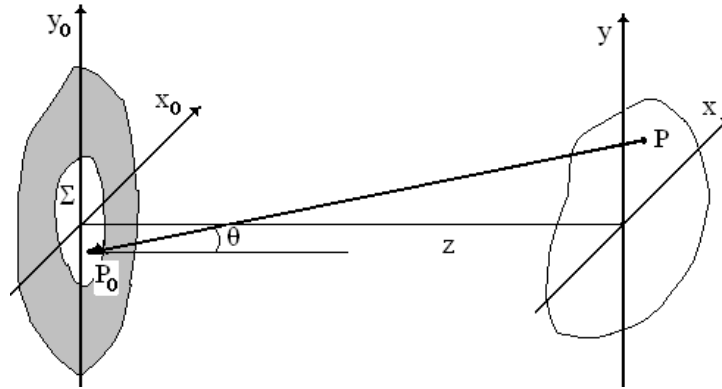
Figure 2.2: Huygens-Fresnel Principle in Rectangular Coordinate. (Adapted after J.W. Goodman, *Introduction to Fourier Optics, Third Edition*").

Huygens law states that the field $u(r)$ at a time t is related to the field $u(r')$ at an earlier time t' by the integral equation,

$$u(r) = \int_V u(r')G(r,r')dv$$

(2.16)

where the dependence of time was ignored.

Equation (2.13) can be stated as,

$$U(x,y,z) = \frac{1}{i\lambda} \oint_{S_A} (U(x0,y0;z=0) \frac{\exp(ikr)}{r} \cos\theta ds \qquad (2.17)$$

Where θ is the angle between the outward normal n and the vector $\vec{r}$ pointing

from (x,y,z) and $(x_0,y_0;z=0)$, $\cos\theta = \frac{z}{r}$, and $r = \sqrt{z^2 + (x-x_0)^2 + (y-y_0)^2}$, and the

Huygens-Fresnel principle can be written,

$$U(x,y,z) = \frac{z}{i\lambda} \oint_{S_A} (U(x_0,y_0;z=0) \frac{\exp(ikr)}{r} dx_0 dy_0 \qquad (2.18)$$

2.3. Optical Field Reconstruction Methods

Optical field reconstruction using diffraction methods involves the determination of the

object amplitude and phase. Amplitude is a quantity proportional to the square root of the

intensity in the diffraction pattern and represents the strength of interference at a specific

point. Phase is the relative time of arrival of the scattered radiation (wave) at a particular

point (*e.g.* photographic film), and this information is lost when the diffraction pattern is

recorded.

In digital holography a hologram is recorded digitally. The object field, $O(x,y)$

interferes with the reference field, $R(x,y)$, at the hologram plane. Here, we use a setup in

off-axis geometry, meaning the reference field interferes with the object field at an angle,

θ. The interference between the object wave $O(x,y) = Amp_O(x,y)\exp[i\varphi_O(x,y)]$ and the

plane reference wave $R(x,y) = \exp(i\varphi_R) = \exp[i2\pi(q_x x + q_y y)]$ is recorded in the hologram

plane $(x=x_0, y=y_0)$, in form of intensity, $h(x,y)$. $Amp_O(x,y)$ is the amplitude and

$\phi_O(x, y)$ is the phase of the object beam. The other two quantities, q_x and q_y, are the carrier frequency of the reference beam in the x and y directions respectively. The complex amplitude of the interference pattern is: $U(x, y) = R(x, y) + O(x, y)$. The hologram intensity pattern is recorded digitally by the CCD in the form:

$$h(x,y) = |R(x,y) + O(x,y)|^2 = 1 + |Amp_O(x,y)|^2 + 2Amp_O(x,y)\cos(\varphi_R - \varphi_O) =$$
$$1 + |Amp_O(x,y)|^2 + O(x,y)\exp[-i2\pi(q_x x + q_y y)] + O(x,y)^* \exp[i2\pi(q_x x + q_y y)] \tag{2.19}$$

The recorded image $h(x, y)$ contains information about both the amplitude and phase of the object beam. To reconstruct the object optical field from the recorded holograms, various methods are used. Optical methods or forward methods are preferred to statistical and inverse methods. Here we will review numerical reconstruction algorithms for digital holography with emphasis on the Fresnel approximation and angular spectrum methods.

The relationship between the two methods, or in other words, how to derive the Fresnel approximation starting from the angular spectrum of a plane wave, is given in Appendix B. The mathematical background of the Fourier transform is given in Appendix C.

2.3.1 Fresnel Approximation

The Fresnel transform, as an approximation to the Kirchoff diffraction integral (Equation 2.12), plays a significant role in evaluating the propagation of wave fields. In the one-dimensional case it is defined by

$$\alpha_{Fr}^D(f) = \int_{-\infty}^{\infty} a(x)\exp[-i\pi(x-f)^2 / D^2]dx \tag{2.20}$$

Where $\alpha(f)$ is called the integral transform of the signal $a(x)$, or its spectrum, and D is a transform parameter (Jaroslavsky). When the complex amplitude of the wave field is linked with the wave field amplitude in a Fresnel plane of the object, D^2 is the product of the illumination wavelength, λ with the distance between the object and the Fresnel or observation plane z, so $D^2 = \lambda z$. We apply Rayleigh-Sommerfeld formula of the first kind to the calculation of $U(r')$, by computing the surface integral on S, surrounding the volume V. The more usable expression for the Huygens-Fresnel principle needs approximations for the absolute distance $r = \sqrt{x^2 + y^2 + z^2}$, Equation (2.21) and for the wavevector along the propagation distance $k_z = \sqrt{k^2 - k_x^2 + k_y^2}$, Equation (2.22).

$$
\begin{aligned}
\sqrt{(x-x_0)^2 + (y-y_0)^2 + z^2} &= [z^2(1 + \frac{(x-x_0)^2 + (y-y_0)^2}{z^2})]^{1/2} \\
&= z(1 + \frac{(x-x_0)^2 + (y-y_0)^2}{2z^2} - \frac{(x-x_0^2 + (y-y_0)^2}{4z^2} + ...) \\
&\cong z(1 + \frac{(x-x_0)^2 + (y-y_0)^2}{2z^2})
\end{aligned}
\tag{2.21}
$$

and, $k^2 = k_x^2 + k_y^2 + k_z^2$, where,

$$
\begin{aligned}
k_z &= \sqrt{k^2 - k_x^2 + k_y^2} = k - \frac{k_x^2 + k_y^2}{2k} - \frac{k_x^2 + k_y^2}{4k_z^2} + ...) \cong \\
&k - \frac{k_x^2 + k_y^2}{2k}
\end{aligned}
\tag{2.22}
$$

And Equation (2.18) therefore becomes,

$$
U(x,y,z) = \frac{\exp(ikz)}{i\lambda z} \iint_{\pm\infty} (U(x_0, y_0; z = 0) \exp\{\frac{ik}{2z}[(x-x_0)^2 + (y-y_0)^2)]\}dx_0 dy_0
\tag{2.23}
$$

Equation (2.23) is a convolution between the field at source and the convolution kernel,

$$
h(x,y,z) = \frac{\exp(ikz)}{i\lambda z} \exp[\frac{ik}{2z}(x^2 + y^2)]
$$

31

Arranging this expression further, we get

$$U(x, y, z) = \frac{\exp(ikz)}{i\lambda z} \exp[\frac{ik}{2z}(x^2 + y^2)] \iint_{\pm\infty} (U(x_0, y_0; z = 0) \exp[\frac{ik}{2z}(x_0^2 + y_0)^2)]$$
$$* \exp[\frac{-ik}{2z}(xx_0 + yy_0)]dx_0 dy_0 \qquad (2.24)$$

Ignoring the front factor, the integral represents the Fourier transform of the product of the complex field to the right of the aperture and a quadratic phase exponential (Goodman, Hariharan, Schnars, Kuo, Scott).

The expression (2.24) could be written as,

$$U(x, y, z) = \exp[\frac{ik}{2z}(x^2 + y^2)]\mathcal{F}[U(x_0, y_0; z = 0) \cdot h] \qquad (2.25)$$

where $h = \frac{-ik}{2z} \exp[ikz + \frac{ik}{2z}(x_0^2 + y_0)^2)]$ is the PSF of the system.

There are two common methods to calculate the Fresnel transform. The first is by evaluating the Huygens integral for back propagating waves, and the second is by multiplying the Fourier transform of the Fresnel field with the Fresnel optical transfer function h, and then performing an inverse Fourier transform. Here we discussed the second one which is the most common hologram reconstruction method since it requires only one FFT.

The minimum reconstruction distance is imposed by the discrete Fourier transform, and it has the expression, $z_{min} = \frac{a^2}{N\lambda}$, where $a = N\Delta x$ is the size of the hologram, N x N is the hologram area in pixels, Δx is the pixel's size or the lateral resolution. We can also write the expression for the lateral resolution being $\Delta x = \frac{\lambda z}{N\Delta x_0}$,

where z is the reconstruction distance and Δx_0 is the pixel size of the CCD camera. The minimum of the reconstruction distance is $z_{\min}$.

2.3.2 The Angular Spectrum of a Plane Wave

The scalar diffraction theory can be reformulated using the theory of linear, invariant system. The Fourier components of any disturbance are analyzed at an arbitrary plane as plane waves traveling in various direction from that plane. The resultant field amplitude is the superposition off all these plane waves, at an arbitrary plane with a phase shift contribution due to the wave propagation..

We take Fourier transform of Equation (2.19), and obtain the spatial frequencies as follows:

$$\mathcal{H}(k_x, k_y) = \delta(k_x, k_y) + \mathcal{F}[Amp_O(x,y)^2] + A_0(k_x, k_y) * \delta(k_x + q_x, k_y + q_y)$$
$$+ A_0(k_x, k_y)\delta(k_x - q_x, k_y - q_y)$$

$$(2.26)$$

The first two terms represent the zero-order term and the third and forth represent the two conjugate images, real image centered around $(k_x = -q_x, k_y = -q_y)$ and virtual image centered around $(k_x = q_x, k_y = q_y)$. The first three terms can be filtered out in the Fourier space and the forth term is shift to the center of the coordinate to obtain the angular spectrum of the object, $A_0(k_x, k_y)$, in the hologram plane. To obtain the spectrum in the object plane, $A_0(k_x, k_y)$ is backward propagated in the frequency domain, along the propagation distance ($z = -Z$), and has the expression:

$$A(k_x, k_y, z) = A_0(k_x, k_y)\exp(ik_z z)$$

$$(2.27)$$

Taking the inverse Fourier transform, we obtain the reconstructed object wavefront,

33

$$U(x,y,z) = \mathscr{F}^{-1}\{A(k_x,k_y) \cdot \exp(ik_z z)\} \qquad (2.28)$$

Breaking the reconstructed complex field into its polar components we get

$$U(x,y,z) = Amp_{O-rec}(x,y)\exp[i\phi_{O-rec}(x,y)] \qquad (2.29)$$

where $Amp_{O-rec}(x,y)$, and $\phi_{O-rec}(x,y)$ represent the reconstructed object wavefront amplitude and phase at r. In this way, we can have access to both the amplitude and the phase information.

Using the angular spectrum method in hologram reconstruction does not require any minimum reconstruction distance. Another benefit of using this method is the filtering capability in the frequency space to remove the background and the virtual term.

2.4. Results

In the previous section and Appendix B, we concluded the two optical reconstructed methods are identical within the paraxial approximation. Since the angular spectrum does not use any approximation, the Fresnel method will never yield similar results as the angular spectrum method does for small reconstruction distance, unless numerical parametric lenses are introduced for wavefront reconstruction to make small reconstruction distances possible without aliasing, but increasing the computational load [7, 8]. To have a concrete idea about how objects are imaged using the two reconstruction methods, we present a few results of various samples. The objects are: the USAF 1951 resolution target, onion skin, and a US coin. Corresponding holograms recorded in off-axis geometry are shown in Figure 2.3a, Figure 2.4a, and Figure 2.5a respectively. Their Fourier transforms are displayed in Figure 2.3b, Figure 2.4b, and Figure 2.5b. The bright spot in the center of images represents the DC term or the zero order of diffraction and can be separated from the real and the virtual images (located symmetrically of the DC

term) by choosing an appropriate angle between the object and reference wave fronts. The DC term represents the background or low frequencies features of the object. The virtual and real images account for high frequencies object features. Applying a circular filter (white circle) in the Fourier space we can get rid of the zero order term, virtual images and other noise present in the image.

Figure 2.3c and Figure 2.3d represent the amplitude and the phase images reconstructed from the hologram (Figure 2.3a), of an area of $1040 \times 1040 \, \mu m^2$ using the angular spectrum. The object is situated at a distance $z = 270 \, \mu m$ from the hologram. Figure 2.3e, f, g, h represent the amplitude and the phase images reconstructed from the hologram (Figure 2.3a), of an area of $1040 \times 1040 \, \mu m^2$ using the Fresnel approximation. Figure 2.3e and Figure 2.3f are reconstructed with the minimum reconstruction distance

$z_{min} = \dfrac{a^2}{N\lambda} = 7348 \mu m$ (imposed by the discrete Fourier transform) and Figure 2.3g and

Figure 2.3h are reconstructed with the reconstruction distance $z < z_{min}$, $z = 7000 \mu m$.
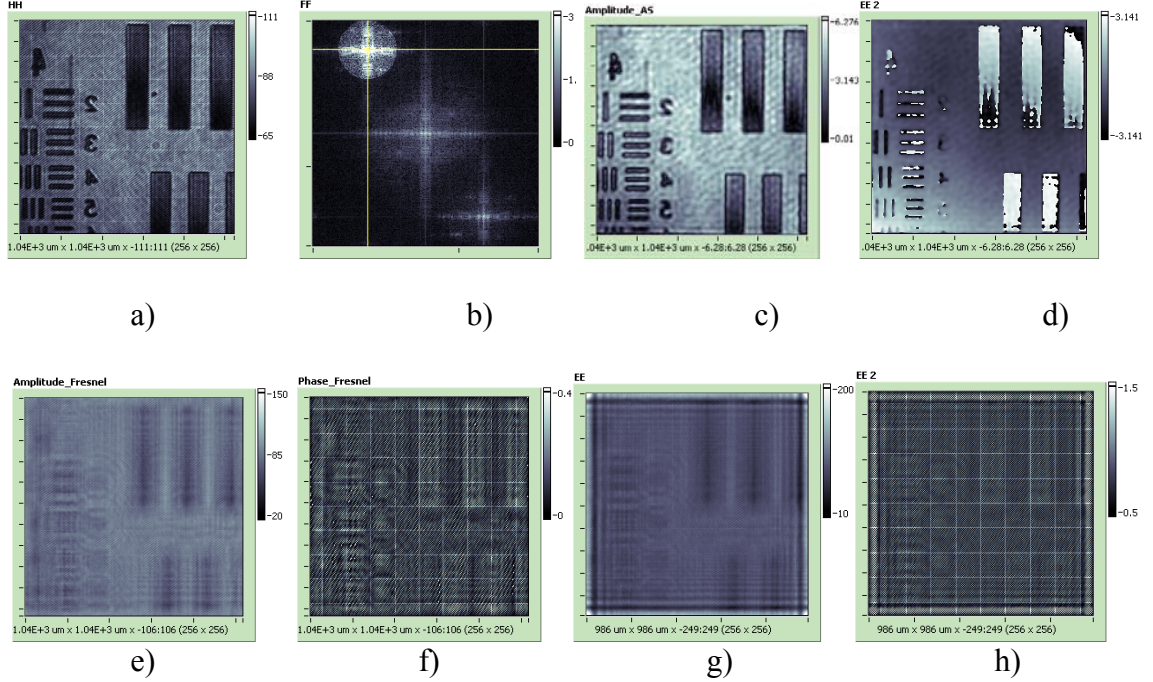
Figure 2.3: Holography of an USAF Resolution Target. The image area is $1040 \times 1040 \, \mu m^2$ (256×256 pixels) and the image is at $z = 270 \, \mu$m from the hologram, $\lambda = 0.575 \mu m$, $a = 1040 \mu m$, N=256, : (a) hologram; (b) angular spectrum; (c) amplitude and (d) phase images by the angular spectrum method; (e) amplitude and (f) phase images at minimum reconstruction distance $z_{min} = \dfrac{a^2}{N\lambda} = 7348 \mu m$ by the Fresnel transform method; (g) amplitude and (h) phase images at the reconstruction distance $z = 7000 \mu$m ($z < z_{min}$) by the Fresnel transform method

Figure 2.4 is an example of how the lateral resolution is affected by the minimum reconstruction distance requirement. In Section 2.3.1 we have shown the lateral resolution is $\Delta x = \dfrac{\lambda z}{N\Delta x_0} = f(z, \Delta x_0)$. The area of the hologram (Figure 2.4a), reconstructed amplitude (Figure 2.4c), and phase (Figure 2.4d) is 235x176 μm^2, 640x480 pixels which gives two reconstruction distances in each direction, x, y,

$z_x = z_{\min,x} = \dfrac{a_x^2}{N_x \lambda} = 150 \mu m$, $z_y = z_{\min,y} = \dfrac{a_y^2}{N_y \lambda} = 112 \mu m$. The angular spectrum is not constrained by the hologram area and the lateral resolution is affected only by the optics.

a) b) c) d)
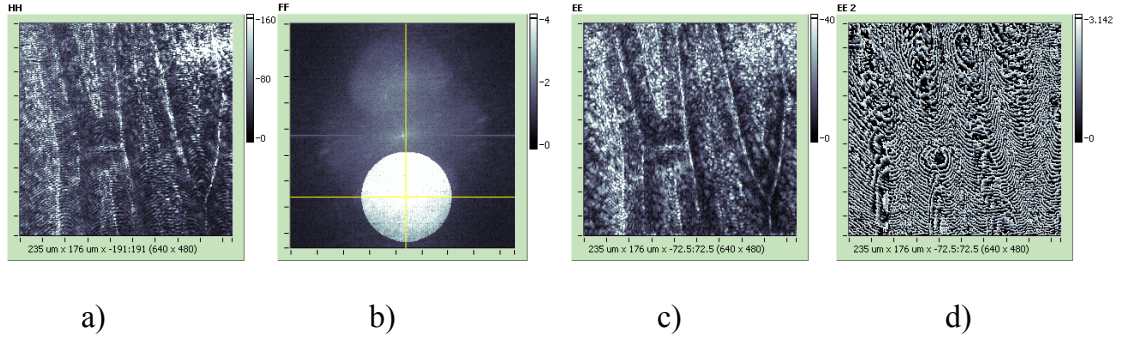
Figure 2.4. Holography of the Onion Skin. The image area is $236 \times 176 \,\mu m^2$ (640 × 480 pixels) and the image is at z = 4.95 μm from the hologram: (a) hologram; angular spectrum; (c) amplitude and (d) phase, images by the angular spectrum method.

Again, this is an example of a hologram recorded when the object is situated at a distance z = 198 μm from the hologram Figure 2.5. This distance is smaller than the

$z_{min} = \dfrac{a^2}{N\lambda} = 8370\,\mu m$ and the amplitude(Figure 2.5d) and phase images (Figure 2.5e) are

not qualitative images. When $z < z_{min}$ aliasing occurs (Figure 2.5f).

a)   b)   c)   d)

e)   f)   g)   h)
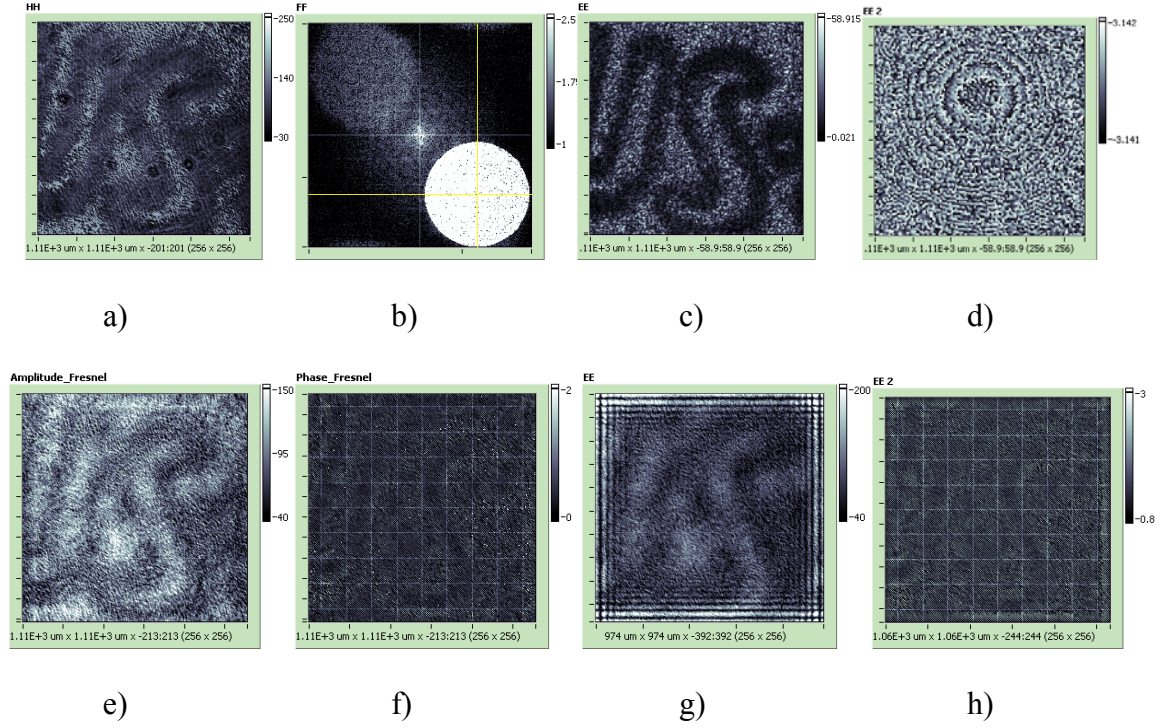
Figure 2.5. Holography of a US Coin. The image area is $1110 \times 1110\,\mu m^2$ (256 ×

256 pixels) and the image is at $z = 198$ μm from the hologram, $\lambda = 0.575\mu m$,

$a = 1110\mu m$, N=256 pixels: (a) hologram; (b) angular spectrum; (c) amplitude and (d)

phase images by the angular spectrum method; (e) amplitude and (f) phase images at

minimum reconstruction distance $z_{min} = \dfrac{a^2}{N\lambda} = 8370\mu m$ by the Fresnel transform method;

(g) amplitude and (h) phase images at the reconstruction distance $z = 8000\mu m\,(z < z_{min})$

by the Fresnel transform method.

In summary, unique capabilities of the angular spectrum compared to the Fresnel approximation are: higher degree of accuracy as it is seen in all images obtained by the angular spectrum, filtering in the frequency domain shown in Figure 2.3b, Figure 2.4b, Figure 2.5b, and there is no minimum reconstruction distance.

2. 5. Conclusion

We demonstrated the capabilities of the two diffraction reconstruction methods, the angular spectrum and the Fresnel approximation in imaging resolution target, onion and coin. The two optical reconstructed methods are identical within the paraxial approximation. Since the angular spectrum is the true method, the Fresnel approximation will never give similar results as the angular spectrum method does.

2. 6. Bibliography

[1] J.W. Goodman, *Introduction to Fourier Optics*. McGraw-Hill Publishing Company, New York (1968).

[2]. Huygens, C. *Traité de la lumière* (completed in **1678**, published in Leyden, **1690**).

[3]. Kirchoff, G. "Zur Theorie der Lichtstrahlen," *Wiedemann Ann.* **1896**, *18(2)*, 663.

[4]. Sommerfeld, A. "Mathematische Theorie der Diffraction," *Math. Ann.* **1896**, *47*, 317.

[5]. Sommerfeld, A. "Die Greensche Funktion der Schwingungsgleichung," *Jahresber. Deut. Math.* **1912**, *21*, 309.

[6]. Wolf, E.; Marchand, E. W. "Comparison of the Kirchhoff and the Rayleigh-Sommerfeld theories of diffraction at an aperture," *J. Opt. Soc. Am.* **1964**, *54(5)*, 587–594.

[7]. F. Montfort, F. Charrière, T. Colomb, E. Cuche, P. Marquet, and C. Depeursinge, "Purely numerical correction of the microscope objective induced curvature in digital holographic microscopy," J. Opt. Soc. Am. A **23,** 2944–2953 (2006).

[8]. T. Colomb, F. Montfort, J. Kühn, N. Aspert, E. Cuche, A. Marian, F. Charrière, S. Bourquin, P. Marquet, and C. Depeursinge, "Numerical parametric lens for shifting, magnification, and complete aberration compensation in digital holographic microscopy," J. Opt. Soc. Am. A **23** (2006).

CHAPTER 3

DIGITAL INTERFERENCE HOLOGRAPHY

This chapter introduces the principle of digital interference holography (DIH), geometry, apparatus, calibration, and phase unwrapping theory. The chapter is organized as follows: Section 3.1 describes the digital interference holography in comparison to the other optical imaging techniques. The digital interference holography technique is reviewed in Section 3.2. Section 3.3 presents the phase unwrapping theory based on DIH. Section 3.4 describes the design of the DIH apparatus. Section 3.5 reviews the setup calibration and the scanning characteristics of the light source. Finally, conclusions are presented in Section 3.6.

3.1. Introduction

One of the important challenges for biomedical optics is noninvasive three dimensional imaging, and various techniques have been proposed and available. For example, confocal scanning microscopy provides high-resolution sectioning and in-focus images of a specimen. However, it is intrinsically limited in frame rate due to serial acquisition of the image pixels. Ophthalmic imaging applications of laser scanning *in vivo* confocal microscopy have been recently reviewed [1]. Another technique, optical coherence tomography (OCT), is a scanning microscopic imaging technique with micrometer scale axial and lateral resolution, based on low coherence or white light interferometry to

coherently gate backscattered signal from different depths in the object [2, 3]. Swept-source optical coherence tomography is a significant improvement over the time-domain OCT [4-6], in terms of the acquisition speed and signal-to-noise ratio (SNR). A related technique of wavelength scanning interferometry uses the phase of the interference signal, between the reference light and the object light which varies in the time while the wavelength of a source is swept over a range. A height resolution of about 3 μm has been reported using Ti:sapphire laser with wavelength scanning range of about 100 nm [7, 8]. The technique of structured illumination microscopy provides wide-field depth-resolved imaging with no requirement for time-of-flight gated detection [9].

In the last few years, the scanning wavelength technique in various setups has been adopted by researchers for three-dimensional imaging of microscopic and submicroscopic samples. When digital holography is combined with optical coherence tomography, a series of holograms are obtained by varying the reference path length [38]. A new tomographic method that combines the principle of DIH with spectral interferometry has been developed using a broadband source and a line-scan camera in a fiber-based setup [39]. Sub-wavelength resolution phase microscopy has been demonstrated [40] using a full-field swept-source for surface profiling. Nanoscale cell dynamics were reported using cross-sectional spectral domain phase microscopy (SDPM) with lateral resolution better than 2.2 μm and axial resolution of about 3 μm [41]. A spectral shaping technique for DIH is seen to suppress the sidelobes of the amplitude modulation function and to improve the performance of the tomographic system [42]. Submicrometer resolution of DIH has been demonstrated [43].

Another optical tomographic technique, applied widely for determination of the refractive index [44-49], is based on acquiring multiple interferograms while the sample is rotating. The reconstruction of the phase distribution is performed using filtered back-projection algorithm. Then the phase distribution is scaled to refractive index values. Refractive index distribution reveals information about the cellular internal structure of a transparent or semitransparent specimen.

In this paper, we use computer and holographic techniques with digital interference holography (DIH) to accurately and consistently identify and quantify different objects structure with μm resolution. This technique is based on an original numerical method [28], where a three-dimensional microscopic structure of a specimen can be reconstructed by a succession of holograms recorded using an extended group of scanned wavelengths.

3.2. Principle of Digital Interference Holography

Suppose an object is illuminated by a laser beam of wavelength λ. A point r_0 on the object scatters the light into a Huygens wavelet, $A(r_0)\exp(ik|r-r_0|)$, where the object function $A(r_0)$ is proportional to the amplitude and phase of the wavelet scattered or emitted by object points (Figure 3.1a). For an extended object, the field at r is $E(r) \sim \int A(r_0)\exp(ik|r-r_0|)d^3r_0$, where the integral is over the object volume. The amplitude and phase of this field at the hologram plane z = 0 is recorded by the hologram, as $H(x_h, y_h; \lambda)$. The holographic process is repeated using N different wavelengths, generating the holograms $H(x_h, y_h; \lambda_1), H(x_h, y_h; \lambda_2), ..., H(x_h, y_h; \lambda_N)$. From each of the holograms, the field $E(x, y, z; \lambda)$ is calculated as a complex 3D array over the volume in

the vicinity of the object (Figure 3.2a). Superposition of these N 3D-arrays results in

$\sum_k \int A(r_0) \exp(ik|r - r_0|) d^3 r_0 \sim \int A(r_0) \delta(r - r_0) d^3 r_0 \sim A(r)$. That is, for a large enough number

of wavelengths, the resultant field is proportional to the field at the object and is nonzero

only at the object points. In practice, if one uses a finite number N of wavelengths, with

uniform increment $\Delta(1/\lambda)$ of the inverse wavelengths, then the object image $A(r)$ repeats

itself (other than the diffraction/defocusing effect of propagation) at a beat wavelength

$\Lambda = [\Delta(1/\lambda)]^{-1}$, with axial resolution $\delta = \Lambda / N$. By use of appropriate values of $\Delta(1/\lambda)$

and N, the beat wavelength Λ can be matched to the axial range of the object, and δ to

the desired level of axial resolution (see Appendix A).
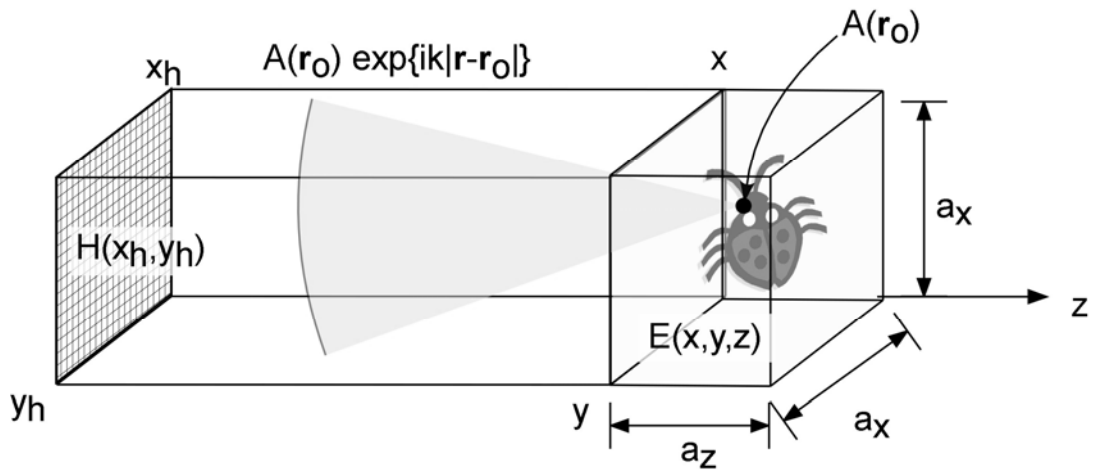
a)
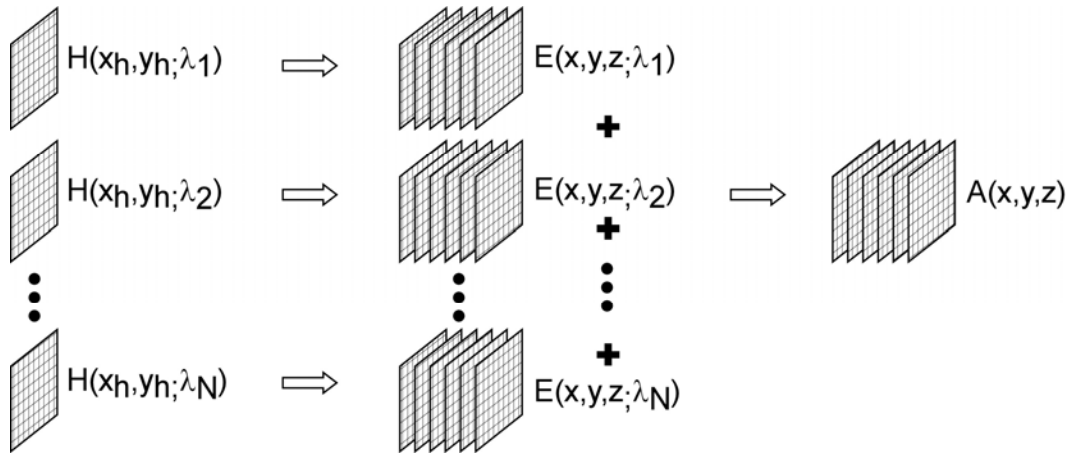
b)

Figure 3.1: Digital Interference Holography Geometry a) DIH Volume Representation, and b) process of DIH. H: hologram; E: optical field in the object volume; A: object function. See text for more details.

3.3 Multiple-Wavelength Optical Phase Unwrapping by Digital Interference Holography

The optical thickness profile of transparent object can be obtained from quantitative phase images with sub-wavelength accuracy. Two important parameters are subsequently derived from the optical thickness profile, the physical thickness and the index of refraction of the sample. Quantitative phase images are already demonstrated using several digital holography techniques based on two or three wavelengths [50-54]. Using digital interference holography, we want to make use of the phase information to determine the physical height of the sample. The combination of phase images of two different wavelengths λ_1 and λ_2 results in another phase image whose effective or beat wavelength is $\Lambda = \lambda_1 \lambda_2 / |\lambda_1 - \lambda_2|$. By choosing the two wavelengths close enough, the beat wavelength can be made large enough to cover the range of optical thickness of the object. This is another example of the capabilities of digital holography that are not possible in real space holography. The phase difference between two wavelengths λ_1, λ_2 is: $\phi_{12} = \phi_1 - \phi_2 = 4\pi h n(\lambda)(\frac{1}{\lambda_1} - \frac{1}{\lambda_2})$, where $n(\lambda)$ is an approximate value of the refractive index of the sample being imaged. Consequently, by choosing an appropriate combination of wavelengths, the height profile of an image is:

$$h = \frac{\phi_1 - \phi_2}{4\pi n(\lambda)(\frac{1}{\lambda_1} - \frac{1}{\lambda_2})} = \frac{\phi_1 - \phi_2}{4\pi n(\lambda)} \Lambda 12 . \tag{3.1}$$

3.4. Experimental Setup

The basic configuration of the apparatus is a Michelson interferometer, Figure 3.2. The light source is a Coherent 699 ring dye laser, pumped by Millenia V diode-pumped solid-state laser, tunable over a range of 565 nm to 615 nm with an output power of up to 500 mW. The laser output is spatial-filtered and collimated. The focusing lens L2 focuses the laser on the back focus of the objective lens L3, so that the object is illuminated by a collimated beam.
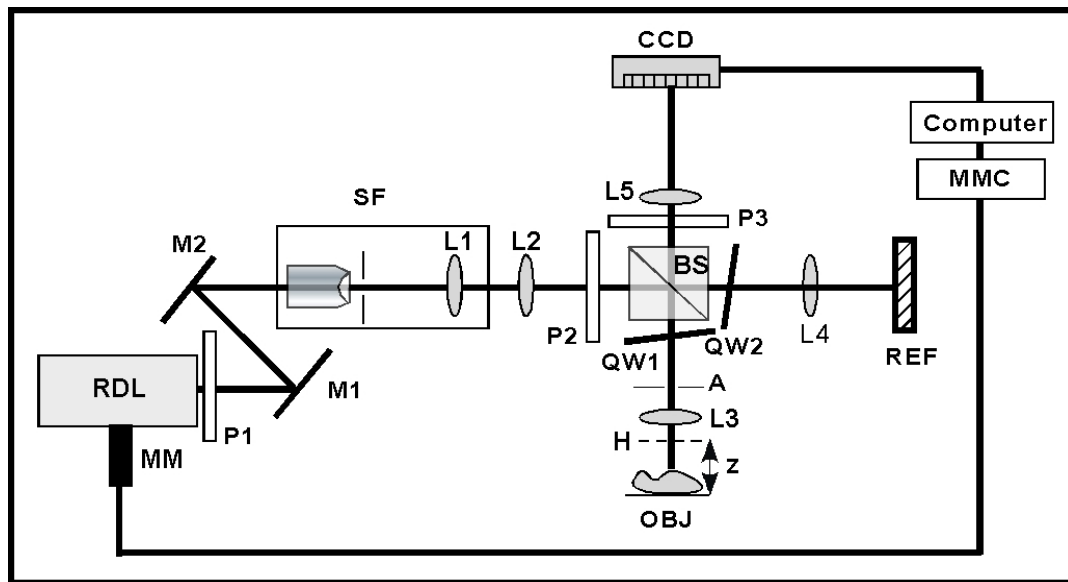
Figure 3.2. Digital Interference Holography Apparatus. RDL: ring dye laser; M's: mirrors; SF: spatial filter and expander; L's: lenses; P's: polarizers; BS: polarizing beamsplitter; QW's: quarter waveplates; A: aperture; H: hologram plane; OBJ: object; REF: reference mirror; MM: motorized micrometer; MMC: controller for MM.

The lenses L3 and L5 form a microscope pair, Figure 3.3, so that the CCD acquires a magnified image of a plane H in the vicinity of the object plane. The reference mirror is an optical conjugate of the plane H through the matching objective lens L4. Then the image acquired by the CCD is equivalent to a holographic interference between a plane reference wave and the object wave that has propagated (diffracted) over a distance z from the object plane. In general the object plane may be at an arbitrary distance z from the hologram plane H, and the object can be numerically brought back in focus by the digital holography process. But in practice, it is advantageous to keep the object plane in focus to simplify the optical alignment and to help identify the object portion being imaged, as well as minimizing potential secondary aberration effects. The polarization optics – polarizer P2, analyzer P3, quarter wave plates, and polarizing beam splitter – is used to continuously adjust the relative partition of optical power between the object and referernce fields and to maximize the interference contrast. The polarizer P1 at the output of laser is used to continuously adjust the overall power input to the interferometer. The CCD camera (Sony XC-ST50) has 780 x 640 pixels with 9 μm pitch, and is digitized with an 8-bit monochrome image acquisition board (NI IMAQ PCI-1407). Slight rotations of the reference mirror and object planes enable the acquisition of off-axis hologram. A variable aperture placed at the back focal (Fourier) plane of the objective lens L3 can be useful in controlling the angular spectrum of the object field. The aperture acts as a Fourier filter that stops the scattered light coming from the object. Hence, relatively most of the light that passes the small disk filter corresponds to a small scattering angle.
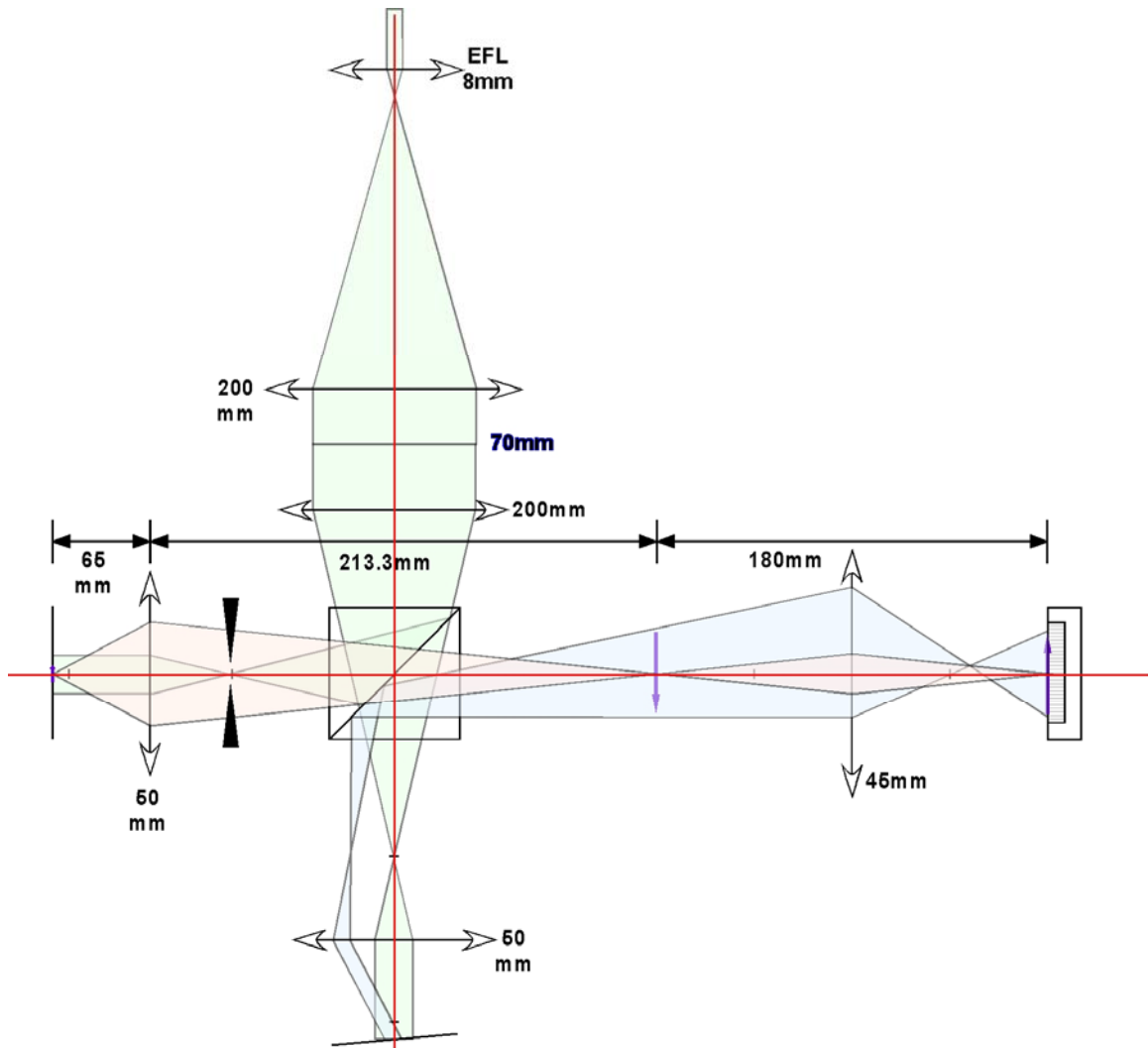
Figure 3.3. Rays diagram

When laser light travels through the linear polarizer, Figure 3.4a, a selected vibration plane is passed by the polarizer (parallel to the transmission axis) and the electric field vectors vibrating in all other orientations are blocked. The polarized beam splitter reflects part of the laser beam, linearly polarized at 90° from its original plane, to the object and also the BS transmits part of the laser beam to the reference. When the light is incident of a quarter-wave plate, QW, the light is divided into two equal electric field components and one of them is retarded by a quarter-wave plate, producing a

circularly polarized light. After passing back through the QW plate, Figure 3.4b, the reflected light is linearly polarized at 90° from its original plane. The reflected light from the object passes as a transmitted wave through the beam splitter and it combines at the analyzer plane with the reflected light from the reference mirror. The analyzer is utilized to control the amount of light passing through the crossed pair (polarizer-analyzer), and can be rotated in the light path to enable various amplitudes of polarized light to pass through.
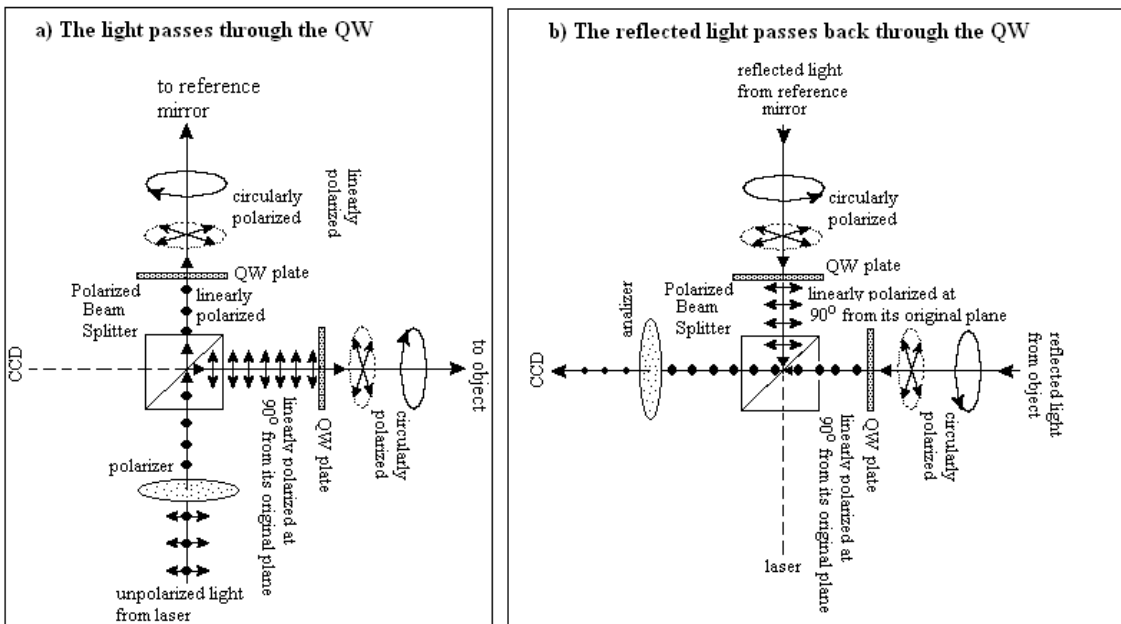
Figure 3.4. Polarization Control in Digital Interference Holography

3.5. Experimental Calibration

3.5.1 The tuning characteristics of the light source

The light source used in this experiment was a dye laser pumped by a solid state laser. To obtain the tuning range of about 40 nm necessary for our experiments, Rhodamine 6G

(R6G) dissolved in ethylene glycol has been chosen. The tunning curve is shown in Figure 3.5. The wavelength tunable range of 34 nm for this experiment was between 568 nm to 602 nm. The tunable wavelength range determines the axial resolution of the image, while the tuning resolution or the wavelength increment determines the axial range, or the axial size of an object. The ability to distinguish axial distances of various layers of a tissue is called the axial resolution, δz. This tuning parameter is obtained in the following way:

$$k = \frac{2\pi}{\lambda}, \delta k = \frac{2\pi\Delta\lambda}{\lambda^2}, \Lambda = \frac{2\pi}{\delta k} = \frac{\lambda^2}{\delta\lambda}, \delta z = \frac{\Lambda}{N} \qquad (3.1)$$

where, λ is the center wavelength, $\delta\lambda$ is the wavelength increment, k is the wavevector, δk is the wave number increment, δz is the axial resolution and Λ is the object axial size. The hologram acquisition process is described in Appendix D. Figure D.1 shows the main screen of the DIH software, written in Labview 8.5. The wavelength scanning process is controlled by a stepper motor that changes the birefringent filter of the laser in small increments, changing the laser wavelength when it rotates, Figure D.2.
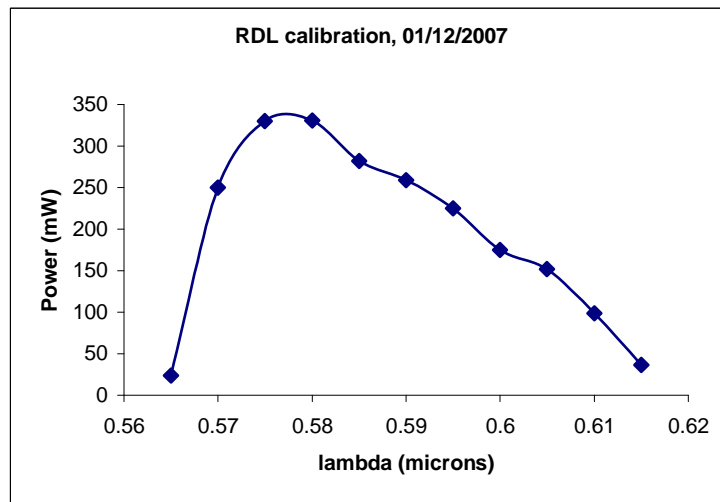
Figure 3.5. Tuning Curve of the Rhodamine 6G

3.5.2 The calibration curve

The digital interference holography requires a sequence of wavelength within the Rhodamine 6G spectral range. To be able to get the right wavelengths when the controlled micrometer changes the birefringent filter we used a monocrometer (CVI Digikrom 240) with with a spectral resolution of ca. ($\pm 2cm^{-1}$). Two calibrations were performed, micrometer position versus wavelength (Figure D.3) and, micrometer position versus wavevector (Figure D.4). The points represent measurements and the solid curve theoretical values. The calibration curves are: $z = a_0\lambda^2 + a_1\lambda + a_0$, and $z = b_0(\frac{1}{k})^2 + b_1\frac{1}{k} + b_0$ viceversa, where a_2, a_1, a_0 and b_2, b_1, b_0 are the calibration coefficients.

3.6. Conclusions

We have characterized the digital interference instrument in terms of scanning parameters. They are: the wavelength range of the source, the axial size of the object, and the axial resolution of the system. In the following, we will optimize and evaluate the DIH technique in imaging and characterize human, animal tissue and fingerprint patterns.

3.7. Bibliography

[1] Patel D V and McGhee C N 2007 Contemporary in vivo confocal microscopy of the living human cornea using white light and laser scanning techniques: a major review *Clin. Experiment. Ophthalmol.* **35** (1) 71-88

[2] Huang D *et al* 1991 Optical coherence tomography *Science* **254** 1178–81

[3] Fujimoto J G, Brezinski M E, Tearney G J, Boppart S A, Bouma B, Hee M R, Southern J F and Swanson E A 1995 Optical biopsy and imaging using optical coherence tomography *Nature Med.* **1** 970–72

[4] Srinivasan V J, Huber R, Gorczynska I and Fujimoto J G 2007 High-speed, high-resolution optical coherence tomography retinal imaging with a frequency-swept laser at 850 *Optics Letters* **32**(4) 361-63

[5] Hiratsuka H, Morisak K and Yoshimur T 2000 Optical Coherence Tomography System based on Synthesis of Optical Coherence Function With a Wavelength-Scanning Laser Source *Optical Review* **7**(5) 442-47

[6] He Z and Hotate K 1999 Synthesized optical coherence tomography for imaging of scattering objects by use of a stepwise frequency-modulated tunable laser diode *Optics Letters* **24**(21) 1502-04

[7] Yamamoto A, Kuo C, Sunouchi K, Wada S, Yamaguchi I and Tashiro H 2001 Surface Shape Measurement by Wavelength Scanning Interferometry Using an Electronically Tuned Ti:Sapphire Laser *Optical Review* **8**(1) 59-63

[8] Yamaguchi I, Yamamoto A and Yano M 2000 Surface topography by wavelength scanning interferometry *Opt. Eng.* **39**(1) 40–46

[9] Ansari Z et al 2002 Wide-field, real time depth-resolved imaging using structured illumination with photorefractive holography *Applied Physics Letter* **81** 2148-50

[10] Gabor D 1971 Holography *Nobel Lecture*

[11] Goodman J W and Lawrence R W 1967 Digital image formation from electronically detected holograms *Appl. Phys.Lett.* **11** 77-79

[12] Schnars U 1994 Direct phase determination in hologram interferometry with use of digitally recorded holograms *J. Opt. Soc. Am*. A **11** 2011-5

[13] Schnars U and Jueptner W 1994 Direct recording of holograms by a CCD target and numerical reconstruction *Appl.Opt.* **33** 179–181

[14] Schnars U and Jueptner W 2002 Digital recording and numerical reconstruction of holograms *Meas. Sci. Technol.* **13** R85-R101

[15] Yamaguchi I, Kato J, Ohta S and Mizuno J 2001 Image formation in phase-shifting digital holography and applications to microscopy *Appl. Optics* **40** 6177-86

[16] Yamaguchi I and Zhang T Phase-shifting digital holography 1997 *Opt. Lett*. **22** 1268

[17] Zhang T and Yamaguchi I 1998 Three-dimensional microscopy with phase-shifting digital holography *Opt. Lett.* **23** 1221

[18] Poon T C 2003 Three-dimensional image processing and optical scanning holography *Adv. Imaging & Electron Phys*. **126** 329-50

[19] Yamaguchi I, Matsumura T and Kato J 2002 Phase-shifting color digital holography *Opt. Lett*. **27** 1108

[20] Barty A, Nugent K A, Paganin D and Roberts A 1998 Quantitative optical phase microscopy *Opt. Lett*. **23** 817

[21] Cuche E, Bevilacqua F and Depeursinge C 1999 Digital holography for quantitative phase-contrast imaging 1999 *Opt. Lett*. **24** 291

[22] Ferraro P, De Nicola S, Finizio A, Coppola G, Grilli S, Magro C and Pierattini G 2003 Compensation of the inherent wave front curvature in digital holographic coherent microscopy for quantitative phase-contrast imaging *Appl. Opt.* **42** 1938-46

[23] Xu M L, Peng X, Miao J and Asundi A 2001 Studies of digital microscopic holography with applications to microstructure testing Appl. Opt. 40 5046-51

[24] Pedrini G and Tiziani H J 1997 Quantitative evaluation of two-dimensional dynamic deformations using digital holography *Opt. Laser Technol*. **29** 249–56

[25] Picart P, Leval J, Mounier D and Gougeon S 2005 Some opportunities for vibration analysis with time averaging in digital Fresnel holography *Appl. Opt*. **44** 337–43

[26] Haddad W S, Cullen D, Solem J C, Longworth J W, McPherson A, Boyer K and Rhodes C K 1992 Fourier-transform holographic microscope *Appl. Opt*. **31** 4973-8

[27] Xu W, Jericho M H, Meinertzhagen I A and Kreuzer H J 2001 Digital in-line holography for biological applications *Proc. Natl. Acad. Sci. USA* **98** 11301-05

[28] Kim MK 1999 Wavelength scanning digital interference holography for optical section imaging *Opt. Letters* **24** 1693

[29] Kim MK 2000 Tomographic three-dimensional imaging of a biological specimen using wavelength-scanning digital interference holography *Opt. Express* **7** 305-10

[30] Dakoff A, Gass J and Kim M K 2003 Microscopic three-dimensional imaging by digital interference holography *J. Electr. Imag*. **12** 643-647

[31] Yu L, Myung M K 2005 Wavelength scanning digital interference holography for variable tomographic scanning *Opt. Express* **13** 5621-7

[32] Yu L, Myung M K 2005 Wavelength-scanning digital interference holography for tomographic 3D imaging using the angular spectrum method *Opt. Lett*. **30** 2092

[33] Kim M K, Yu L and Mann C J 2006 Interference techniques in digital holography *J. Opt. A: Pure Appl. Opt*. **8** 512-23

[34] Gass J, Dakoff A and Kim M K 2003 Phase imaging without 2-pi ambiguity by multiwavelength digital holography *Opt. Lett*. **28** 1141-3

[35] Mann C J, Yu L, Lo C M and Kim M K 2005 High-resolution quantitative phase-contrast microscopy by digital holography *Opt. Express* **13** 8693-98

[36] Parshall D and Kim M K 2006 Digital holographic microscopy with dual wavelength phase unwrapping *Appl. Opt.* **45** 451-59

[37] Mann C, Yu L and Kim M K 2006 Movies of cellular and sub-cellular motion by digital holographic microscopy *Biomed. Engg. Online* **5** 21

[38] Sarunic M V, Weinberg S, and Izatt J A 2006 Full-field swept-source phase microscopy *Opt. Lett*. **30** 1462-64

[39] Massatsch P, Charriere F, Cuche E, Marquet P, and Depeursinge C D 2005 Time-domain optical coherence tomography with digital holographic microscopy *Appl. Opt*. **44** 1806-12

[40] Yu L and Chen Z 2007 Digital holographic tomography based on spectral interferometry Opt. Lett. **32**, 3005-07

[41] Ellerbee A K, Creazzo T L and Izatt J A Investigating nanoscale cellular dynamics with cross-sectional spectral domain phase microscopy *Opt. Express* **15** 8115-24

[42] Yu L and Chen Z 2007 Improved tomographic imaging of wavelength scanning digital holographic microscopy by use of digital spectral shaping *Opt. Express* **15** 878-86

[43] Montfort F, Colomb T, Charrière F, Kühn J, Marquet P, Cuche E, Herminjard S, and Depeursinge C 2006 Submicrometer optical tomography by multiple-wavelength digital holographic microscopy *Appl. Opt.* **45** 8209-17

[44] Meneses-Fabian C, Rodriguez-Zurita G, and Arrizn V 2006 Optical tomography of trans-parent objects with phase-shifting interferometry and stepwise-shifted Ronchi ruling *J. Opt. Soc. Am.* A **23** 298-305

[45] Gorski W 2006 Tomographic microinterferometry of optical fibers Optical Engineering **45** 125002

[46] Charriere F, Pavillon N, Colomb T, Heger T, Mitchell E, Marquet P, Rappaz B, and Depeursinge G 2006 Living specimen tomography by digital holographic microscopy: morphometry of testate amoeba *Opt. Express* **14** 7005-13

[47] Charriere F, Marian A, Montfort F, Kuhn J, Colomb T, Cuche E, Marquet P, and Depeursinge C 2006 Cell refractive index tomography by digital holographic microscopy *Opt. Lett*. **31** 178-180

[48] Vishnyakov G N, Levin G G, Minaev V L, Pickalov V V, and Likhachev A V 2004 Tomographic Interference Microscopy of Living Cells *Microscopy and Analysis* **18**15-17

[49] Choi W, Fang-Yen C, Badizadegan K, Oh S, Lue N, Dasari R R, and Feld M S 2007 Tomographic phase microscopy *Nature Methods* **4** 717-19.

[50]. N. Warnasooriya & MK Kim, "LED-based multi-wavelength phase imaging interference microscopy", *Opt. Expr*. 15, 9239-9247 (2007).

[51]. D. Parshall & M.K. Kim, "Digital holographic microscopy with dual wavelength phase unwrapping", *Appl. Opt*. 45, 451-459 (2006).

[52]. C.J. Mann, L. Yu, C.M. Lo, & M.K. Kim, "High-resolution quantitative phase-contrast microscopy by digital holography", *Opt. Express* 13, 8693-8698 (2005). (An image from this paper was featured on the masthead of the issue.)

[53]. C. Mann, L. Yu, & M.K. Kim, "Movies of cellular and sub-cellular motion by digital holographic microscopy", *Biomed. Engg*. Online, 5, 21 (2006).

[54]. A Khmaladze, MK Kim, & CM Lo, "Phase imaging of cells by simultaneous dual-wavelength reflection digital holography," *Opt. Express* 16, 10900-10911 (2008).

CHAPTER 4

OPTIMIZATION OF DIGITAL INTERFERENCE HOLOGRAPHY

In the previous chapter, we presented the principle of the digital interference holography and the fundamental parameters that characterize the digital interference holography system. An improved digital interference holography (DIH) technique is proposed. This technique incorporates a dispersion compensation algorithm to minimize the phase variation in the system. Using this instrument we acquired successfully tomographic images of the resolution target wrapped with scotch tape with a signal-to-noise ratio of about 50 dB. To demonstrate the capabilities of our system we also reconstructed tomographic and volume fundus images in human and animal eyes with narrow axial resolution less than 5 μm. The chapter is organized as follows: Section 4.1 describes the dispersion compensation based on wavelength. The significance of the signal-to-noise ratio in DIH system is presented in Section 4.2. In Section 4.3 are shown various results. Conclusions are presented in Section 4.4.

4.1. Dispersion Compensation-Phase Matching

Tunable lasers are particularly sensitive to chromatic-dispersion, $n(\lambda)$, characteristics of materials, in particular second-order k'' and third order dispersion k''', which typically cause broadening of the axial point spread function [3]. Any mismatch in the length of

the reference and sample arms of the interferometer will generate wavelength dependent phase error. Precise measurements of any sample characteristics using tunable lasers acquire accurate measuring of the media dispersion effect in the sample arm of the interferometer. Recent studies have been reported to measure the refractive index of ocular media using white-light interferometry [4]. The study concluded the dispersion of aqueous and vitreous humors for bovine, monkey, goat, and rabbit did not vary from the dispersion of water. Numerous approaches have been used to measure the second order dispersion. The most common method is to insert a dispersive material in the reference arm to compensate the sample dispersion in the object arm [5, 6]. A numerical dispersion compensation method was introduced for optical coherence tomography [7] to compensate for the depth resolution loss. It is based on the correlation of the depth scan signal with a depth-dependent correlation kernel taken as a Gaussian temporal distribution. Another numerical compensation of dispersion mismatch was demonstrated in real space directly to experimental hologram using wavenumber scanning. The cosine function (that contains the dispersion mismatch ϕ_i) in the expression of the interferogram is transformed to a complex function followed by multiplication with an $\exp(-j\phi_i)$ in the complex Fourier transform operation [8, 10].

In DIH [13, 14], the laser beam is tuned from short to high wavelengths. The phase calculated by digital holography is given by $\varphi = kz = 2\pi z / \lambda$, where z is the distance of an object point relative to the position of the reference mirror and λ is the wavelength of the laser. Uncertainty in k or z leads to phase error, which needs to be corrected for. Dispersion error (uncertainty in k) tends to have severe effect on the accuracy due to its accumulative nature. Short wavelengths are associated with higher frequency periodicity

of interference while long wavelengths are associated with a slow periodicity of interference. As the optical path difference between the reference and the object arms increases, ex. because of the ocular media, the modulation across the spectrum increases in frequency because short wavelengths accumulate more phase than longer wavelengths do [9]. All optical components and ocular media dispersion contribute to the distortion of the spectrum. The function $\phi(k)$ is not linear with respect to the wavenumber $k = 2\pi / \lambda$. This function can be expanded in Taylor series, around the center wavenumber $k_c = 2\pi / \lambda_c$, with λ_c being the center wavelength.

$$\phi(k) = \phi(k_c) + \left. \frac{\partial \phi(k)}{\partial k} \right|_{kc} (k_c - k) + \frac{1}{2} \left. \frac{\partial^2 \phi(k)}{\partial k^2} \right|_{kc} (k_c - k)^2 + ... + \frac{1}{n!} \left. \frac{\partial^n \phi(k)}{\partial k^n} \right|_{kc} (k_c - k)^n \qquad ..(4.1)$$

The dispersion components are: first term is a constant offset, second term is the group-delay, third term is the group-velocity dispersion or chromatic dispersion, and the last term represents higher order dispersion. The third term in the Equation (4.1) is the cause of the broadening of the input signal as it travels through a dispersive media. This fact has a direct impact in worsening of the axial resolution and the signal to noise ratio of the optical field superposition. The process of dispersion-compensation becomes complicated due to the higher order terms in Equation (4.1).

We employed the following method to estimate the phase corrections. For example, from each hologram $H(\lambda_n)$, a 3D object field is reconstructed. The expression of the free error phase of this field is given in the Equation (4.2). It has a 2D phase profile at a suitable value of z that corresponds to the location of the object,

$$\phi_n(x, y) = \phi_{n\,O-rec}(x, y) = \text{phase}\{obj(x, y, z; \lambda_n)\} = k_n z \qquad (4.2)$$

61

where k_n are various wavenumbers , and $k_n z$ are the free error phases for each of k_n's. Next step is to calculate the difference profiles,

$$\delta\phi_n(x,y) = \phi_n(x,y) - \phi_{n-1}(x,y) = \delta k \cdot z(x,y) \tag{4.3}$$

where $z(x,y)$ is the z-profile of the object being imaged. If there are not errors in the wavenumber estimation, then all $\delta\varphi_n$'s for various n's should be identical since δk's are perfectly equally spaced between holograms. Otherwise, the uncertainties introduce phase error, $\varepsilon_n = \Delta k_n z$, so that the Equation (4.3) will become,

$$\phi_n'(x,y) = (k_n + \Delta k_n) \cdot z = \phi_n(x,y) + \varepsilon_n \tag{4.4}$$

where Δk is the deviation from the nominal constant k , and the new difference profile,

$$\delta\phi_n'(x,y) = \phi_n'(x,y) - \phi_{n-1}'(x,y) = \delta k \cdot z(x,y) + (\varepsilon_n - \varepsilon_{n-1}) \tag{4.5}$$

The idea is to find the series $\varepsilon_2, \varepsilon_3, ..., \varepsilon_n$ that makes $\delta\phi_2, \delta\phi_3, ..., \delta\phi_n$ as identical as possible. This is done by taking the difference $\delta\phi_{n-1}'(x,y) - \delta\phi_1'(x,y) + \varphi$, modulo 2π , and find ε_n's by minimizing $\sum_{x,y}\left|\delta\phi_{n-1}'(x,y) - \delta\phi_1'(x,y) + \varphi\right|$ versus the variable φ. This procedure assumes that $z(x,y)$ is a well-defined 2D function, and gives very accurate and straightforward estimate of ε's. With diffuse or multilayered objects, it is more difficult to obtain completely deterministic procedures to obtain ε's. In that case, one needs to reduce the domain (x,y) to an area of the object known to have a well-defined single-surface profile.

4.2. Signal – to – Noise Ratio

Addition of a series of N cosines or imaginary exponentials yields: $S = \dfrac{1}{N} \sum\limits_{n=1}^{N} \exp(in\delta kz)$,

so that $|S|^2 = \dfrac{\sin^2(N\pi z/\Lambda)}{N^2 \sin^2(\pi z/\Lambda)}$, where $\delta k = 2\pi/\Lambda$. The signal to noise ratio (SNR) of the

peaks at $z = 0, \Lambda, \ldots$ grows proportional to N^2, while the width of the peak narrows as

$\delta \sim \Lambda/N$. This behavior of the SNR and resolution is achieved only if all the amplitudes

and phases of cosines are identical. Each hologram captured by the camera is normalized

by the 2D average of each hologram to compensate for the laser power variation across

the tuning range.

$$H_{norm}(x_h, y_h; \lambda_n) = \frac{H(x_h, y_h; \lambda_n)}{\sum_{x_h, y_h} H(x_h, y_h; \lambda_n)/N_x N_y} \tag{4.6}$$

4.3. Results

4.3.1. Resolution Target

We used a U.S. Air Force resolution target, with an area of 1040 x 1040 μm^2, 256 x 256

pixels, as a standard to calibrate the system. The area selected in the Figure 4.1a

represents group 2, element 3 and group 4 elements 2, 3, 4, 5, 6 of the resolution target.

The bars in group 4, element 6 with 17.54 μm width are evident. The reconstruction

distance z, representing the distance from the object to the hologram plane is 643.56 μm.

The complex field of the resolution target is computed separately for 50

wavelengths by numerical diffraction using the angular spectrum method, which gives an

axial range of $\Lambda = 500\mu m$ and axial resolution of $\delta z = 10\mu m$. All 3D electric fields are

added together to obtain a 3D electric field of the object being imaged. Cross-sections of

the volume can be taken in the x, y, and z planes. Cross-sectional images in the y-z planes Figure 4.1b, and x-z planes Figure 4.1c, are shown below. The resolution target is an object without internal structure and the reflection of the laser beam takes place at the surface of the resolution target. A piece of clear tape is placed on top of the resolution target to provide a second surface for demonstration of tomographic imaging. The first layer (interrupted) in Figure 4.1b, 4.1c is the reflection that comes from the chromium coated surface. The second layer that can be seen in Figure 4.1b, 4.1c is the reflection from the attached tape surface.

a)   b)   c)
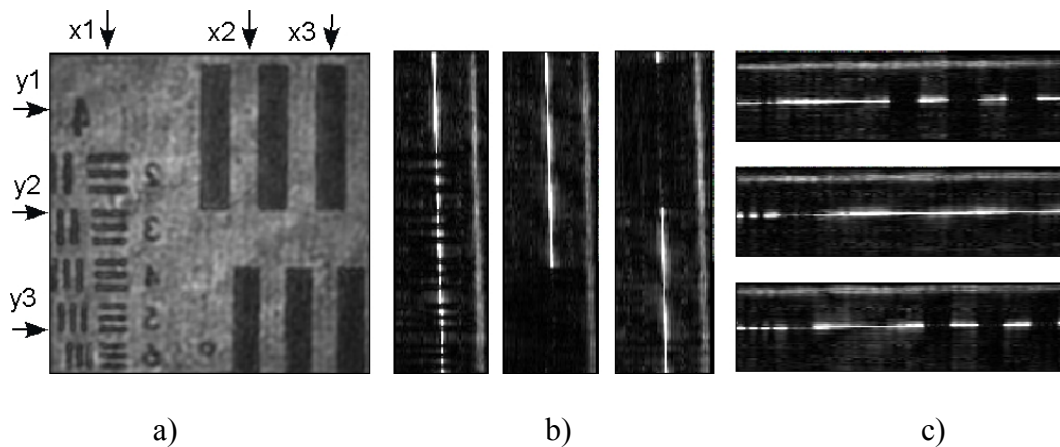
Figure 4.1. The Reconstructed Volume of the Resolution Target: (a) x-y cross-section, 1040 x 1040 μm^2. (b) y-z cross sections at various x values, 500 x 1040 μm^2, from left to right, x1, x2, and x3. (c) x-z cross sections at various y values, 1040 x 500 μm^2, from top to bottom, y1, y2, and y3.

We have tested the improvement of SNR with increasing number of holograms N. As described above, the SNR is expected to grow as N^2. As seen in Figure 4.2, the 4-fold increase in N from 100 to 400 lowers the noise from -30 dB to about -45 dB, which is consistent with $10 \cdot \log 16 = 12 dB$. This data set is without the clear tape attachment.
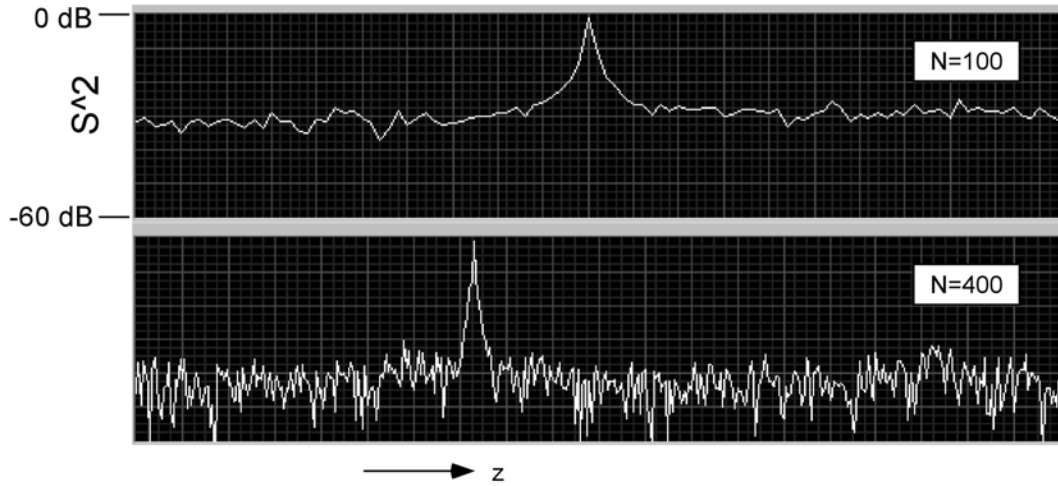
Figure 4.2. Signal-to-Noise-Ratio Improvement. The peak in each semi-log graph represents the surface of resolution target. As N increases four-fold the SNR increases by 12 dB, as expected.

4.3.2 Biological Samples: Pig Retina

In the following, we present a few examples of tomographic imaging of biological specimens using digital interference holography. Figure 4.3 and Figure 4.4 are images of a porcine eye tissue provided by the Ophthalmology Department at the USF. It was preserved in formaldehyde, refrigerated and a piece of the sclera, with retinal tissue attached, was cut out for imaging. The holographic image acquisition and computation of

the optical field are carried out for each of 50 wavelengths in the range from 565 nm to 602 nm. Superposition of images, in DIH processes described above, reveals the principal features of the retinal anatomy. The imaged surface areas are 0.67 x 0.67 mm^2 for Figure 4.3 and 1.04 x 1.04 mm^2 for Figure 4.4. The axial range $\Lambda = 500 \mu m$ and axial resolution $\delta z = 10 \mu m$ for both image sets. The measured SNR for these images was about 45~55 dB.

In Figure 4.3, the images reveal convex surfaces of blood vessels, as well as about $150 \mu m$ thick layer of retina on top of the choroidal surface. Apparently, the blood vessels in figure Figure 4.3 were fixed with blood in them, while figure Figure 4.4 shows mostly empty and flattened blood vessels. In fact, the preparation and handling of the tissue sample resulted in tear of some of the retinal tissue. Thus the upper right half of Figures 4.4 has intact retinal tissue, while the lower left half is missing the retinal layer and the choroids surface is exposed. In Figure 4.4b, the boundary marked 'c' is the bare choroidal surface, while the surface 'a' is the choroidal surface seen through the retinal surface 'b'. The index of refraction of the retinal layer causes the choroidal surface to appear at a different depth compared to the bare surface, causing the break in the outline of the choroidal surface in Figures 4.4b and Figures 4.4c.
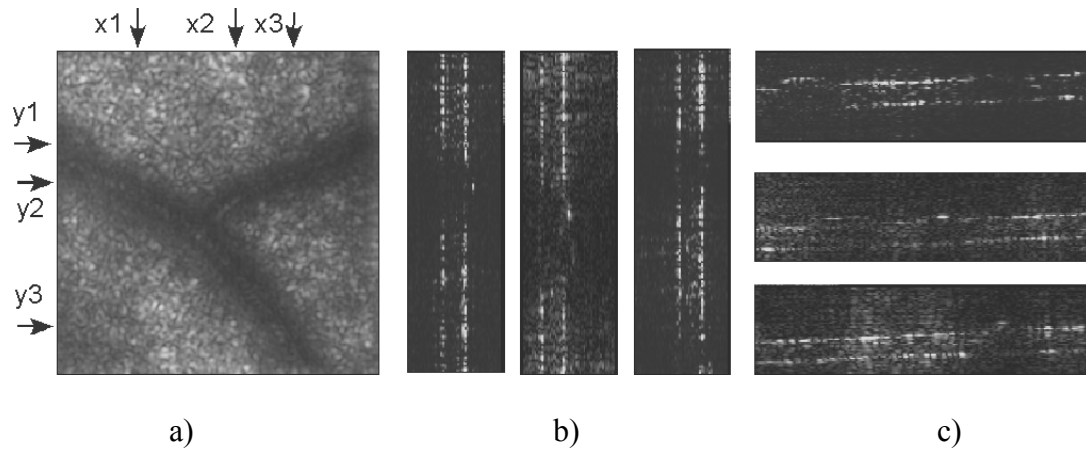
Figure 4.3. The Reconstructed Volume of the Retina with Filled Blood Vessels: (a) x-y cross-section, 670 x 670 μm^2. (b) y-z cross section along x1, 500 x 670 μm^2. (c) x-z cross sections at various y values, from top to bottom, y1 and y2, 670 x 500 μm^2.
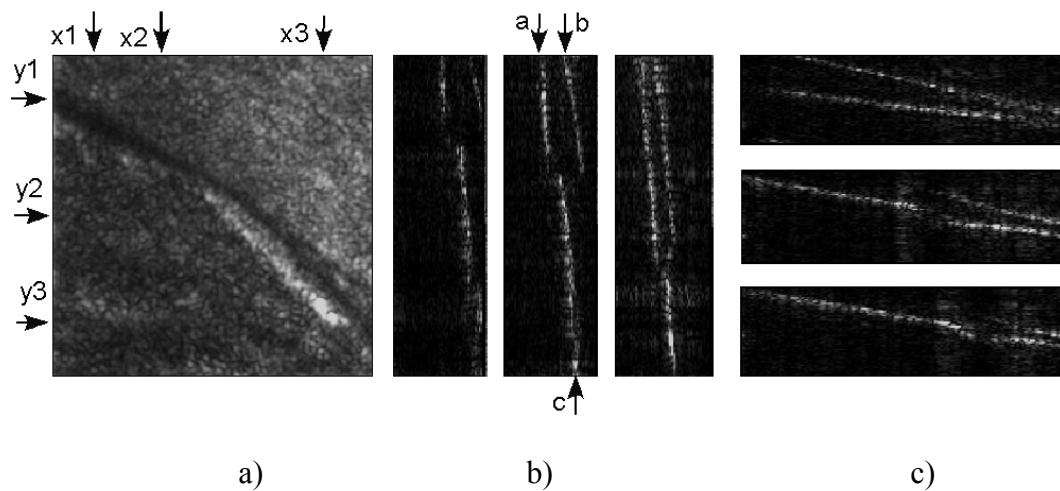

Figure 4.4. The Reconstructed Volume of the Retina with Empty Blood Vessels: (a) x-y cross-section, 1040 x 1040 μm^2. (b) y-z cross sections along x1, x2, and x3, 500 x 1040 μm^2. (c) x-z cross sections at various y planes, from top to bottom, y1, y2 and y3, 1040 x 500 μm^2.

67

The dispersion-compensation method is applied to all reconstructed samples from above. As an example the phase matching technique was demonstrated on human macula. The imaged surface area is 5020 x 5020 mm^2, Figure 4.5a, with a physical axial range $\Lambda = 209.75\mu m$ and physical axial resolution $\delta z = 4.19\mu m$. Tomographic images of the human macula are shown in Figure 4.5b, and Figure 4.5c respectively. Nerve fiber layer and retinal pigment epithelium are emphasized in Figure 4.5b by applying the phase correction. The optical thickness between the retinal nerve fiber layer (NFL) and the retinal pigment epithelial layer (RPE) is about $84\mu m$.
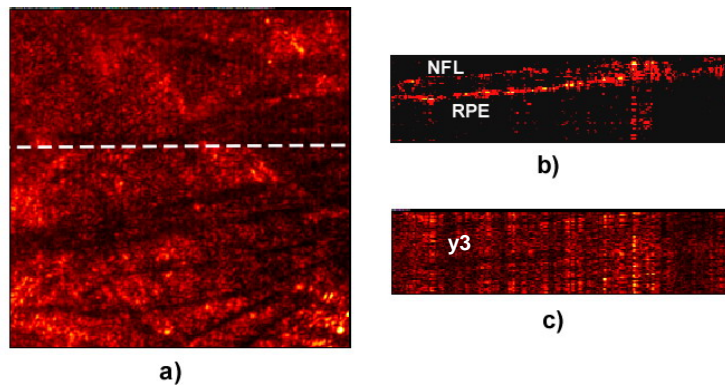
Figure 4.5. Phase-Matching Demonstration on Human Macula Sample: a) x-y cross-section, FOV=5000 x 5000 μm^2; b) x-z cross section along the dashed line from Figure 4.5a, 5020 x 209.75 μm^2 with the phase-matching scheme included; c) x-z cross sections along the dashed line from fig.3a, 5020 x 209.75 μm^2 without phase-matching scheme included; $\Delta\lambda$: 0.560-0.600 μm; $\delta z = 4.19\mu m$; $\delta x = \delta y = 19.6\mu m$; NX= NY=256 pixels; NZ= 50 pixels.

4.4. Conclusion

We have presented results of imaging experiments using digital interference holography. Calibration experiments using resolution target demonstrates improvement of SNR with increasing number of holograms consistent with theoretical prediction. Imaging experiments on retinal tissue reveal topography of blood vessels as well as optical thickness profile of the retinal layer. The SNR of tissue images is comparable to that of resolution target, implying the imaging system is operating at close to theoretical optimum. Further improvement in SNR may be achieved if the hologram number N is increased further. At this point, however, imperfection in the phase matching scheme seems to be limiting such improvement. Modification of the hologram exposure method have to be made so that the holograms are taken at equal intervals of wave vectors, not wavelengths, as well as automatically minimize the reference-object distance difference by a simple interferometric tracking and feedback. The next chapter covers the in-vitro imaging of the human ophthalmic tissue using DIH, and a comparison of ophthalmic devices capabilities is given relative to the DIH.

Acknowledgments

4.5. Bibliography

[1]. Kim, M.K., Yu, L., and Mann C.J., "Interference techniques in digital holography", J. Opt. A: Pure Appl. Opt. 8, 512-23 (2006).

[2]. Potcoava, M.C., and Kim, M.K., "Optical tomography for biomedical applications by digital interference holography", Meas. Sci. Technol., 19, 074010 (2008).

[3]. C. K. Hitzenberger, A. Baumgartner, W. Drexler, and A. F. Fercher, "Dispersion effects in partial coherence interferometry: implications for intraocular ranging," J. Biomed. Opt. 4, 144–151 (1999).

[4]. Hammer D.X., Welch A.J., "Spectrally resolved white-light interferometry for measurement of ocular dispersion", J. Opt. Soc. Am. A., 16, 2092-2102 (1999).

[5]. C.K. Hitzenberger, A. Baumgartner, W. Drexler, A.F. Fercher, "Dispersion effects in partial coherence interferometry: implications for intraocular ranging," J. Biomed. Opt. 4, 144-151 (1999).

[6]. Drexler, W., Morgner, U., Kärtner, F. X., Pitris, C., Boppart, S. A., Li , X. D., Ippen , E. P., and Fujimoto , J. G., "*In vivo* ultrahigh-resolution optical coherence tomography", *Opt. Lett*., 24 1221-1223 (1999).

[7]. Fercher, A. F., Hitzenberger, C. K., Sticker, M., Zawadzki, R., Karamata, B., Lasser, T., "Numerical dispersion compensation for Partial Coherence Interferometry and Optical Coherence Tomography", Opt. Express 9 12, 610-615 (2001)

[8]. Choi, D., Hiko-Oka, H., Amano, T., Furukawa, H., Kano, Nakanishi, F., M., Shimizu, K., and Ohbayashi, K., "Numerical compensation of dispersion mismatch in discretely swept optical-frequency-domain-reffectometry optical coherence tomography," Jpn. J. Appl. Phys. Part 1 45, 6022–6027 (2006).

[9]. Tumlinson, A.R., Hofer, B., Winkler, A.M., Povazay, B., Drexler, W., Barton, J.K.," Inherent homogenous media dispersion compensation in frequency domain optical coherence tomography by accurate k-sampling", Appl Opt. 47, 687-93 (2008).

[10]. Cense, B., and Nassif, N.A., "Ultrahigh-resolution high-speed retinal imaging using spectral-domain optical coherence tomography", Opt. Express 12, 2435-2447 (2004).

CHAPTER 5

IN-VITRO IMAGING OF OPHTHALMIC TISSUE BY DIGITAL

INTERFERENCE HOLOGRAPHY

This chapter introduces the in-vitro imaging of human optic nerve head and retina by the digital interference holography. Samples of peripheral retina, macula, and optic nerve head from two formaldehyde-preserved human eyes were dissected and mounted onto slides. Holograms were captured by a monochrome CCD camera (Sony XC-ST50, with 780 x 640 pixels and pixel size of ~ 9 μm). Light source was a solid-state pumped dye laser with tunable wavelength range of 560-605 nm. Using about 50 wavelengths in this band, holograms were obtained and numerically reconstructed using custom software based on NI LabView. Tomographic images were produced by superposition of holograms. Section 5.1 reviews some of the eye fundus diseases identified with existent ophthalmic devices. Section 5.2 gives details of samples preparation and ophthalmic tissue. Section 5.3 discusses the experimental setup for ophthalmic imaging. Section 5.4 presents experimental results. Finally section 5.5 concludes this chapter.

5.1. Introduction

Imaging methods have become a critical player in the field of ophthalmology, and currently the clinical ophthalmologist depends heavily on such imaging to guide

diagnosis and treatment decisions. The optic nerve and macula are emphasized in current-day ocular imaging. Diseases of optic nerve (glaucoma) and macula (age related macular degeneration, epiretinal membrane, cystoid or diabetic macular edema) can be objectively diagnosed and monitored with the aid of optical imaging techniques. For glaucoma management, accurate evaluation and assessment of optic disc topography and neuroretinal rim area is helpful for tracking glaucomatous change [1-8]. Macular thickness - in particular nerve fiber layer and ganglion cell layer thickness - may also be important in evaluating glaucomatous changes [9,10]. Studies have shown correlations between optic nerve cup measurements (cup volume, the ratio of cup area to disc area, and cup shape) and nerve fiber number [9].

Treatment of macular diseases, such as age-related macular degeneration and cystoid macular edema, depends on accurate knowledge of retinal thickness and microanatomy. Drusen can be identified in dry macular degeneration with tomographic imaging techniques; more importantly, subretinal fluid can be identified in exudative macular degeneration. Epiretinal membranes can be visualized above the nerve fiber layer and aid in surgical planning. Macular edema, often difficult to assess clinically, can be easily diagnosed and objectively followed throughout treatment to mark resolution of intraretinal fluid by tomographic imaging.

Digital Interference holography (DIH) is similar to OCT, in that it offers rapid 3D imaging with theoretically higher resolution [17-25]. The goal of the present study is to evaluate the thickness of the macula and to quantify optic nerve head characteristics (shape, diameter, cup depth, and cup width), using micrometer resolution DIH. DIH may provide another option in ocular imaging, potentially providing high resolution 3D

73

information which could potentially aid in guiding diagnosis and treatment of many ocular diseases.

5.2. Methods

5.2.1 Specimen Preparation

Each of the two formaldehyde-preserved human eyes were obtained from the Lions Eye Institute for Transplant & Research (Tampa, FL) and dissected into two hemispheres. Sample preparation was performed under a microscope to minimize tissue damage. The inner vitreous was peeled away using tweezers and the sclera was removed using microforceps. Samples of the peripheral retina, macula, and the optic nerve head were removed and flat-mounted on microscope slides. Due to desiccation of tissue, measured macula thickness and optic disc parameters are smaller compared to normal values. The research did not meet the USF definition of human research activities; therefore, IRB approval was not required.

5.2.2 Macula and Optic Nerve Characteristics

The term "macula" clinically refers to the area of the retina within the temporal vascular arcades, typically spanning a diameter of 5-6mm. Histologically, it is a region with multiple layers of ganglion cell nuclei. The neurosensory retina can be divided into several layers which include (from anterior to posterior): internal limiting membrane, nerve fiber layer, ganglion cell layer, inner plexiform layer, inner nuclear layer, outer plexiform layer, outer nuclear layer, inner and outer segments of photoreceptors, and

retinal pigment epithelium. Studies report central foveal thickness in normal patients to be an average of 182 microns by OCT measurement [28, 32].

A schematic of optic disc head geometry is shown in Figure 5.1. The anterior surface of the optic nerve is visible ophthalmoscopically as the optic disc, and oval structure measuring 1.5 mm horizontally and 1.75 mm vertically, with a depression known as the physiologic cup located slightly temporal to the geometric center of the disc. The central retinal artery passes through this cup, vascularizing the retina. The optic nerve head consists of four parts: the superficial nerve fiber layer, the prelaminar region, the laminar region, and the retrolaminar region. Glaucoma damages the superficial nerve fiber layer [26].
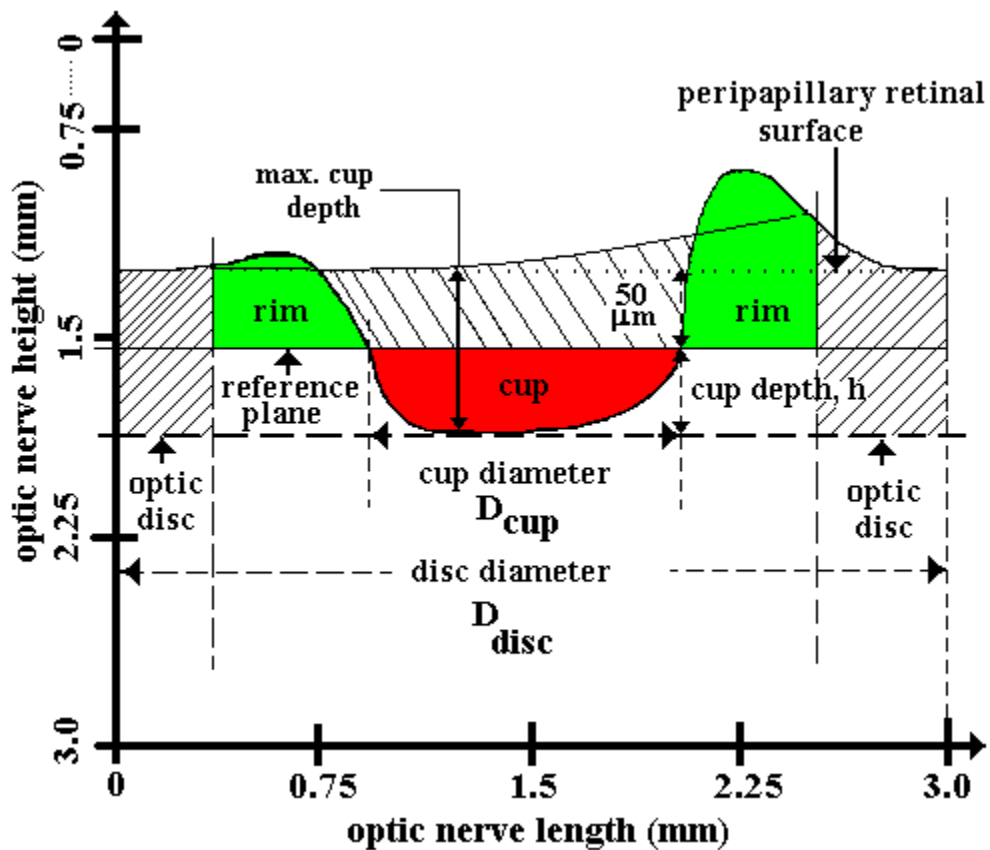

Figure 5.1. Optic Disc Geometry and Parameter Representation.

5.3 Theory

A hologram can record all information present in a wave front, including both amplitude and phase. For this reason it can reproduce the three-dimensional structure wavefront of the object. In DIH [17-25] images are reconstructed from a number of 2D digitally-recorded holograms while the wavelengths are varied at regular intervals. The amplitude and phase information of the optical field are reconstructed from the digitally recorded holograms using the angular spectrum method [21-24, 33].

The optical field, $E(x, y; z)$, is assumed to be a solution of the wave equation in the frequency domain (paraxial or Helmholtz equation) that has the form, $(\nabla^2 + k^2)E(x, y; z) = 0$, where $k^2 = k_x^2 + k_y^2 + k_z^2$, k being the wavenumber or modulus $(= 2\pi/\lambda)$ of the propagation vector, and k_x, k_y, k_z represent spatial frequencies along x, y, z respectively. One way to solve the wave equation is to use the angular spectrum method [21-24, 33]. Starting at the hologram plane where $z = 0$ (aperture plane), the Fourier transform of the optical field, $E(x, y; 0)$, represents the angular spectrum at that plane, $A_0(k_x, k_y; 0)$. A complex transfer function is used to propagate the angular spectrum along z axis toward the reconstruction plane at z = Z, and the angular spectrum becomes, $A(k_x, k_y; z) = A_0(k_x, k_y; 0)\exp(ik_z z)$. The field at any other z-plane can be calculated with just one inverse Fourier transform of the angular spectrum at that plane. The superposition of the multiple three-dimensional reconstructed optical fields yields tomographic images with narrow axial resolution. The range of physical sizes and resolution of objects are controlled by the proper choice of wavelength interval.

Under the Huygens principle, the source is treated as many individual point sources, located at r_P from the center of the source, Figure 5.2.
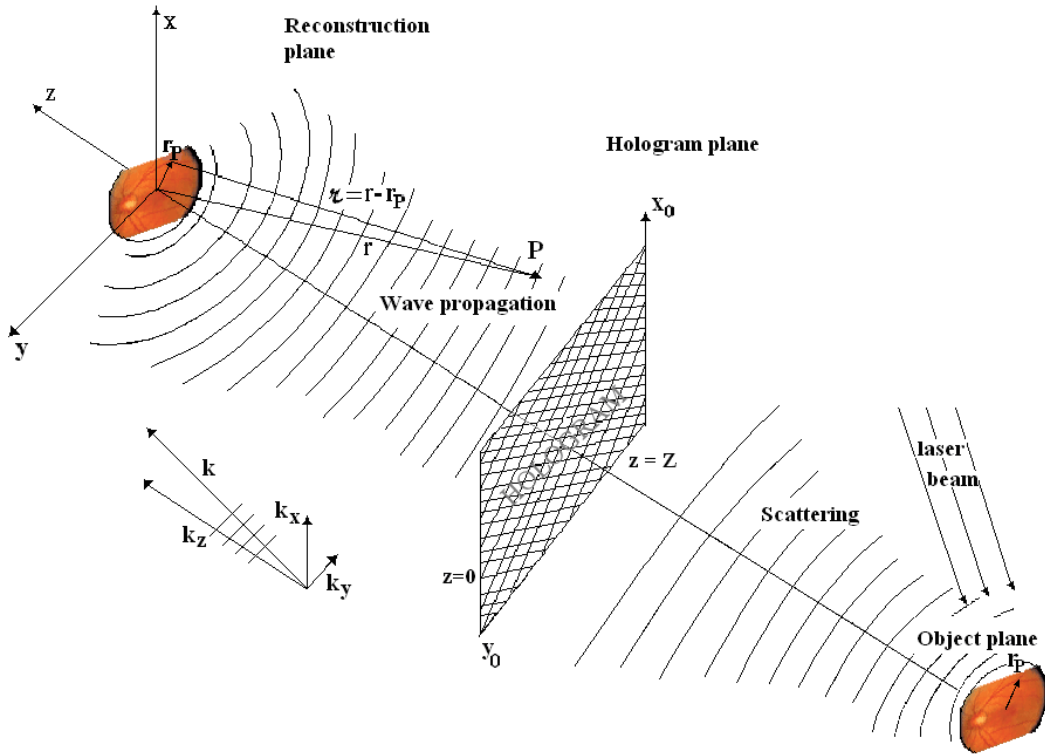
Figure 5.2. Sketch of Object, Hologram and Reconstruction Planes. Illustration of the object wave scattered off the object points and the propagate of the real image wave r to the reconstruction planes; k_x, k_y, k_z represent the spatial carrier frequencies in the frequency space, imparted by the offset angle of the reference wave with respect to the optical axis of the scattered wave.

Scatter from a point initiates spherical waves. When an object is illuminated by a laser beam of wavelength λ, each point on a wave front serves as a source of secondary spherical wavelets, $O(r_P)\exp(ik|r - r_P|)$, where the object function $O(r_P)$, is proportional to the amplitude and phase of the wavelet scattered or emitted by object point. The object

field, $E_{OBJ-\lambda i}$ for a specific wavelength interferes with the reference field, $E_{REF-\lambda i}$ at the hologram plane and the amplitude and phase of the object field at the hologram plane are recorded by the hologram, in form of intensity, $H(x_h, y_h, \lambda_i)$.

$$H(x_0, y_0, \lambda_i) = |E_{OBJ-\lambda i}|^2 + |E_{REF-\lambda i}|^2 + E_{OBJ-\lambda i} \cdot E_{REF-\lambda i}^* + E_{OBJ-\lambda i}^* \cdot E_{REF-\lambda i} \quad (5.1)$$

The first two terms represent the zero-order term and the third and forth represent the two conjugate images, virtual and real. We call the optical field at the hologram plane, $E_0(x_0, y_0; z_0)$. Accordingly, a complex field $E_0(x_0, y_0; z_0)$ at a position vector $(x_0, y_0; z_0 = 0)$ can be decomposed into its spectrum of plane-wave components $A_0(k_x, k_y; 0)$ defined by the Fourier transform,

$$A_0(k_x, k_y; 0) = \iint E_0(x_0, y_0; z_0) \exp[-i(k_x x_0 + k_y y_0)] dx_0 dy_0 \quad (5.2)$$

Given the field at a specified plane ($z = 0$), we wish to calculate the field at another plane z, where the object is located. The Fourier transform of the first three terms from Equation (5.1) are eliminated by applying a filter in the Fourier space of the object field, Equation (5.2). The angular spectrum can then be propagated in space along the z – axis, perpendicular to the hologram plane, multiplying the Equation (5.2) by $\exp[ik_z z]$. The reconstructed complex wave-field $E_{\lambda i}(x, y, z)$ is found by:

$$E_{\lambda i}(x, y, z) = (\frac{1}{2\pi})^2 (x, y, z) \iint dk_x dk_y A_0(k_x, k_y; 0) \exp[i(k_x x + k_y y + \sqrt{k^2 - k_x^2 - k_y^2} z)]$$

$$= \mathscr{F}^{-1}\{\mathscr{F}\{E_0\} \cdot \mathscr{F}\{h\}\} = \mathscr{F}^{-1}\{A_0 \cdot H\} \quad (5.3)$$

where, $H(k_x, k_y) = \frac{1}{2\pi} \exp[i(\sqrt{k^2 - k_x^2 - k_y^2} z)]$ is the Fourier transform of the Huygens PSF for $k_z \cong k$. The holographic process is repeated using N different wavelengths, generating the holograms $H(x_h, y_h, \lambda_1)$, ... $H(x_h, y_h, \lambda_i)$. From each of the holograms, the

optical field $E(x,y,z,\lambda_i)$ is reconstructed as a complex 3D array over the volume in the vicinity of the object. This process is illustrated using the superposition principle,

$$E(r) = \sum_{i=1}^{N} E_{\lambda i}(r) \sim \sum_{i=1}^{N} \iiint O(r_P) \exp(ik_i \,|\, r - r_P \,|) d^3 r_P =$$

$$\iiint O(r_P) \sum_{i=1}^{N} \exp(ik_i \,|\, r - r_P \,|) d^3 r_P \sim \iiint O(r_P) \cdot \delta(r - r_P) d^3 r_P \sim O(r) \qquad (5.4)$$

When N goes to infinity, the sum under the volume integral from Equation (5.4) becomes a delta function. In this way, the conjugate of the digitized scattered wave is reconstructed at various z positions and it is proportional to the real object image wave at r, $O(r)$. The addition of the 3D optical fields behaves as a periodic sequence of pulse-like peaks with an optical period or optical beat wavelength (or optical axial extent), $\Lambda_{OPD} = \dfrac{2\pi}{\delta k}$ with optical axial resolution $\delta z_{OPD} = \dfrac{\Lambda}{N}$, wavenumber range $\Delta k = k_{max} - k_{min}$, and wavenumber increment $\delta k = \dfrac{\Delta k}{N-1}$. In the Michelson interferometer the physical difference in length between the two arms, Δz, depends on the optical path difference (OPD) between the object wave and the reference wave, the optical frequency dependent index of refraction $n(\lambda)$, and the dependence on the double pass in reflection mode:

$$\Delta z = \frac{1}{2} \frac{OPD}{n(\lambda)} \qquad (5.5)$$

Assuming an index of refraction of 1.38 in the macular retina the physical difference in length becomes, $\Delta z = 0.36(OPD)$. Therefore, the physical beat wavelength becomes, $\Lambda = 0.36(\Lambda_{OPD})$, and the physical axial resolution becomes, $\delta z = 0.36(\delta z_{OPD})$. Knowing the axial resolution δz and the number of pixels N_z along

the axial scan, z axis, one can obtain quantitative information of the height profile of the object.

5.4 Ophthalmic DIH Scanning System

The DIH instrument uses a high-speed, high-resolution, non-contact, non-invasive technology and has no mechanical moving parts. It consists of an off-axis Michelson interferometer in a backscattering geometry shown in Figure 5.3. The light source is generated by a Millenia V solid-state laser pumping a ring dye laser (Coherent 699), centered on $\lambda = 575nm$ with an output power of up to 500 mW. The laser beam, after being spatially-filtered, collimated (BE) and linearly polarized (P2), is divided by the polarizing beam splitter (PBS) into two beams, sample (OBJ) and reference (REF) waves. Using the lens L1, the laser beam is focused on the back focus of the lens L2, so that the object is illuminated with a collimated light. The objective L3 is placed in the reference arm to compensate for phase curvature induced by L2 into the object arm. The lens L2 projects the hologram plane H (an optical conjugate of the reference mirror plane) onto the CCD camera, through C-mount lenses L4, which form the image at the infinity. The digital camera (monochrome CCD, 30 frames per second, 780 x 640 pixels, with square pixels of 9 μm) acquires an image of the hologram at H, a superposition between a plane reference wave and the object wave that has diffracted over a distance $z = Z$ from the object plane. We call Z the reconstruction distance due to the fact the object can be numerically brought in focus by adjusting the distance Z, without moving the object or the CCD camera. Polarizers P1, P2, analyzer P3 and quarter-wave plates QW are used in conjunction with the polarizing beam splitter PBS to continuously adjust the overall laser

power in the experimental setup and inside of the interferometer. The analyzer P3 is cross polarized with regard to the polarizer P2 and the quarter wave plates are oriented at 45°. The reflected light at the object and at the reference pass the quarter wave plates two times changing the polarization plane by 90°, and interfering at the CCD plane after passing the analyzer P3. The role of the polarizer P3 is to pass the light reflected from the sample and to block the stray light from the optics [27]. A variable aperture placed at the back focal (Fourier) plane of the objective lens L2 can be useful in controlling the angular spectrum of the object field.
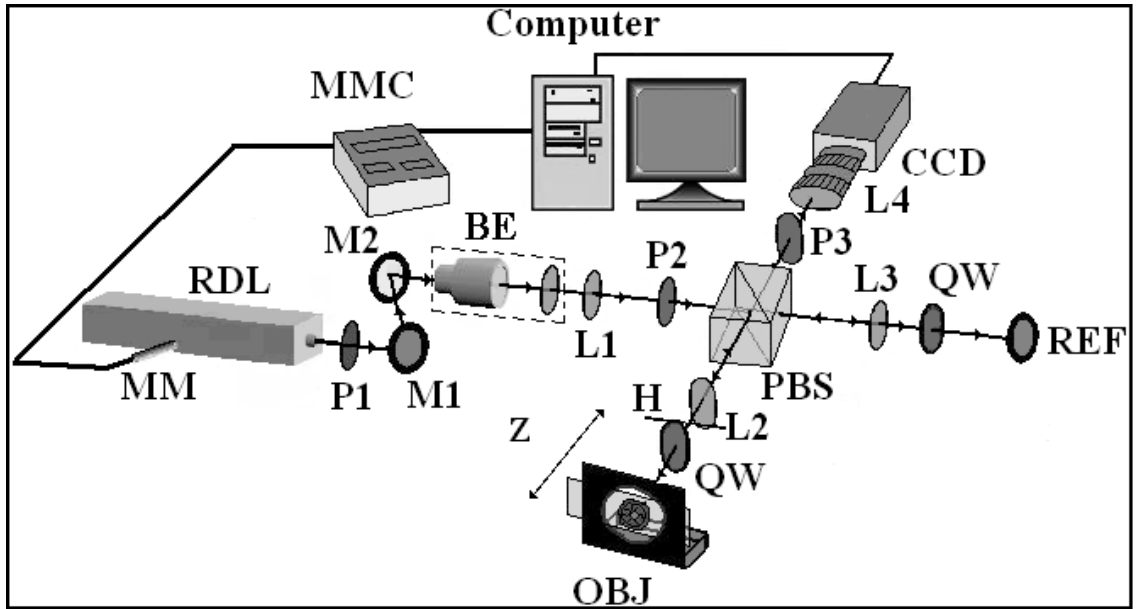
Figure 5.3. Experimental Apparatus. RDL: ring dye laser; M1 and M2: mirrors; REF: reference mirror; L1, L2, L3, L4 and L5 lenses; BE: beam expander; P1, P2 and P3: polarizers; PBS: polarizing beamsplitter; QW's: quarter waveplates; A: aperture; H: hologram plane; OBJ: object; MM: motorized micrometer; MMC: controller for MM.

5.5. Results

The attached amplitude images were obtained from a healthy excised human eye supplied to us by the Lions Eye Institute for Transplant & Research of Tampa FL. The holographic image acquisition and computation of the optical field of the macula sample are carried out for about 50 wavelengths in the $\Delta\lambda$ range of 560-600 nm. Superposition of images, in the DIH processes described above, reveals the topographic mapping within the macular tissue, Figure 5.4a, and clearly delineates borders of blood vessel segments. The imaged surface area is 5020 x 5020 μm^2 with a physical axial range $\Lambda = 209.75 \mu m$ and physical

axial resolution $\delta z = 4.19 \mu m$. Different layers are distinguishable in the cross-sectional images of the human macula, Figure 5.4b, 5.4c. The optical thickness between the retinal nerve fiber layer (NFL) and the retinal pigment epithelial layer (RPE) is about $84 \mu m$.

a)   b)   c)
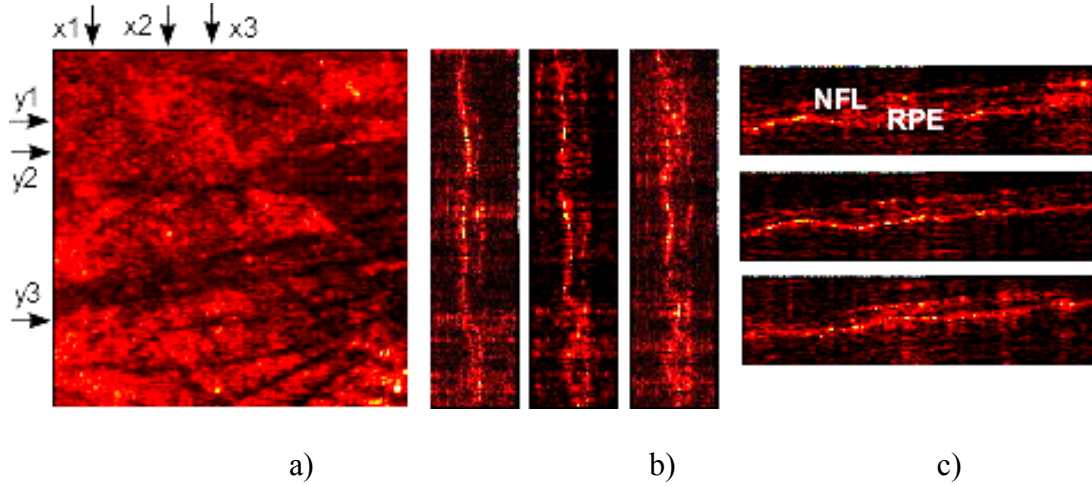
Figure 5.4. The Reconstructed Volume of the Human Macula Sample: (a) x-y cross-section, FOV = 5020 x 5020 μm^2; (b) y-z cross sections at various x values, 5020 x 209.75 μm^2, from left to right, x1, x2, and x3; (c) x-z cross sections at various y values, 209.75 x 5020 μm^2, from top to bottom, y1, y2, and y3; $\Delta\lambda$: 0.560-0.600 μm; $\delta z = 4.19 \mu m$; $\delta x = \delta y = 19.6 \mu m$; NX= NY=256 pixels; NZ= 50 pixels.

Figure 5.5a, represents the en-face reconstructed 3D structure of the optic nerve region with an area of 5020 x 5020 μm^2. We can identify the scleral ring (disc) diameter Ddisc = 1750 μm and the cup diameter Dcup = 660 μm, Figure 5.5b. Our measurements cannot be clinically correlated with normal anatomic values as the tissue was post-mortem and edematous, falsely enlarging the disc diameter with swelling of the surrounding nerve fiber layer tissue. Vitreous papillary adhesions also had to be removed

with forceps from the optic nerve tissue, and any remnants laying atop the nerve tissue rim could have falsely enlarged our measurements. The optic nerve sample was slightly tilted when it was imaged, resulting in the left side of the scleral ring appearing to be darker than the right. The optic cup has a well distinguished shape with high reflectivity - depicted by brighter colors on 3D imaging. The higher reflectivity within the cup depth explains the higher noise in the region of the optic cup, (Figure 5.5a.). The black valley around the disc is a false valley due to a phase jump at the edge of the disc.

a)   b)
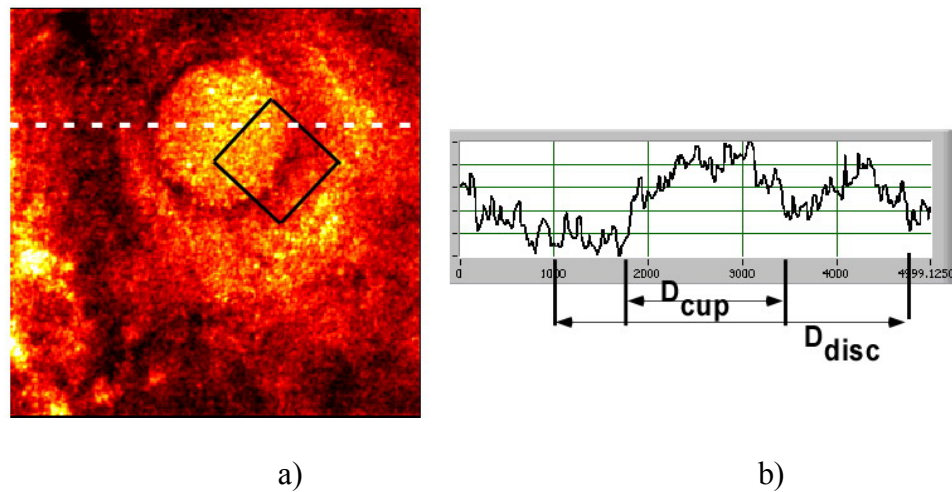
Figure 5.5. The Reconstructed Volume of the Human Optic Nerve Sample: (a) x-y cross-section, FOV = 5020 x 5020 μm^2 ; Z_0 = 446 μm ; $\Delta\lambda$: 0.563-0.605 μm ; $\delta z = 4.06 \mu m$; $\delta x = \delta y = 19.6 \mu m$; NX= NY=256 pixels; NZ= 50 pixels; (b) cross section along the dashed line in Figure 5.5a; Dcup = cup diameter, Ddisc = disc diameter.

Figure 5.6a, represents the en-face reconstructed optical field of the rhombus region from Figure 5.5a. The cross-sectional images in the y-z planes Figure 5.6b, and x-z planes Figure 5.6c, are also shown. In practice, if one uses a finite number of

wavelengths, N with a uniform increment δk of inverse wavelengths, then the object image repeats itself at a beat wavelength $\Lambda = \dfrac{2\pi}{\delta k}$, with axial resolution $\delta z = \Lambda / N$. This occurred in the x-z cross sections, Figure 5.6c top, where the bottom of the cup depth, h2, is found at the top. Therefore, to find the cup depth, h1 is added to h2, where h1 (relative to the baseline height) and h2 are the upper and the bottom part of the cup. By using appropriate values of δk and N, the physical axial size (beat wavelength), Λ, can be matched to the axial range of the object, and δz to the desired level of physical axial resolution. The height of the x-z cross sections, Figure 5.6c top, represents the physical axial size $\Lambda = 280.35 \mu m$ made of 50 pixels (the number of wavelengths being scanned) with a physical axial resolution $\delta z = 5.61 \mu m$. Using this information one can quantify the cup depth being as h= 355.11 μm, and the cup slope, s, of about 47°.

| | a) | b) | c) |
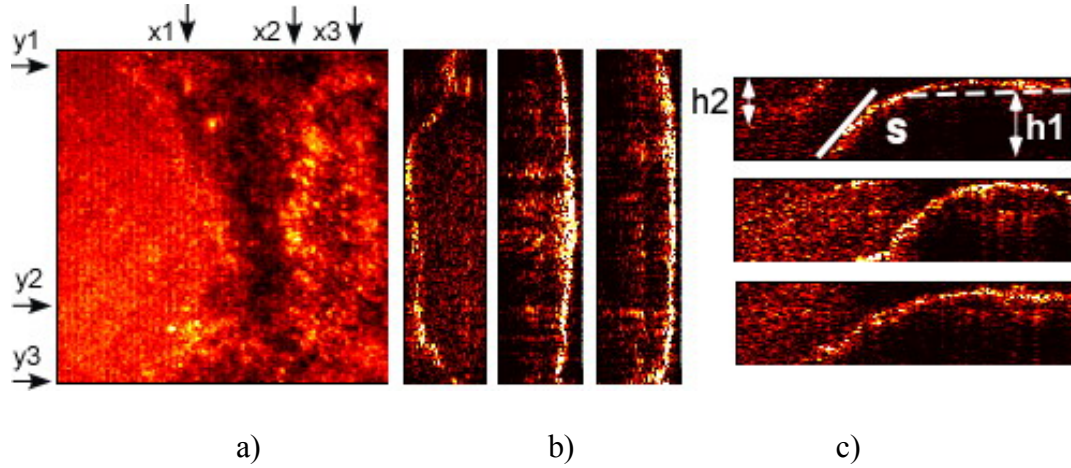
Figure 5.6. The Reconstructed Volume of the Human Optic Nerve Sample (the rhombus shape volume from Figure 5.5a: (a) x-y cross-section, FOV=1100 x 1100 μm^2; (b) y-z cross sections at various x values, 1100 x 280.35 μm^2, from left to right, x1, x2, and x3; (c) x-z cross sections at various y values, 280.35 x 1100 μm^2, from top to bottom, y1, y2, and y3; Z = 29.7 μm; $\Delta\lambda : 0.565 - 0.595 \mu m$; $\delta z = 5.61 \mu m$; $\delta x = \delta y = 4.32 \mu m$; NX= NY=256 pixels; NZ= 50 pixels; s = the slope; h1, h2: heights.

The y-z cross section images of the reconstructed volume of the second eye optic nerve at various x values are shown in Figure 5.7a. The characteristics of the cross-sectional area are: the area imaged is 4696 x 239.85 μm^2, the physical axial extent $\Lambda = 239.85 \mu m$, the reconstruction distance Z = 5049.5 μm; lateral resolution 18.37 μm (256 pixels), and physical axial resolution $\delta z = 4.8 \mu m$ (51 pixels). Cross section (x3) of the intensity levels data along the dotted line is shown in Figure 5.7b, from which the disc diameter and the cup diameter were quantified as: Ddisc = 1750 μm, and the cup

depth is about $240\,\mu m$. The cup-shaped depression is located slightly temporal to its geometric center as shown in all three cross-sections

a)   b)
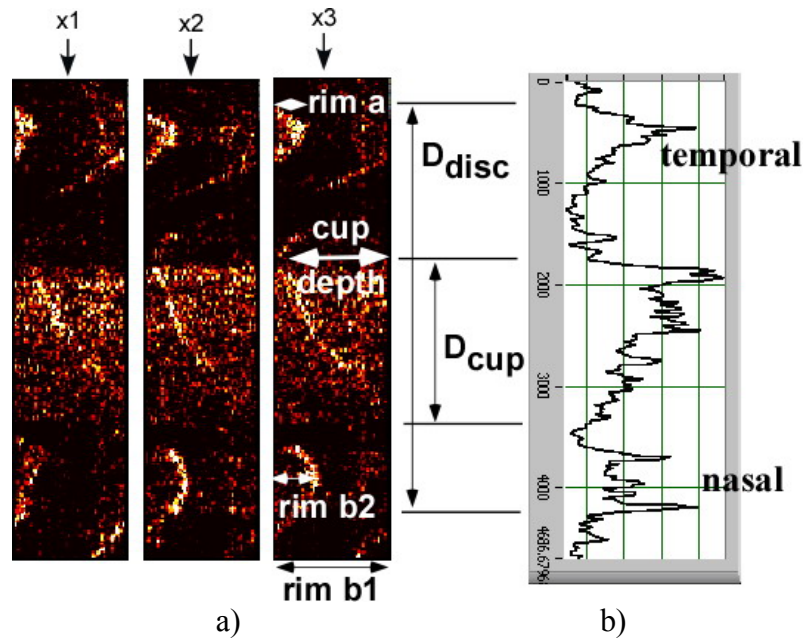
Figure 5.7. (a) Y-Z Cross Section Images of the Reconstructed Volume of the Human Optic Nerve Sample (the second eye optic nerve): at various x values, 4696 x $239.85\,\mu m^2$, from left to right, x1, x2, and x3; (b) intensity levels function of x with temporal, cup, and nasal picks; Z = 5049.5 μm; $\Delta\lambda: 0.562 - 0.597\,\mu m$; $\delta z = 4.8\,\mu m$; $\delta x = \delta y = 18.37\,\mu m$; NX= NY=256 pixels; NZ= 51 pixels; Ddisc: disc diameter; high intensity in the region of the cup does not correspond to physical shape (see discussion in the text).

5.6. Conclusions

Imaging techniques in ophthalmology are currently evolving rapidly. Histological resolution approaching that for in-situ imaging is the goal of many imaging techniques. The ideal imaging device should be a robust instrument that uses high-speed, non-

contact, non-invasive technology, has no mechanical moving parts, and has an axial resolution better than 5 μm. There is no doubt that OCT, with additional extensions, has become one of the most advanced imaging technique in the ophthalmology area. For ophthalmic imaging, the light source has to be chosen as a function of the characteristics of the reflected spectrum. This spectrum varies with three histological parameters, RPE melanin, haemoglobin, and choroidal melanin [31]. The intensity decreases in the green region once the melanin increases and the RPE response becomes weaker. Also, the absorption of the ophthalmic tissue depends on haemoglobin in visible and water in infrared. Water absorption in the vitreous at 950 nm and above 1100 nm limits the scanning wavelength range of about 150 nm [13, 14]. Therefore, light sources operating on a centered wavelength between 800 and 850 nm are necessary to avoid absorption in the ocular media. The wavelength band centered on 830 nm has been employed in clinical OCT instruments. An ultrahigh resolution (UHR) OCT technology using a broadband Ti:Al$_2$O$_3$ laser (centered on 800 nm) at an axial resolution of 2-3 μm has been demonstrated for in-vivo imaging of retinal and corneal morphology [12, 16]. Other recent Fourier domain detection methods utilize high-speed UHR OCT imaging with a bandwidth of ~ 150 nm centered near ~900 nm [11, 14]. Spectral / Fourier domain detection (SD-OCT) utilizes high speed imaging at 1300 nm with an axial resolution of $10\,\mu m$ [41], and at 1060 nm with an axial resolution of $10.4\,\mu m$ [15]. Swept source / Fourier (SS-OCT) domain detection for 3D volumetric imaging of the retina [13], utilizes a bandwidth centered at 850 nm with an axial resolution of $< 7\,\mu m$. Optical imaging of tissue at a longer wavelength (1300 nm) offers deeper choroidal penetration, in spite of

the fact that tissue exposure is higher for wavelengths above 1000 nm. Also, the retinal tissue is more transparent for wavelengths in near-infrared (above 1000 nm).

Despite these advances in the OCT optical biopsy, there is still room to make for improvement of OCT techniques. The results of the Advanced Imaging for Glaucoma Study (AIGS) indicate the SD-OCT is still in infancy [29]. A dilemma, as to why SD-OCT has been unsuccessful compared to time-domain OCT (TD-OCT) in detecting glaucoma by imaging the circumpapilary retinal fiber layer (cpRNFL), constitutes a problem in the retina imaging technology [29]. All OCT devices are characterized by complicated software for image processing and registration of cross-sectional OCT images with a fundus image from the same OCT data set.

Digital Interference holography (DIH) offers rapid 3D imaging with theoretically higher resolution than OCT, and without the need to reassemble images from scans. Our research has demonstrated that, in vitro, DIH can measure the dimensions of the scleral ring and provide a definitive answer regarding the size of the optic disc, a clinically important parameter that is not provided by current OCT instruments. Numerical focusing of holographic images can be accomplished from a single exposed hologram.

This work is to our knowledge a novel and innovative approach to retinal imaging. The goal in the future is to improve DIH imaging parameters to a level compatible with clinical applications and to identify and address technical challenges for such applications.

At this point, our scanner has to overcome the signal-to-noise ratio issue, to provide clinically relevant information. The scanning time is 30 s and the signal-to-noise ratio (SNR) is about 50 dB [23]. The imaging dynamic range or SNR will be improved to

about 90 dB by replacing the dye laser with a Ti:Sapphire laser (longer wavelengths), introducing a high-speed camera and increasing the number of holograms from 50 to 500. With increased speed, and resolution, DIH has the potential to provide a significant improvement in terms of information captured, both for the diagnosis of disease and for the understanding of normal histopathology and physiology. With better axial resolution and greater axial range, we expect to be able to extract more information about retinal thickness and structure.

In vivo imaging of human eye needs to be fast enough to avoid blurring due to eye movement (tremors, drifts, saccades). More attention needs to be paid to scanning of wavelengths at high speed. Normally, the dye laser wavelength is tuned by rotating a birefringent filter (BRF) with a micrometer. The micrometer moves at a speed of ~0.5mm/s, and information on the laser spectral and power behavior at high speed scan is not readily available. A Ti:Sapphire laser with an appropriate actuator and a sweep function parameterized by time is a good option that works very well with the SS – OCT systems. Also, a retinal tracker system for three-dimensional retinal morphology and function will be developed and integrated in the DIH setup.

We plane to translate and adapt the optical bench apparatus onto a fundus camera. Optically, the apparatus will consist of a Michelson interferometer with fundus camera attached to the object arm as an optimized imaging lens for the object, i.e. the eye. Use of optical fibers and couplers allow flexible and compact design of the holography module. With the holography imaging module in place, a set of basic digital holography imaging experiments are to be carried out in order to establish and optimize the imaging characteristics of the fundus camera used as a holography camera. The reference mirror

will have a motorized z-translation stage, for proper matching of relative distance to the object (retina), and the optics will be modified to compensate for the eye's optics in the object arm.

Another challenge in ophthalmic imaging applications is to ensure that the level of laser radiation on the eye is not damaging to the vision. The SNR of the system needs to be sufficient so that a radiation level weak enough to safe can still generate good quality images. Once new equipment is integrated in the setup, we will carry out a set of measurements to calibrate the irradiance arriving at the object. The image quality, i.e. SNR, is to be measured as a function of the irradiance, as well as various other optical parameters, such as polarization, object-reference intensity ratio, and the type of object being imaged.

Admittedly, limitations inherent to post-mortem cadaveric models did exist in regard to our ability to correlate measurements from imaging with known normal anatomic findings. However, the images do illustrate the ability of DIH imaging to successfully depict and measure contour of ocular tissue. Our goal in imaging was not to replicate known measurements, but rather to illustrate the concept of the ability of DIH imaging to image a 3D ocular structure with adequate resolution.

With full development of its capabilities, DIH may provide another option in ocular imaging, providing high resolution 3D information which could potentially aid in guiding the diagnosis and treatment of many ocular diseases.

5.7. Bibliography

[1]. J.C.H. Tan and R.A. Hitchings, *Invest. Ophthalmol.Vis. Sci.* **44** 1132 (2003).

[2]. K.H. Min, G.J. Seong, Y.J. Hong, *et al*. *Kor. J. Ophthalmol*. **19** 189 (2005).

[3]. J. Xu, H. Ishikawa, G. Wollstein, *et al*. *Invest. Ophthalmol.Vis. Sci.* **49** 2512 (2008).

[4]. O. Geyer, A. Michaeli-Cohen, D.M. Silver, *et al*. *Br. J. Ophthalmol*. **82** 14 (1998).

[5. F.S. Mikelberg, *Can. J. Ophthalmol.* **42** 421 (2007).

[6]. J.B. Jonas, G.C. Gusek, and G.O.H. Naumann, *Invest. Ophthalmol.Vis. Sci.* **29** 1151 (1998).

[7]. N.V. Swindale, G. Stjepanovic, A. Chin, et al. *Invest. Ophthalmol.Vis. Sci.* **41** 1730 (2000).

[8]. C. Bowd, L.M. Zangwill, E.Z. Blumenthal, et al. *J. Opt. Soc. Am. A*. **19** 197 (2002).

[9]. C.K. Leung, W.M. Chan, W.H. Yung, *et al. Ophthalmology*. **112** 391 (2005).

[10]. G. Wollstein, H. Ishikawa, J. Wang, *et al. Am J Ophthalmol*. **139** 39 (2005).

[11]. M. Wojtkowski, V. Srinivasan, J.G. Fujimoto, *et al. Ophthalmology*. **112** 1734 (2005).

[12]. W. Drexler, U. Morgner, R.K. Ghanta, J.S. Schuman, F.X. Kärtner, J.G. Fujimoto. *Nat Med.* **7** 502 (2001).

[13]. V.J. Srinivasan, I. Gorczynska, and G.J. Fujimoto. *Opt. Lett.* **32** 361 (2007).

[14]. V.J. Srinivasan, T.H. Ko, M. Wojtkowski, *et a*l. *Invest. Ophthalmol.Vis. Sci.* **47** 5522 (2006).

[15]. Y. Yasuno, Y. Hong, S. Makita, et al. *Opt. Express*. **15** 6121 (2007).

[16]. G. Wollstein, L.A. Paunescu, T.H. Ko. *Ophthalmology*.**112** 229 (2005).

[17]. M.K. Kim. *Opt. Lett.* **24** 1693 (1999).

[18]. M.K. Kim. *Opt. Express*. **7** 305 (2000).

[19]. A. Dakoff, J Gass and M.K. Kim. *J. Electr. Imag.***12** 643 (2003).

[20]. L. Yu and M.K. Kim. *Opt. Express*. **13** 5621 (2005).

[21]. L. Yu and M.K. Kim. *Opt. Lett*. **30** 2092 (2005).

[22]. M.K. Kim, L. Yu and C. J. Mann. *J. Opt. A: Pure Appl. Opt.*. **8** 512 (2006).

[23]. M. C. Potcoava and M.K. Kim. *Meas. Sci. Technol***. 19** 074010 (2008).

[24]. M.C. Potcoava, C.N Kay, M.K Kim, and D.W Richards, *Ophthalmic Technologies XIX*, 7163-10, SPIE BIOS 2009.

[25]. F. Montfort, T. Colomb, F. Charrière, et al. *Appl. Opt.* **45**, 8209-8217 (2006).

[26]. C.K. Leung, W. Chan, Y. Hui, *et al. Invest. Ophthalmol.Vis. Sci*. **46** 891 (2005).

[27]. H. Piller, *Zeiss-Werkschrift*. **34** 87 (1959).

[28]. A. Chan, J.S. Duker, T.H. Ko, *et al*. *Arch Ophthalmol.* **124** 193 (2006).

[29]. S.J. Preece and E. Claridge, *Phys.Med. Biol*. **47** 2863 (2002).

[30]. R. Huber, K. Taira, M. Wojtkowski, and J.G. Fujimoto. Proc. SPIE; 6079, 60790U (2006).

[31]. J. G. Fujimoto. Nature Biothechnology. 21 1361(2003).

[32]. American Academy of Ophthalmology Basic and Clinical Science Course: Fundamentals and Principles of Ophthalmology, 2006).

[33]. J.W. Goodman, *Introduction to Fourier Optics* (3rd Edition, Roberts & Company Publishers, 2005).

CHAPTER 6

FINGERPRINT BIOMETRY APPLICATIONS OF DIGITAL INTERFERENCE HOLOGRAPHY

The Digital interference holography (DIH) is a multiwavelength optical technique that can be used to build holographically the three dimensional structure of the fingerprints. This chapter proposes to show how the DIH technique could be used in the field of forensic science as a powerful fingerprints scanner to identify and quantify Level 1 (pattern), Level 2 (minutia points), and Level 3 (pores and ridge contours) fingerprint characteristics from the amplitude images. Section 6.1 reviews some of the fingerprint features used in the enrollment, verification, and identification phases. Section 6.2 covers the theory of the fingerprint imaging and object field reconstruction. Section 6.3 discusses the experimental setup for fingerprint imaging. Samples characteristics are discussed in Section 6.4. Section 6.5 presents experimental results. Conclusions are presented in Section 6.6.

6.1. Introduction

There are three kinds of fingerprints that could be identified where they were left behind. They are latent, visible, and plastic prints. Latent prints are left on the surface of the objects and are invisible. A chemical is used to make the prints visible. Visible prints are

left when a finger is coated with a colored substance. Plastic prints are formed when the finger presses onto a soft surface such as wax, soap or putty. All these prints are called exemplar fingerprints when they are obtained from human fingers using scientific tests under supervision. The features of the fingerprints can be classified in three levels [1-7]. Level 1 feature refer to the pattern type, such as arch, tented arch, left loop, right loop, double loop, and whorl. Level 2 features are formed when the ridge flow is interrupted by some irregularities, known as minutiae. Examples of minutiae are bifurcation, ending, line-unit, line-fragment, eye, and hook. Level 3 features include other dimensional characteristics like pores, creases, line shape, incipient ridges, scars, and warts. Finger recognition is a complex process that occurs in three phases: enrollment, identification and verification [2]. During the enrollment phase fingerprints from different individuals are recorded digitally by the CCD camera. The identification process or one-to-many matching refers to the finding the person who committed the crime based on the matching of his fingerprints against an existing database of known fingerprints. The verification process or one-to-one matching refers to the comparison of the individual fingerprints against those of his/her enrolled fingerprints template. When enough similarities are found between three or more nearby minutiae in both claimant and enrollee fingerprints, then the fingerprints are said to match. This is called minutia matching. Another matching scheme is the correlation matching [2] performed in the frequency domain due to the fact that the fingerprints in the space-domain are subject to alignment errors such as the elasticity, different noise between claimant and enrollee images, as well as translational and rotational freedoms. Most of the fingerprints technologies rely on minutiae matching approach with higher recognition accuracy. The matching process is a

challenging work; usually it requires a few combined algorithms to improve the accuracy of the measurements. Therefore, there is still much potential for algorithmic improvement [8].

We use the multi-wavelength digital interference holography (DIH) scanner [13-22], and fingerprints recognition to build up the three dimensional structure of the fingerprints and to identify and match fingerprints feature that could be used in the two phases, identification and verification. The wavelengths range is swept automatically and for specific wavelengths the hologram is recorded digitally followed by numerical reconstruction of the optical field. The axial resolution is a parameter that depends on the wavelength scanning range and is obtained by superposing all optical fields. The DIH scanner setup is a Michelson interferometer in off-axis reflection geometry. This work proposes to show how the DIH technique could be used in the field of forensic science to identify and quantify Level 1 (pattern), Level 2 (minutia points), and Level 3 (pores and ridge contours) fingerprint features. Our contribution is as follows: a new optical scanner, DIH, is introduced in the area of the fingerprints recognition; a database of fingerprints is created for each enrolled subject using different print materials; the fingerprint 3D images along with minutiae extracting and minutiae matching are presented; using this technique we were able to obtain information not only about the ridges, but also the depth and the width of the ridges; we built a three dimensional structure of the fingerprints templates with microns size axial resolution.

6.2. Theory

The diffraction is described by two mathematical methods. In the transfer function method, the object field at the observation plane is the inverse Fourier transform of the

96

Fourier transform of the object field at the aperture multiplied by the free-space transfer function. The second method is based on calculating the spatial distribution of the object field at the observation plane as an integral over individual responses of each point of the aperture through the point-spread function of the system. Function of the type of wavelet arriving at the observation plane, the point-spread function can take various mathematical expressions. The below developed theory is based on the Fourier approach.

Suppose an object is illuminated by a laser beam of wavelength λ. Considering the actual wave-front amplitude $O(r_{OBJ})$, the point r_{OBJ} on the object scatters the light into a Huygens wavelet, $O(r_{OBJ})\exp(ik|r-r_{OBJ}|)$ where the object function $O(r_{OBJ})$ is proportional to the amplitude and phase of the wavelet scattered or emitted by object points. For an extended object, the field at r, is found by linearly superposing the the reconstructed optical fields due to the secondary wavelets inside of the object and it has the expression,

$$U(r) \sim \int O(r_{OBJ})\exp(ik\,|\,r-r_{OBJ}\,|)d^3 r_{OBJ} \qquad (6.1)$$

where the integral is over the object volume. In holography, the amplitude and the phase of the object field is recorded at the hologram plane, $(x_h, y_h, z_h = 0)$ as $HN(\,H_N(x_N, y_N, \lambda_N)\,)$, for each N$^{\text{th}}$ wavelength. The total optical field as a result of the superposition of all N 3D-arrays results in:

$$U(x,y,z;\lambda) \sim \sum_k \int O(r_{OBJ})\exp(ik\,|\,r-r_{OBJ}\,|)d^3 r_{OBJ} \sim$$
$$\int O(r_{OBJ})\delta(r-r_{OBJ})d^3 r_{OBJ} \sim O(r) \qquad (6.2)$$

If a large number of wavelengths is used with uniform increment $\Delta(1/\lambda)$, the object image repeats itself at the beat wavelength (axial size), $\Lambda = \left[\Delta(1/\lambda) \right]^{-1}$, having an axial resolution of $\delta z = \Lambda / N$.

We perform the reconstruction of the optical field using the angular spectrum algorithm. The advantages of the angular spectrum method over more commonly used Fresnel transformation (or Huygens convolution) method, are as follow: Firstly, the Fresnel transformation is accurate only when small angles of diffraction are involved [22]. The angular spectrum method and the Fresnel approximation are equivalent within the small angles approximation called paraxial approximation. Secondly, the noise and frequency components in the Fourier space can be easily controlled by eliminating unwanted frequencies. Thirdly, no minimum reconstruction distance is necessary as in the case of the Fresnel approximation [17]. Once the angular spectrum at z = 0 is calculated by a Fourier transform, the field at any other z-plane can be calculated with just one more Fourier transform.

6.3. Digital Interference Holography Fingerprint Scanner Setup

A schematic diagram of the DIH scanner setup is presented in Figure 6.1. We used a Michelson interferometer in a backscattering geometry with a ring dye laser source, tunable over a range of 563 nm to 615 nm with an output power of up to 500 mW. The object (fingerprint sample) is illuminated by a collimated beam as follow: The laser output, after being spatial-filtered, collimated and linearly polarized, is split into sample and reference waves at polarized beam splitter, PBS. The focusing lens, L2, focuses the laser on the back focus of the objective lens L3, and L5 (C-mount lenses) forms the

image at infinity. The reference mirror is at the optical conjugate of the plane H through the matching objective lens L4. A digital CCD camera (8 bit, 30 frames per second, 780 x 640 pixels with 9 μm pitch) acquires the holographic interference between the plane reference wave and the object wave that has propagated (diffracted) over a distance z from the object plane. We call z the reconstruction distance due to the fact the object can be numerically brought into focus by adjusting the distance, z, without moving the object or the CCD camera. The fingerprint on a glass surface induces differences in the optical polarization or reflection, or both, between the clean part of the surface and that bearing the print [10]. The polarization optics – polarizers P1, P2, analyzer P3, quarter wave plates, and polarizing beam splitter – are used to continuously adjust the overall laser power in the experimental setup and inside the interferometer. A variable aperture placed at the back focal (Fourier) plane of the objective lens, L3, can be useful in controlling the angular spectrum of the object field. Samples are attached to a microscope slide and mounted on a lens holder.
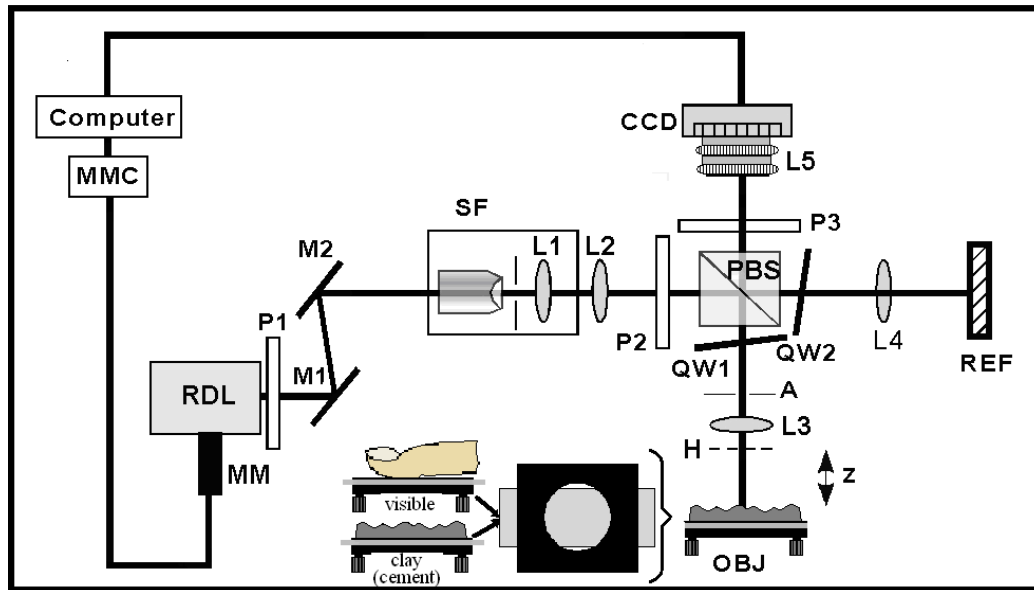
Figure 6.1. Digital Interference Holography Fingerprint Scanner Setup. RDL: ring dye laser; M's: mirrors; SF: spatial filter and expander; L1, L2: lenses with focal length of 25 cm; L3, L4: lenses with focal length of 15 cm; L5: C-mount lens set to infinity focus;; PBS: polarizing beamsplitter; QW's: quarter waveplates; A: aperture; H: hologram plane; OBJ: object (visible, clay, cement); REF: reference mirror; MM: motorized micrometer; MMC: controller for MM.

6.4. Sample Characteristics

For the purpose of evaluating our DIH system, in the enrolment phase, we created two sets of image databases, DB1 with field-of-view (FOV) 5.0 x 5.0 mm^2 and DB2 with FOV 10.4 x 10.4 mm^2. Each database contains image data from a) visible fingerprint, b) the clay fingerprint, c) the plastic print on a mixture of clay and silver enamel, d) the plastic print on clay (the thumb finger was coated with a lightly layer of enamel before pressing into the clay), e) the plastic clay print only; and f) the plastic cement print of

thumb fingerprint from three subjects A, B, and C, with 5 impressions for each subject: visible fingerprints on glass by using silver enamel Figure 6.2a (subject A), and Figure 6.2b (subject B); the plastic print on a mixture of clay and silver enamel Figure 6.2c, the plastic print on clay (the thumb finger was coated with a light layer of enamel before pressing into the clay), Figure 6.2d; the plastic clay print only Figure 6.2e; and the plastic cement print Figure 6.2f. We tested different kinds of household materials. One set of prints was made with Crayola Solid White Model Magic FUSION mixed with TESTORS Gloss Enamel Craft Paint, 1180 Steel Acier Figure 6.2c, to make the imprints more reflective. The two materials become sticky if too much enamel is added resulting not good fingerprint impressions. The other set of prints was made with Van Aken Claytoon Modeling Clay only. Usually the plastic fingerprints are lifted using different impression materials. To obtain the positive fingerprints (real), a few drops of Duco (ITW Devcon Corporation) household cement were poured at the top of the negative (reverse of real print) clay print [11, 12]. This kind of cement dries hard and clear, making the fingerprint features look natural. After a few hours, the clay was removed from below the cement print surface, and extra work has been done to clean the fingerprints positive mold of the impurity. Air bubbles are inevitable since the clay does entrap air inside of it, Figure 6.2f. In order to affix the fingerprints samples in the optical setup a small scanning screen made with a microscope slide attached to a lens holder, Figure 6.1. All clay print samples in different combinations and the cement sample were fixed on microscope slides facing the CCD camera.
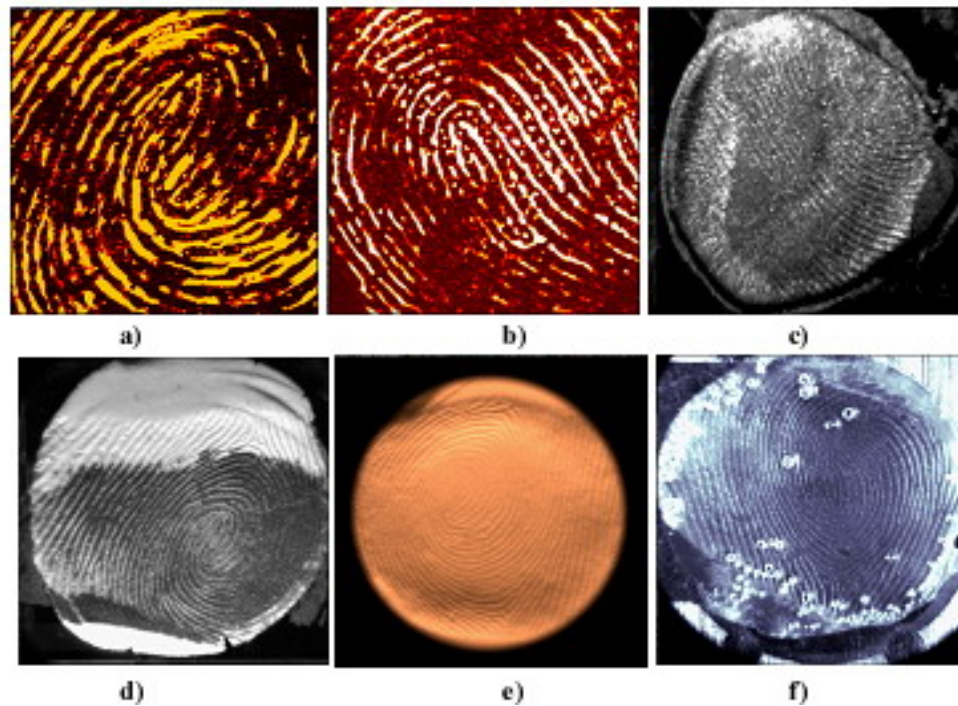
Figure 6.2. Fingerprints Samples: the enamel visible fingerprints, a) subject A; b) subject B; the clay fingerprints, c) the plastic print on a mixture of clay and silver enamel, d) the plastic print on clay (the thumb finger was coated with a lightly layer of enamel before pressing into the clay), e) the plastic clay print only; and f) the plastic cement print.

6.5. Results

When a finger tip coated with enamel touches the microscope cover slip, a visible pattern of ridges and valley is left behind, Figure 6.3a, 6.3d. From the experimental setup, one can notice the collimated laser beam illuminates the microscope cover glass at a right angle, and the CCD camera plane is parallel to the object plane, therefore the light reflected from the glass only (valleys) is bright since the specular reflection happens at a

right angle. The light reflected from the enamel prints (ridges) represents a combination of specular and diffuse light, so the ridges prints appear darker. We can notice a doubled-loop fingerprints pattern for subject A, with a few examples of bifurcation points A1's and ending points A2's in both direct image Figure 6.3a, and reconstructed image using DIH, Figure 6.3b. The quality of the reconstruction of the visible fingerprints using DIH is high since the flow of the ridges follows the same pattern on both the direct and reconstructed prints. Moreover, the closed and open pores A3's, located on the ridges are very well distinguishable in both images. Taking into consideration the lateral resolution in the x or y direction is $\delta x = \delta y = 40.56$ µm with the same number of pixels, $N_x = N_y = 256$, the width of the fingerprint ridge to which the arrow A4 is pointing to is $212 \mu m$ for subject A, in Figure 6.3b, and $454 \mu m$ (arrow B4) for subject B in Figure 6.3d. In the identification or verification stages, the examiner also determines the orientation of the imprint left by the fingerprint ridges. Here, using the 3D representation of the reconstructed optical field by the DIH, Figure 6.3c, an examiner could obtain significant information about the orientation of the imprint left by the fingerprint ridges under different views. As a comparison, a direct image of subject B, with a right loop pattern, bifurcation point B1, ending point B2, and pores B3, is shown in the Figure 6.3d. Therefore, based on all this information, DIH can act as an optical lifting tool in the area of visible fingerprint recognition.

<center>a)   b)   c)   d)</center>
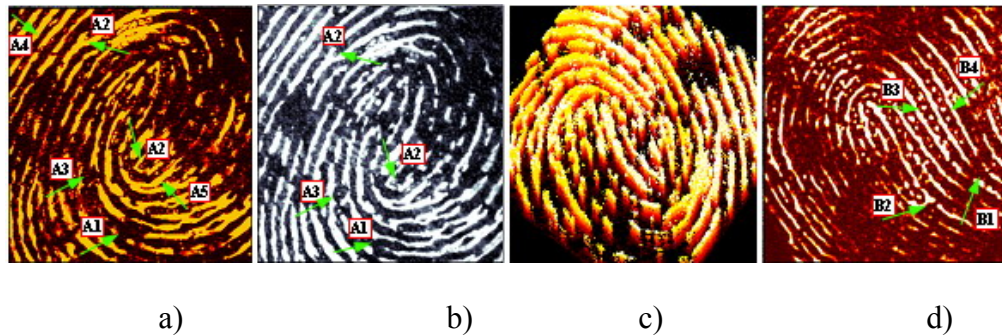
Figure 6.3. Enamel Visible Fingerprints, ridges (dark), valley (bright): a) x-y direct image data, subject A; b) x-y reconstructed optical field, subject A; c) the reconstructed and rotated (Euler angles: θ =4.32°, φ= 234° , Ψ = 0.23°) optical field , subject A; d) direct image data, subject B; FOV =10.383 x 10.383 mm^2 , $\delta x= \delta y$= 40.56 μm; Nx = Ny =256 pixels; A's, B's represent Level 2 and Level 3 fingerprint characteristics.

Fingerprints left at a crime scene do not always present good quality. This is the case of the sample in Figure 6.2c, where the core part of the fingerprint is not shown. This is a fingerprint pattern with high reflectivity, similar to a silver coin. Using DIH, we can reconstruct the 3D fingerprint profile of this sample, the plastic print on a mixture of clay and silver enamel Figure 6.4. The holographic image acquisition and computation of the optical field are carried out for each of 50 wavelengths in the range from 560 nm to 600 nm. Superposition of images, in the DIH process described above, reveals the wavy features of the fingerprints pattern. The imaged surface area is about 5.0 x 5.0 mm^2. The axial range is $\Lambda = 210.5 \mu m$, the lateral resolution $\delta x = \delta y = 19.6 \mu m$, and $\delta z = 4.205 \mu m$. A valley/ridge in a negative clay print corresponds to a ridge/valley in a positive clay print. From the fingerprint topography in Figure 6.4b, 6.4c, one can quantify the height of the fingerprint ridges from valley to top and the width of the fingerprint

<center>104</center>

ridges from valley to valley, as $h = 80.5 \mu m$ (about 19 pixels of size μm), and

$w = 764 \mu m$ respectively (about 39 pixels of size 19.6 μm).
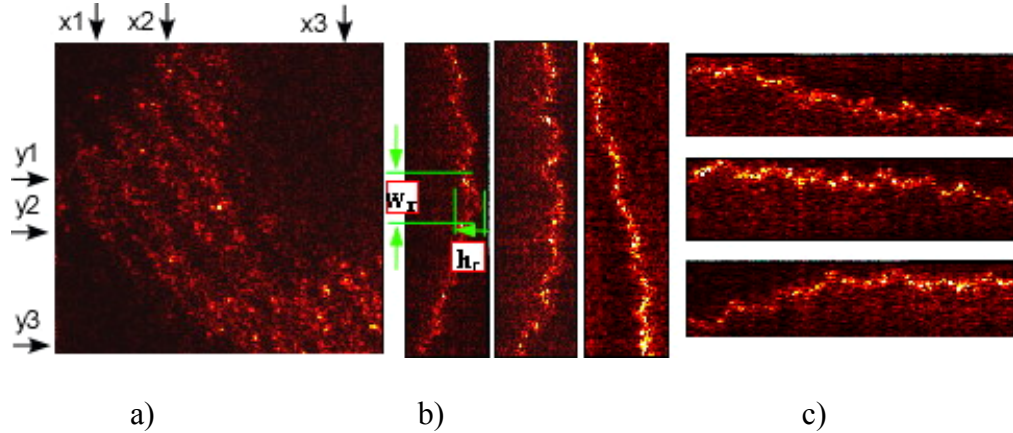
Figure 6.4. The Reconstructed Volume of the Plastic Print on a Mixture of Clay and Silver Enamel Sample: (a) x–y cross-section, 5017×5017 μm^2; (b) y–z cross sections at various x values, 210.5×5017 μm^2, from left to right, x1, x2 and x3; (c) x–z cross sections at various y values, 5017×210.5 μm^2, from top to bottom, y1, y2 and y3; $\Delta\lambda$: 0.560-0.600 μm; Z= 743 μm; Λ= 210.5 μm; $\delta x= \delta y$ =19.6 μm, δz = 4.205μm, Nx = Ny =256 pixels, Nz = 50 pixels.

The next example is a small area sample, FOV~5.0 x 5.0 mm^2, the thumb finger of the subject C was coated with a light layer of liquid enamel and pressed against the clay mold to make the prints. In the en-face image, Figure 6.5a, there is an important Level 2 (minutiae) feature, called crossover, which is a short ridge that runs between two parallel ridges. The end points of this feature are P_1 and P_2. The distance between the two points along the x axis is $767 \mu m$, and $1505 \mu m$ along the y axis respectively. In the tomographic images, Figure 6.5b, 6.5c, the crests of the ridges (the actual valleys of the

fingerprint) are shown. The two end points of the crossover feature are also visible in the tomographic images. The dark gaps between crests correspond to the actual ridges of the fingerprint and they do not reflect the light since the silver enamel is not more present there.
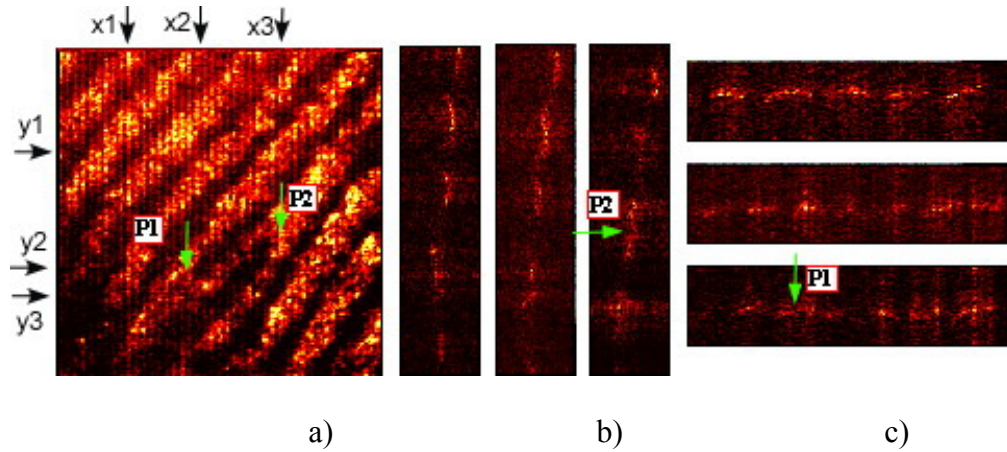
Figure 6.5. The Reconstructed Volume of the Plastic Print on Clay (finger coated with enamel before pressing into the clay) sample (a) x–y cross-section, 5017 × 5017 μm^2; (b) y–z cross sections at various x values, 209.5 × 5017 μm^2, from left to right, x1, x2 and x3; (c) x–z cross sections at various y values, 5017 × 209.5 μm^2, from top to bottom, y1, y2 and y3; $\Delta\lambda$: 0.560-0.600 μm; Z= 743 μm; Λ= 209.5 μm; $\delta x = \delta y =19.6$ μm, $\delta z = 4.19$ μm, Nx = Ny =256 pixels, Nz = 50 pixels; P's represent Level 2 fingerprint characteristics.

The reconstructed optical field with an area of 10.4 x 10.4 mm^2, of the core part of the sample in Figure 6.2d, is shown in Figure 6.6a. This case is similar to the previous sample; the only difference is a double FOV. Because of this, the fingerprint ridges appear closer to each other in this case and the gaps between these are not seen in the

tomographic images, Figure 6.6b, 6.6c. The gaps are visible when the images are magnified. A closer analysis gives reasonable comparison and a point of view as to match a visible print with a 3D print. The valleys pattern and the valleys contour are similar to the doubled-loop fingerprints pattern and the contour of the ridges in the silver enamel visible prints, Figure 6.3a, 6.3b. During the reconstruction process, we observe the features are preserved in spite of the noise present in any optical setup and from various sample conditions. In the fingerprint verification or identification phases, fingerprints are rejected if they do not have the same flow of ridges, direction and location in the two situations. After all these basic similarities are resolved, we need to see where the valley and ridge widths match. The valley A5, with a width of $404 \mu m$ in Figure 6.3a is approximately equal to the width of the ridge A5 in Figure 6.6a, which is $448 \mu m$. The second one is wider since the width of the ridge of a plastic print is measured from valley to valley and not from one edge to the other edge as in the case of the silver enamel visible fingerprints. Moreover the height of the ridge R1 in Figure 6.6b is $38.64 \mu m$ and the width of the same ridge is $677 \mu m$.
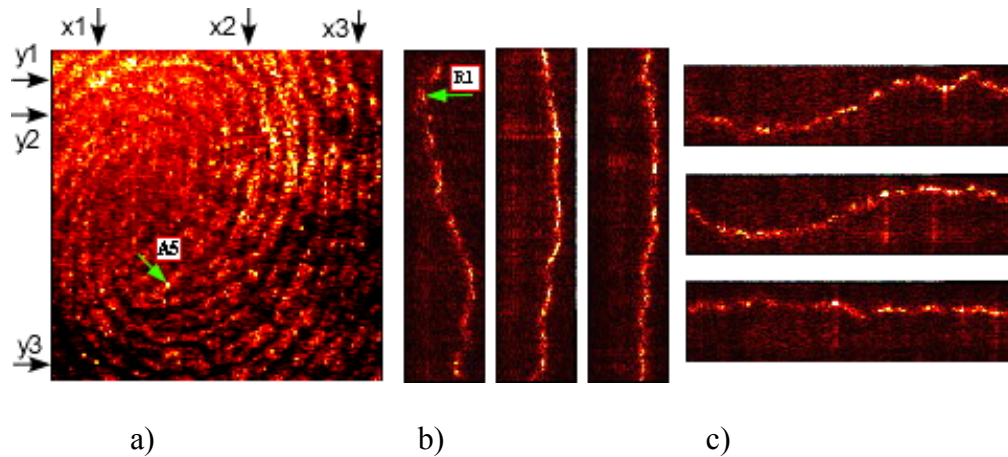
Figure 6.6. The Reconstructed Volume of the Plastic Print on Clay (finger coated with enamel before pressing into the clay) sample: (a) x–y cross-section, 10×10 mm^2; (b) y–z cross sections at various x values, 212.5×10383 μm^2, from left to right, x1, x2 and x3; (c) x–z cross sections at various y values, 10383×212.5 μm^2, from top to bottom, y1, y2 and y3; $\Delta\lambda$: 0.563-0.603 μm; Z= 8911 μm; Λ= 212.5 μm; δx= δy =40.56 mm, δz = 8.497 mm, Nx = Ny =256 pixels, Nz = 50 pixels; A5 and R5 are ridges.

Once the plastic prints are found at the scene of the crime their ridges and furrows must be preserved. A solution to lift prints from a rough surface is to use casting materials that fill in the whole area and not break up fingerprint pattern when the whole print is lifted. A few casting materials, used to record impression marks, are: liquid silicone rubber with catalyst, DuroCast casting putty, TexturLift liquid silicone, and common materials used for dental impressions. Usually, before applying the casting materials the plastic prints should first be dusted with magnetic powder that contains ferromagnetic particles to increase the contrast of the prints. Here, we used Duco household cement, due to the fact that it was cheaper than the other materials, without any magnetic powder applied to enhance the contrast. As an example, Figure 6.7

represents the reconstructed volume of the plastic cement print sample; the en-face image, Figure 6.7a, with an area of 10.4×10.4 µm^2, and the tomographic images, Figure 6.7b, 6.7c with areas of 264×10383 µm^2 (10383×264 µm^2). The axial resolution for this sample is $\delta z = 5.26$ µm and the lateral resolution is $\delta x = \delta y = 40.56$ µm. Sometimes, trying to image the core part of a fingerprint is not simple since the details are very small. The fingerprint surface is clearly distinguishable but the shape of the ridges is barely seen; it means that a better resolution than 5.26 μm is a need to reveal the wavy pattern of prints in the tomographic images or a different casting material should be used.

a)   b)
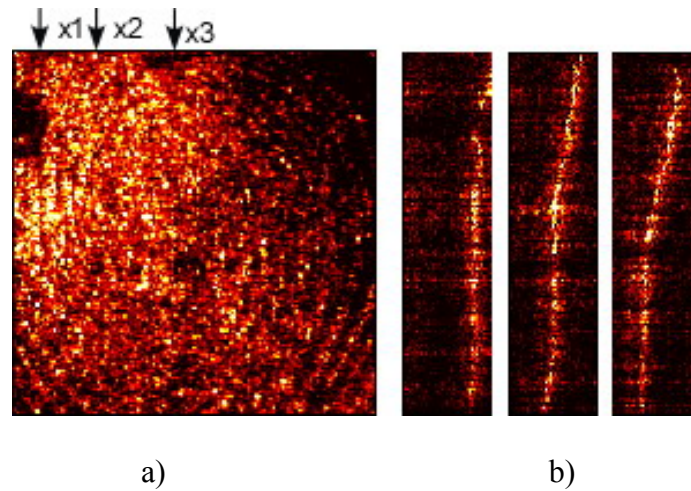
Figure 6.7. The Reconstructed Volume of the Plastic Cement Print Sample: (a) x–y cross-section, 10.383×10.383 mm^2; (b) y–z cross sections at various x values, 264×10383 µm^2; from left to right, x1, x2 and x3; $\Delta\lambda$: 0.561-0.593 µm; Z= 2975 µm; Λ= 264 µm; $\delta x = \delta y = 40.56$ µm, $\delta z = 5.26$ µm, Nx = Ny = 256 pixels, Nz = 50 pixels.

In Figure 6.8a, a direct (non-holographic) image of a patent print is shown, where a finger tip coated with enamel is lightly pressed on a slide glass, leaving a visible, print.

The amplitude image Figure 6.8b clearly reproduces the double loop pattern of this finger. Such two-dimensional image of patent prints can be obtained using conventional imaging methods and holography does not offer particular advantages. Holographic phase images, on the other hand, can provide additional information on the third dimension. Figure 6.8c is a phase image obtained from the same hologram used in Figure 6.8b. Although there is some hint of the loop structure as well as some low frequency variation of the enamel thickness over the field of view, the film is too thick and the phase map is severely wrapped, resulting in overall very noisy pattern. Another hologram is acquired using a slightly different wavelength, 577.71 nm vs. 580.17 nm, and its phase image is shown in Figure 6.8d, which is just as noisy. The two phase images are now combined using the optical phase unwrapping procedure described above, and the result is shown in Figure 6.8e. The beat or synthetic wavelength is then $\Lambda=12136$ μm, which is the full z-scale or color scale of Figure 6.8e. The fact that there is little phase-wrapping in Figure 6.8e implies that the enamel thickness is about 100 μm. These images include bifurcation points (A1), end points (A2), as well as open pores (A3), and the ridge-to-ridge width is measured to be about 212 μm.
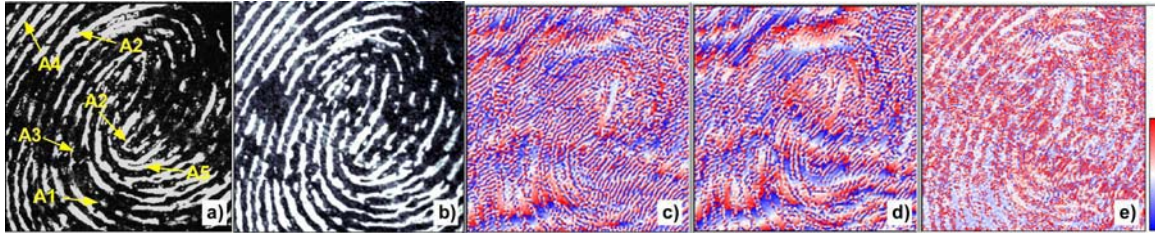
Figure 6.8. Latent Fingerprints. Optical phase unwrapping of fingerprint images by two-wavelength holographic phase microscopy: a) direct image of patent fingerprint made with lightly enamel-coated finger; b) holographic amplitude image; c) and d) phase images from two holograms made with wavelengths 577.71 nm and 580.17 nm; e) optically phase-unwrapped image by combination of c) and d). FOV is and the gray (color) scale of e) corresponds to 136 μm of optical thickness range.

6.6. Conclusions

To summarize, a new non-invasive optical scanner, DIH, was successfully introduced to forensic science, more precisely in the area of fingerprints recognition. The three-dimensional imaging of fingerprints and also their role in identification and verification systems were demonstrated. The selection of the optimum casting materials depends on many variable, including: (1) The material has to be soft enough to not stress the ridges by pressing the finger onto the clay; (2) It has to set up in a short period of time; (3) It does not shrink or expand when it sets up; and (4) The casting materials fill in the entire area and does not break up fingerprint pattern when the whole print is lift. To obtain qualitative fingerprints a few mold (print) and casting materials should be tested to see the effectiveness of the materials. We were able to obtain 2D and 3D enrollee fingerprint structures. Various fingerprint characteristics, Level 1 (pattern), Level 2 (minutia points),

and Level 3 (pores and ridge contours) were identified. Also the height and the width of the ridges were quantified with μm axial resolution ($\sim 5\mu m$). In order to improve this method, we will replace the ring dye laser with a Ti:Saphire laser to increase the tunable wavelength range and subsequently increase the axial resolution below $5\mu m$, and try different casting materials. Advanced commercial fingerprints systems, live-scan sensors, reveal the skin layers using a multiwavelength technique (TIR), [9]. Our future work will concentrate on building up the 3D structure of the live-scan fingerprints using our optical scanner based on the DIH technique. Once the real fingerprints features are stored as digital information in the computer, the real and the casting material fingerprints could be used to map and match identical features. By doing live-scan fingerprints we will also have access to the 3D information of the pores not captured in the print or casting materials.

6. 7. Bibliography

[1]. A. M Knowles, "Aspects of physicochemical methods for the detection of latent fingerprints," *Phys. E: Sci. Instrum.* **11,** 713-721 (1978).

[2]. L. O'Gorman, "Overview of fingerprint verification technologies," Elsevier Information Security Technical Report **3**, (1998).

[3]. A. K. Jain, L. Hong, S. Pankanti, and R. Bolle, "An Identity-Authentication System Using Fingerprints," Proc. of the IEEE **85**, 1365-1388 (1997).

[4]. A. K. Jain, J. Feng, A. Nagar and K. Nandakumar, "On Matching Latent Fingerprints," Workshop on Biometrics, CVPR, (2008).

[5]. U. Park, S. Pankanti and A. K. Jain, "Fingerprint Verification Using SIFT Features," Proc. of SPIE Defense and Security Symposium, (2008).

[6]. Y. Zhu, S.C. Dass and A.K. Jain, "Statistical Models for Assessing the Individuality of Fingerprints", IEEE Transactions on Information Forensics and Security, **2**, 391-401 (2007).

[7]. A. K. Jain, Y. Chen, M. Demirkus, "Pores and Ridges: High-Resolution Fingerprint Matching Using Level 3 Features," IEEE Transactions on Pattern Analysis and Machine Intelligence **29**, 15-27 (2007).

[8]. R. Cappelli, D. Maio, D. Maltoni, J..L. Wayman, and A.K. Jain," Performance evaluation of Fingerprint Verification System," IEEE Transactions on Pattern Analysis and Machine Intelligence **28**, 3-18 (2007).

[9]. R. K. Rowe, S. P. Cocoran, K. A. Nixon, and R. E. Nostrom, "Multispectral Fingerprint Biometrics," Proc. SPIE **5694**, 90 (2005).

[10] S. S. Lin, K. M. Yemelyanov, E. N. Pugh Jr., N. Engheta, "Polarization- and Specular-Reflection-Based, Non-contact Latent Fingerprint Imaging and Lifting," J. Opt. Soc. Am. A **23**, 2137-2153 (2006).

[11]. Y. Cheng and K. V. Larin, "*In Vivo* Two- and Three-Dimensional Imaging of Artificial and Real Fingerprints With Optical Coherence Tomography," Photonics Technology Letters, **19**, 1634-1636 (2007).

[12]. S. Chang, Y. Cheng, K.V. Larin, Y. Mao1, S. Sherif, and C. Flueraru, "Optical coherence tomography used for security and fingerprint-sensing applications," IET Image Process., **2**, 48–58 (2008).

[13]. M. K. Kim, "Wavelength scanning digital interference holography for optical section imaging," Opt. Letters **24,** 1693-1695 (1999).

[14]. M. K. Kim, "Tomographic three-dimensional imaging of a biological specimen using wavelength-scanning digital interference holography," *Opt. Express* **7,** 305-310 (2000).

[15]. L. Yu and M. K. Kim, "Wavelength scanning digital interference holography for variable tomographic scanning," *Opt. Express* **13,** 5621-5627 (2005).

[16]. L. Yu and M. K. Kim, "Wavelength-scanning digital interference holography for tomographic 3D imaging using the angular spectrum method," *Opt. Lett.* **30**, 2092-2094 (2005).

[17]. M. K. Kim , L. Yu and C. J. Mann, " Interference techniques in digital holography," J. Opt. A: Pure Appl. Opt. **8,** 518-523 (2006).

[18]. L. Yu and Z. Chen, "Digital holographic tomography based on spectral interferometry," Opt. Lett. **32**, 3005-3007 (2007).

[19]. M. C. Potcoava and M.K. Kim, "Optical tomography for biomedical applications by digital interference holography," *Meas. Sci. Technol.* **19,** 074010 (2008).

[20]. L.Yu and Z. Chen, "Improved tomographic imaging of wavelength scanning digital holographic microscopy by use of digital spectral shaping," *Opt. Express* **15,** 878-86 (2007).

[21]. F. Montfort, T. Colomb, F. Charrière, J. Kühn, P. Marquet, E. Cuche, S. Herminjard, and C. Depeursinge, "Submicrometer optical tomography by multiple-wavelength digital holographic microscopy," in *Appl. Opt.* **45,** 8209-8217 (2006).

[22]. J. W. Goodman, "Introduction to Fourier Optics," 3rd Edition (2005).

CHAPTER 7

THREE-DIMENSIONAL SPRING CONSTANTS OF AN OPTICAL TRAP

MEASURED BY DIGITAL GABOR HOLOGRAPHY

This chapter presents experimental results on quantitative mapping of three-dimensional optical force acting on an optically trapped co-polyester particle in a three-dimensional parabolic potential by using digital Gabor holography. A brief review of the optical trapping technologies is presented in Section 7.1. The background of the optical trapping process, the digital Gabor holography theory, calibration methods, and the motion tracking algorithm are described in Section 7.2. In Section 7.3 the sample characteristics and the experimental apparatus are presented. The results are presented in Section 7.4. Finally, in Section 7.5 conclusions are made.

7. 1. Introduction

Quantitative studies of physical and biological processes and precise non-contact manipulation of nanometer/micrometer trapped objects can be effectuated with nanometer accuracy due to the development of optical tweezers. A three-dimensional gradient trap is produced at the focus position of a high NA microscope objective. Particles are trapped axially and laterally due to the gradient force. Particles are confined in a potential well and the trap acts as a harmonic spring. The elastic constant or the stiffness along any axis is determined from the particle displacements in time along each

specific axis. Optical tweezers have been used to trap dielectric spheres, living cells, organelles, viruses, and bacteria. The main use for optical trap is the manipulation of biological structures to study of the molecular motors and the physical properties of DNA [1, 2]. Optical sorting tweezers use an optical lattice to sort cells by size and by refractive index [3, 4]. The evanescent field and more recently surface plasmon waves propel microparticles along their propagating path [5, 6]. Optofluidics is a joint technology between microfluidics and micro-photonics. Optical control of the microfluidic elements using optical tweezers was also reported [7]. Another application of optical trapping techniques includes integrated lab-on-a-chip technologies where optical force landscapes are highly desirable to manipulate multiple microparticles in parallel [8].

Several optical trap geometries have been reported [1 - 14]. Cells and colloidal particles have been manipulated in recent years using single or multiple optical beam traps. The first counter – propagating beam optical trap experiment was introduced by Ashkin in 1970 [9]. Optical scattering forces and gradient forces were obtained on submicron silica spheres. The optical fountain is the first optical trapping in three dimensions [10]. It uses gravity against the "scattering" force due to the beam pushing the particle. The single beam gradient trap [11] is considered the most accurate trap in 3D. As with elastic forces, the optical restoring force is proportional to the particle displacement. A stiffness of 0.2 pN/nm was demonstrated for a laser power of 50 mW.

There are two main advantages of using holography in combination with optical tweezers [12-14] instead of quadrant photodetector detectors (QPD). Firstly, in holography the entire 3D structure is reconstructed from a single hologram. It means the 3D position of a particle is also encrypted in a hologram. Recording many holograms in

time we can track the 4D particle position with nanometer precision. The quadrant photodetector detector (QPD) cannot yield the three-dimensional information of the particle position but is favored due to the high recording speed. Video-imaging of the the particle requires high speed CCD camera. Secondly, a laser beam sent into a hologram is divided into a myriad of sub-beams (HOT – holographic optical tweezers), which can independently suspend and manipulate numerous tiny objects for possible transportation, mixing or reacting. Movies of ensembles of microspheres moved into patterns and set to spinning by holographically sculpted light fields were also demonstrated [12, 13].

Another factor that has to be taken in consideration in building optical tweezers is the drift of center of mass of particle. It is difficult to isolate the sample from the environmental and instrumental disturbances to observe the pristine particle motion [22, 25]. The drift frequency is lower than the optically trapped particle motion frequency. Also, this noise is a smooth function of time, independent of the data. The low frequency data components may be excluded by either applying a high pass-filter [24] or by fitting with a smooth curve to be used as a local baseline [25].

Thus, we report the three-dimensional sensing and identification of trapped co-polyester particles of 9.6 μm diameter, trapped in ethylene glycol, using digital Gabor holographic microscopy, with a precision of 1 nm in the z direction and 10 nm along the x and y directions. Holograms were recorded by an IMAQ USB camera at 10 fps for various power values of the trapping laser beam. High resolution complex -valued images of the particles are numerically reconstructed along the optical axis from the holograms using the angular spectrum method [15 – 17]. Three-dimensional position tracking software was developed to compute reconstructions from holograms using CUDA/C and

a graphics processing unit (GPU), the GeForce 8800 GT. Using the object displacements we calculated the stiffness of the optical trap by two calibration methods: equipartition theory, and Boltzmann statistics. The results confirm the linear relationship between the stiffness and the trapping laser power.

We calculated the optical force constants in a three-dimensional parabolic potential model. The results confirm the linear relationship between the stiffness and the trapping laser power. The values of the spring constants of the radiation force, in the axial (z) direction is different from (and weaker than) the transverse (x) and (y). The average values of the spring constants are: the spring constant along x axis $kx = 7.6*10^{-6} N/m$, the spring constant along y axis $ky = 4.8*10^{-6} N/m$, and the spring constant along z axis $kz = 5.0*10^{-7} N/m$.

Software to visualize, record and reconstruct particle positions is written in National Instruments' LabView, Matlab and the NVidia CUDA environment.

7. 2. Theory

7. 2.1. Principle of Digital Gabor Holography

The fundamental setup of a digital holography system is the in-line configuration. The digital in-line, or digital Gabor, holography (DGH) is a 3D imaging technique in which a hologram is formed from interference of the original non-diffracted beam with a component that is diffracted by the object in its path. Information for both virtual and real images is situated in-line along the same axis; therefore, the focused image of either is polluted by its defocused twin. This is one of the drawbacks of using DGH. For the

purpose of tracking particle positions, however, DGH is a particularly simple yet effective solution.

As indicated here by Equation (7.1), the intensity of the interference pattern recorded by the CCD may be decomposed into four terms. The first two appear as zero-order background and are approximately removed by subtracting the average intensity of the entire image from each pixel. The third and forth terms represent the two conjugate real and virtual images.

$$h(x,y) = |O(x,y) + R(x,y)|^2 = |O(x,y)|^2 + |R(x,y)|^2 + O(x,y)R*(x,y) + O*(x,y)R(x,y) \qquad (7.1)$$

The recorded image $h(x,y)$ contains information about both the amplitude and phase of the object beam. This makes it possible to reconstruct the image from the hologram, and we use the angular spectrum method. The Fourier transform of Equation (7.1). is calculated to obtain the spectrum in the object plane, $A_0(k_x,k_y)$. After that, the spectrum is propagated in the frequency domain to any desired distance along the optical axis (z), and is expressed as:

$$A(k_x,k_y,z) = A_0(k_x,k_y)\exp(ik_z z) \qquad (7.2)$$

Taking the inverse Fourier transform, we obtain the reconstructed object wavefront,

$$E(x,y,z) = \mathcal{F}^{-1}\{A(k_x,k_y) \cdot \mathcal{F}[h(x,y;z)]\}. \qquad (7.3)$$

where $h(x,y;z) = -\dfrac{ik}{2\pi z}\exp(ik\sqrt{x^2 + y^2 + z^2})$ is the Huygens PSF. Breaking the reconstructed complex field into its polar components we get

$$E(x,y,z) = |E(x,y,z)|\exp[i\phi(x,y,z)] \qquad (7.4)$$

where $|E(x,y,z)|$, and $\phi(x,y,z)$ represent the reconstructed object wavefront amplitude and phase at r. In this way, we have access to both the amplitude and the phase information. However, in this experiment we use only the amplitude information.

7. 2.2 Principle of Optical Trapping

Since the size of the particles used in this experiment is $d = 9.6\mu m$ and the laser trapping wavelength is $\lambda = 0.532\mu m$, the scattering of light by particles is described by the Mie theory ($d > \lambda$) [18]. Also, the trapping position is determinable by analysis of reflected or refracted light from the particles. The optical trapping forces acting on particles are radiation pressure forces in two forms: scattering (external) and gradient (internal) forces. The scattering force points away from the light source and occurs when photons reflect from the particle. The gradient force is directed toward the focus of the laser beam, as can be seen by conserving momentum when a photon is refracted twice through a sphere. When the gradient force in the region beyond the focus is greater than the scattering force, trapping is stable [11]. The total force acting on the particle has the expression:

$$F_{tot} = F_s + iF_g = \frac{nP}{c}\left\{\{[1+R\cos 2\theta]+iR\sin 2\theta - T^2\sum_{n=0}^{\infty}R^n e^{i(a+nb)}\right\} \tag{7.5}$$

where, F_s, and F_g are the scattering force and the gradient force. The expressions for the two forces are:

$$F_{tot} = F_s + iF_g = \frac{nP}{c}\left\{\{[1+R\cos 2\theta]+iR\sin 2\theta - T^2\sum_{n=0}^{\infty}R^n e^{i(a+nb)}\right\} \tag{7.6}$$

$$F_s = \frac{nP}{c}\left\{1+R\cos 2\theta + -\frac{T^2[\cos(2\theta - 2\theta_r)+R\cos 2\theta]}{1+R^2 +2R\cos 2\theta_r}\right\} \tag{7.7}$$

120

$$F_g = \frac{nP}{c}\left\{1 + R\sin 2\theta + -\frac{T^2[\sin(2\theta - 2\theta_r) + R\sin 2\theta]}{1 + R^2 + 2R\cos 2\theta_r}\right\} \qquad (7.8)$$

In the two equations:, n is the refractive index of the surrounding medium, P is the laser beam power, c is the speed of light, R is the reflectance of light at the surface of the particle, T is the transmittance of light, θ is the angle of incidence, and θ_r is the angle of refraction. The trapping force is: $F = Q(\frac{nP}{c})$, where Q is the trapping efficiency, $\frac{nP}{c}$ is the incident momentum per second of a ray of power P in a medium of index of refraction n. As a conclusion, the fluctuations of an optically trapped particles depends on its size, the temperature and the viscosity of the immersed medium, the numerical aperture of the focusing beam, and the laser power.

7. 2.3 Force Calibration Methods

Calibration of the optical trap is necessary to determine the force acting on a micro/nano size object at a given position. An optically trapped particle, whose inertia is neglected, behaves as a damped harmonic oscillator. The linear equation of motion of a trapped particle in a harmonic potential is given by the reduced Langevin equation [27]:

$$\gamma \dot{x} + k[x(t) - x_{trap}(t)] = F_{thermal}(t) \qquad (7.9)$$

where first term, $\gamma \dot{x}$, represents the is the drag force, which is proportional to the velocity of the bead relative to a fixed position, second term, $k[x(t) - x_{trap}(t)]$, represents the optical force, and the third term, $F_{thermal}(t)$, represents random kinetic agitation, $x(t)$ is the particle position, $x_{trap}(t)$ is the trap position, $\gamma = 6\pi\eta a$ is the Stokes drag coefficient,

η is the dynamic fluid viscosity (here the medium is ethylene glycol), a is the radius of the particle, and k is the stiffness of the optical trap which is proportional to the trapping laser power. Since photon-particle interactions result in an effective restoring force of $F = -kx$, it is customary to describe trap behavior with the spring constant k, to be determined. In three dimensions, there are three spring constants to be found (k_x, k_y, k_z), expected to have lateral symmetry ($k_x \approx k_y$) with weaker strength along the optical axis ($k_z < k_x$).

The optical trap calibration methods described below involve observation of the particle's Brownian motion within the harmonic potential by measurement of displacement $r(t)$. Particles undergoing Brownian motion are characterized by Boltzmann energy $k_B T$, where k_B is the Boltzmann constant and T is the temperature of medium in Kelvin. The first calibration method uses the equipartition analysis of the form:

$$\frac{1}{2} k_B T = \frac{1}{2} k_i \langle \Delta r^2 \rangle = \frac{1}{2} k_i \, \text{var}(r) \tag{7.10}$$

By measuring the variance $\text{var}(r)$ of the particle displacements $r(t)$ for a known medium temperature, one can find the trap stiffness $k_i = \dfrac{k_B T}{\text{var}(r)}$, $i = x, y, z$.

The second method is based on the Boltzmann statistics, with the probability distribution of the particle displacements of the form:

$$P(r) = N_i e^{-\frac{E(r)}{k_B T}} \tag{7.11}$$

where $E(r)$ is the potential energy along the ith–axis and N_i are normalization constants. The parabolic potentials $E(r)$ are obtained in two ways: first way is to find the $P(r)_{fit}$

values by fitting the probability distribution with a Gaussian function, Figure 7.1a (red), after that the potential energy $E(r)$ in $k_B T$ is written as $E(r) = [\ln(P(r)_{fit}) - \ln(N_i)]$ which represents the parabola shape from Figure 7.1b. The second way to obtain the potential energy is to write the energy as $E(r) = k_i r^2 / 2$. The energy is known if we also have information about the spring constant k_i. We can use the spring constant values from the equipartition theorem but if we want to use the Boltzmann statistics only, the spring constant can be obtained by fitting a parabola to the experimental data, $E(r)$ (not in $k_B T$), This implies the spring constant $k_i = 2ak_B T$, where a is the coefficient of r^2 from the parabolic fit of $k_B T[\ln(N) - \ln(P(r))]$, and has the form: $a = -\dfrac{1}{\text{var}(r)} \ln\left[\dfrac{P(r)}{N_i}\right]$.

a)   b)
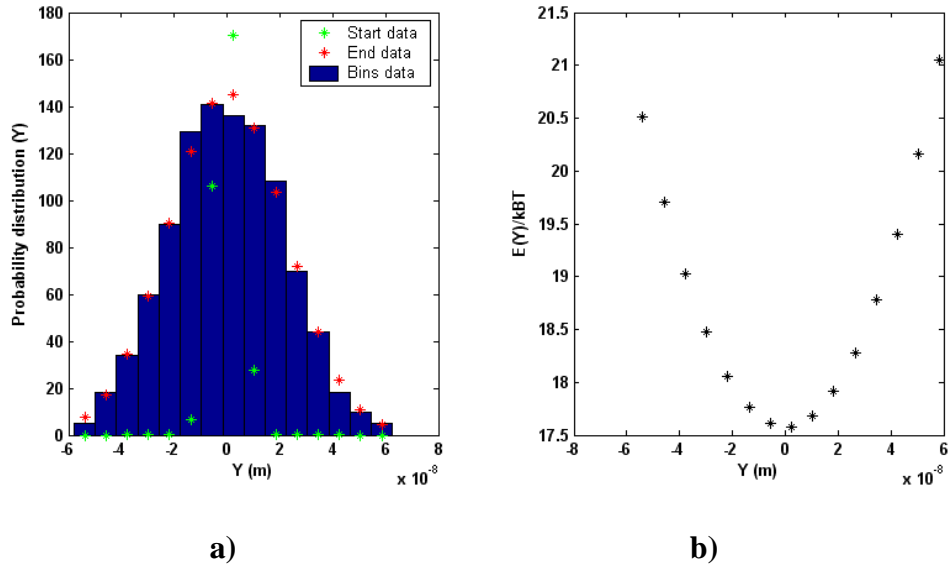
Figure 7.1. a) Particle Displacements Histogram, along y direction, frequency or counts (blue), starting Gaussian distribution (green), and ending Gaussian distribution (red); b) The potential energy in $k_B T$, derived from the probability distribution from Figure 7.1a.

7. 2.4. Computational System for Motion Tracking

The angular spectrum requires two Fourier transforms once the field is known at the hologram plane, one forward FFT to switch to the frequency space and one inverse FFT to return to the space domain obtain after the spectrum propagation to the object plane. Using a Pentium IV CPU, the time required to reconstruct 1000 holograms of 150 x 150 pixels is 100 seconds. GPGPU (General-purpose on graphics processing unit) computation with a CUDA (Compute Unified Device Architecture) based on C-like language allows numerical manipulation of data using a GPU (graphical processing unit) faster than CPU when big grid data arrays are involved. The GPU multi-parallel processors perform operations at 32-bit precision which make it highly useful for large data volume processing. Holograms are stored in the computer (CPU) and processed at a later time by the GPU. The GPU is a GeForce 8800 with 112 stream processors, memory of 512 Mbytes, and GPU clock of 1500 MHz, memory clock of 900 MHz. Holograms stored on the CPU are called by the CUDA functions and sent to the GPU memory. While there, the terms of Equation (7.3) are processed by the GPU chip. The reconstructed amplitude images and consequently the reconstructed (x,y,z) particle position of each hologram is transferred to the CPU.

7. 2. 5. Centroid Position Identification Algorithm

Single particle tracking algorithms usually are useful for motion tracking of objects of varying sizes such as molecules, biological cells, subcellular components, and microbeads. Three-dimensional tracking confers a problem since the lateral and axial resolution is not equivalent for the x, y, z axis. The center of mass does not have a

significant shift in the z-axis as it is in the x, y axis. Example of tracking algorithms are center-of-mass (centroid), cross-correlation, sum-absolute difference, and directly fitting Gaussian curves to the intensity profile [26]. Using digital Gabor holography, the best estimate of the z position is found for the amplitude maximum of the diffracted optical field, Figure 7.2. We recorded 1000 holograms and using GPGPU technology the reconstructed position (x, y, z) is determined for each of the reconstructed optical field. The particle is focused where the amplitude of the optical field, $A(x, y, z)$, is maximized, which is the pick in the Figure 7.2. If the axial range is Δz and we desire a precision of δz, set of $M = \Delta z / \delta z$ equally spaced axial positions are examined. As an example, the reconstruction distance is $3.5 \mu m$ and $M = 1000$, it means $\delta z = 3.5 nm$.
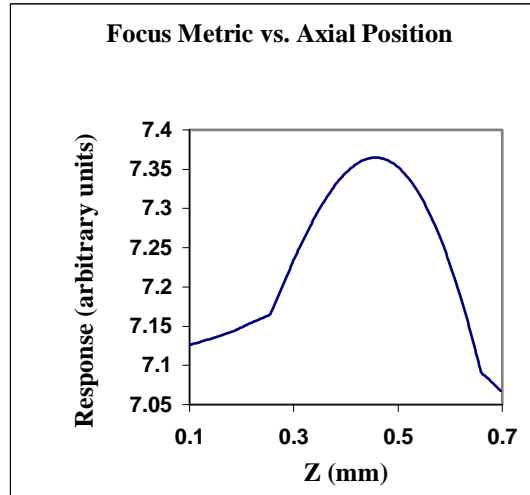
Figure 7.2. Centroid Position Identification.

Also, the center of the particle $c_o(x, y)$ is determined using a weighted average,

$$c_0(x, y) = \frac{\sum_{i,j} A(i, j) c_{i,j}(x_i, y_j)}{\sum_{i,j} A(i, j)}. \tag{7.12}$$

125

where the $A(i,j)$ is the amplitude of each pixel and $c_{i,j}(x_i,y_j)$ is the center of each pixel in the FOV. Thus, the centroid is the weighted average of the pixels by intensity. Nanometer precision is also obtained in the x, y directions due to the amplitude weighting and only fractional pixel lateral motion, noise and edge effects are negligible.

7. 3. Experimental Setup

Our sample was co-polyester particles of diameter $9.6\,\mu m$ from Duke Scientific Corporation with a 20% coefficient of variation. Particles were suspended in ethylene glycol with viscosity $\eta = 0.0161$ Nm/s^2. A custom-made sample chamber, Figure 7.3, consists of a microscope slide (the bottom), under a cover slip, spaced apart in z by parts from another cover slip, and sealed with glue.
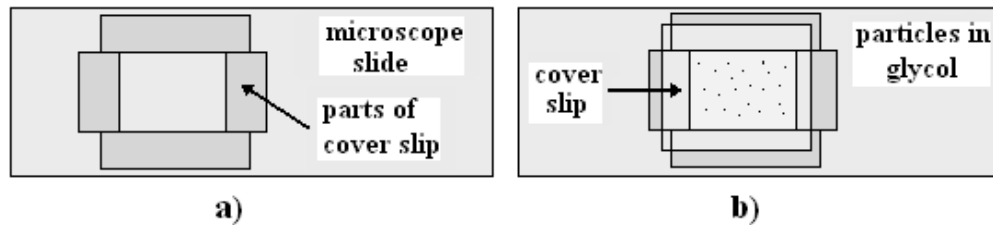
Figure 7.3. Optical Tweezers Sample Chamber; a) chamber made of microscope slide and parts of cover slip; b) chamber filled with particles immersed in ethylene glycol and covered by a cover slip.

A schematic of the experimental apparatus is shown in Figure 7.4. The setup consists of two arms. The digital Gabor holography arm is utilized for illumination/imaging and for three-dimensional position tracking. The trap arm is utilized

to trap the particle at the focus position of the high NA lens, MO2. Each of the two arms will be described in turn below.
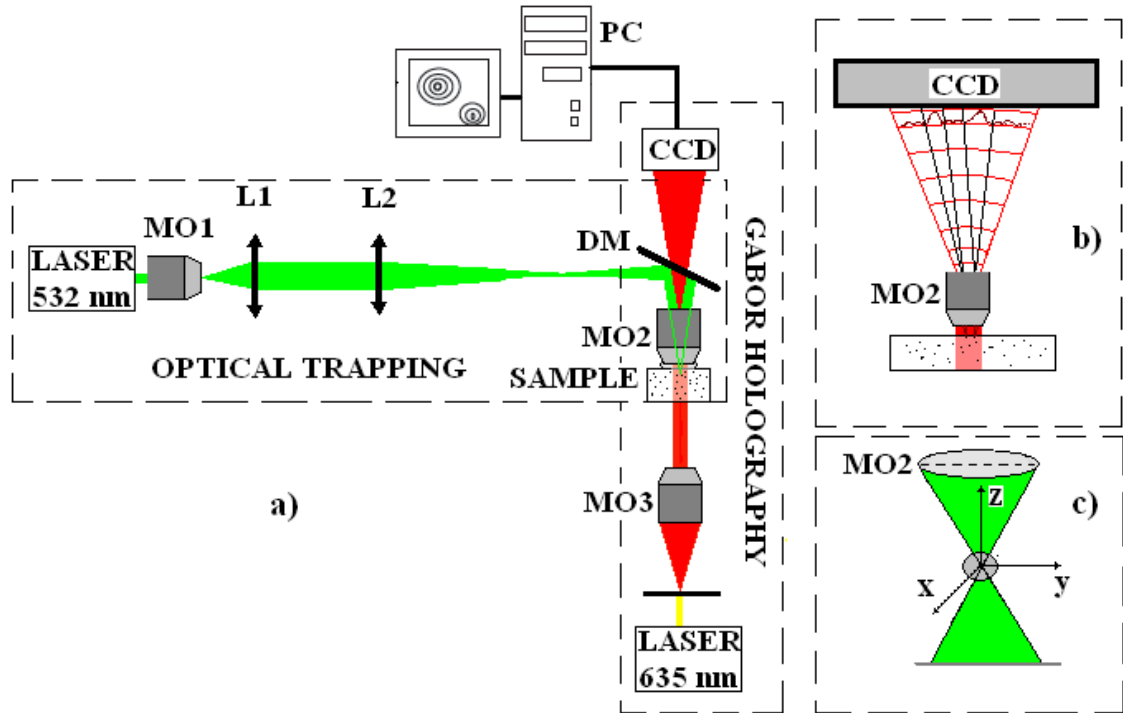
Figure 7.4. Optical Tweezers and Digital Gabor Holography Microscope; a) CCD, charged-coupled device camera, L's lenses, MO's, microscope objectives; b) Gabor holography illustration; c) Illustration of the focus position;

7. 3.1 Digital Gabor Holography Arm

A diode laser (635 nm) illuminates the sample from below, in transmission, along the DGH arm, Figure 7.3a, 7.3b. A fiber optic tip acts as a point source from where the light is radiated in spherical waves. The laser beam is collimated by a 4X microscope objective. Then it is diffracted (object wave) by the object points and interferes with the undiffracted (reference wave) light at the CCD plane to form a hologram. The imaging

lens is a Zeiss Plan-Neofluar 100X, 1.25 NA, oil-immersion objective with a back aperture of 6 mm. A red filter and a polarizer (not shown in the figure) are inserted between the CCD and the dichroic mirror. The red filter blocks reflections from the trapping light and the polarizer adjusts light intensity at the camera. A set of 1000 holograms are recorded in 100 seconds, by the CCD and saved into computer for post-processing.

7.3.2. Optical Trap Arm

A Millenia V Spectra Physics 532 nm laser is used to trap the particle, as shown in Figure 7.3a, 7.3c. The trapping beam passes through a combination of mirrors to position the beam at the desired height. Microscope objective MO1 expands the beam and the combination of L1 (f1 = 10cm), L2 (f2 = 15 cm) adjusts the beam diameter to just overfill the back aperture of the trapping optics. After that, the beam enters the microscope through a dichroic mirror. The dichroic mirror reflects the trapping beam and then it is focused by MO2, thus forming the optical trap near the sample plane. The front working distance is $0.17\,mm$, and the back image distance is 160 mm. The lens L2 with a focal length of 150 mm is positioned at 31 cm from the back of MO2. The dichroic mirror transmits the illumination beam and reflects the trapping beam. The trapping light backward-scattered by the trapped object has two parts; one is the reflected light outside of the microscope, and the other one, approximately 15% of the scattered light, arrives at the camera if the red filter is removed and may be used to initially find the focal position Figure 7.5a. Figure 7.5b shows an optically trapped bead with a field-of-view of $11.5x11.5\,\mu m$ or 150x150 pixels.
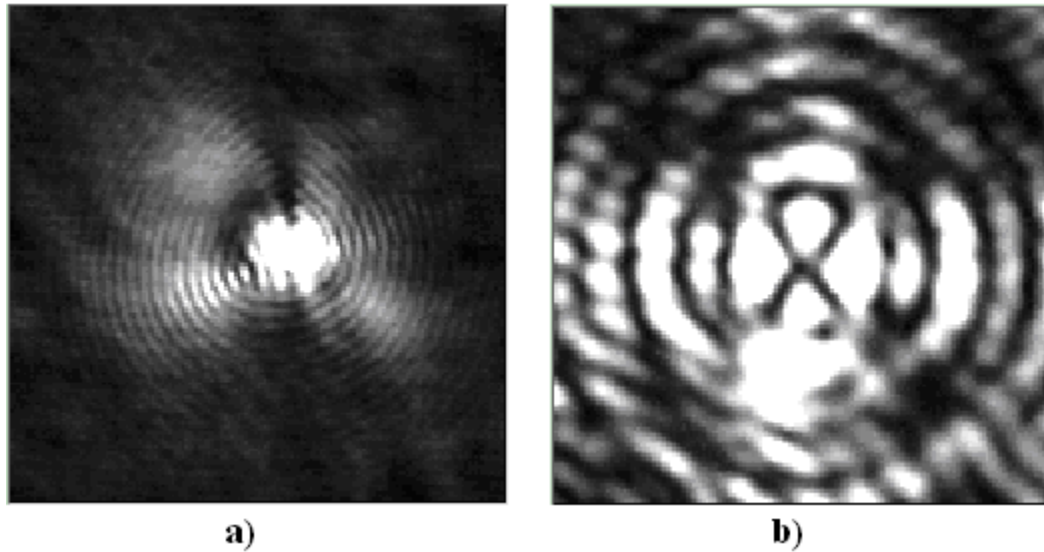
**Figure 7.5.** a) Focused Trapping Light; b) Optically trapped particle; FOV=11.5x11.5μm

or 150x150 pixels. .

7. 4. Results

We performed experiments on optically trapped co-polyester microspheres immersed in ethylene glycol, with viscosity of $\eta = 0.0161$ Nm/s^2 The tracking of a single particle along x, y, z axis is shown in Figure 7.5. We noticed a low frequency variation in the x, y data. This is due to the low speed CCD camera. We also noticed a drift in the z axis, noticing the particle tried to escape the trap.
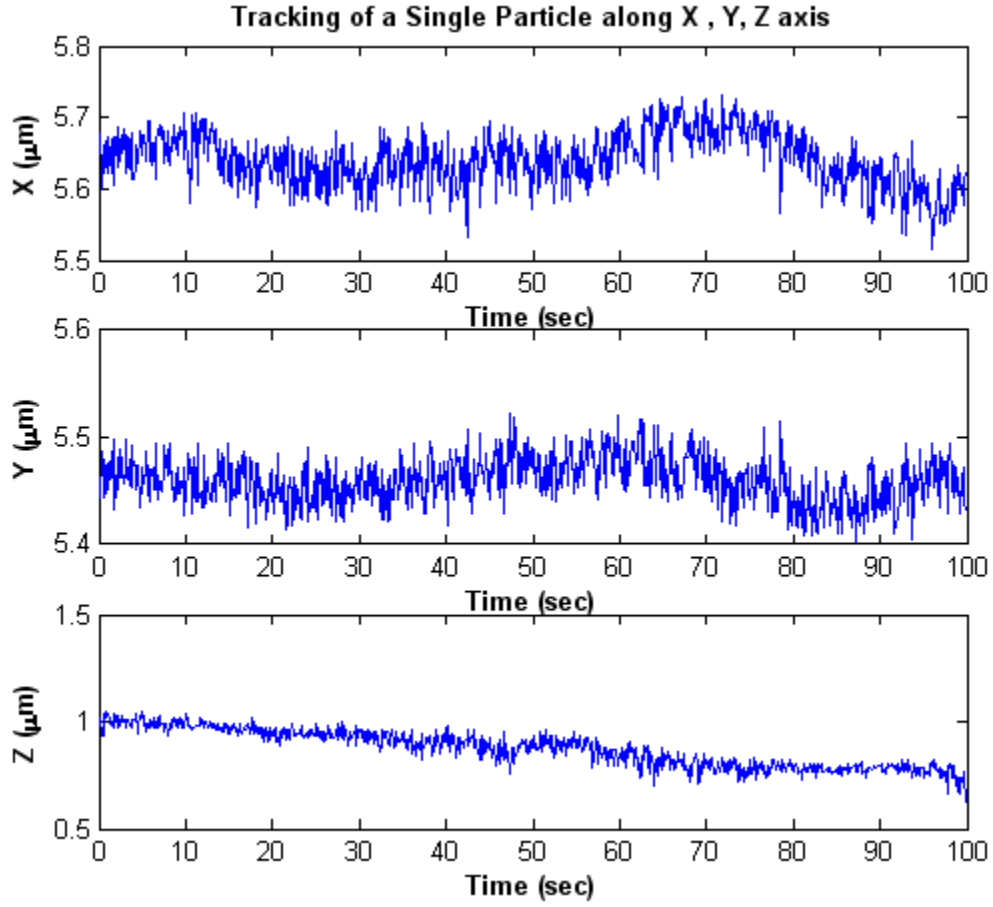
Figure 7.6. Three-Dimensional Single Particle Tracking Function of Time; a) along x axis; b) along y axis; and c) along z axis.

We obtained the mean-square –displacement (MSD), individual axis and 3D, from the measured displacements of an optically trapped microsphere in ethylene glycol according to the formula [28]:

$$MSD(n\delta t) = \frac{1}{(N-1-n)} \sum_{j=1}^{N-1-n} \left\{ [r(j\delta t) - r(n\delta t)]^2 \right\} \tag{7.11}$$

where, δt is the time resolution, and $r(j\delta t) - r(n\delta t)$ describe the particle position following a time interval $n\delta t$ after starting at position $r(j\delta t)$, N is the total number of frames, n, j integers.

Evidence for distinct trapping, hopping, and hindered-diffusive regimes are seen in the mean-square displacement and the probability distribution $P(x)$ [29]. Figure 7.7a, b depicts the MSD in x, y, z versus the time interval τ. Looking at the three graphs MSD_x, MSD_y, MSD_z versus the time interval $\tau = 25s$, Figure 7.7a, the MSD_x and MSD_y at first increase with increasing τ and later become stationary, Figure 7.7b. This behavior of the MSD shows clear evidence of the trapping.

a)   b)
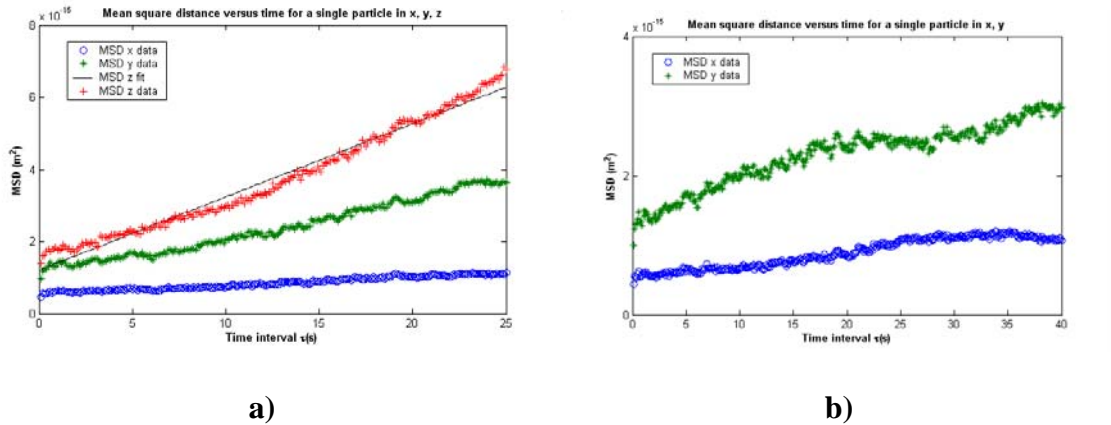
Figure. 7.7. The Mean-Square-Displacement Versus Time Intervals of an Optically Trapped Particle in Ethylene Glycol; a) MSD along x, y, z axis, $\tau = 25s$ b) MSD along x, y axis, $\tau = 40s$.

The MSD_z does not have the same trend as MSD_x and MSD_y since it first increase quickly; then attains a plateau and temporarily ceases to increase, Figure 7.8. Hopping

particle was observed to escape traps (the drift in z). At large τ the MSD_z of a hopping particle increases with increasing τ.
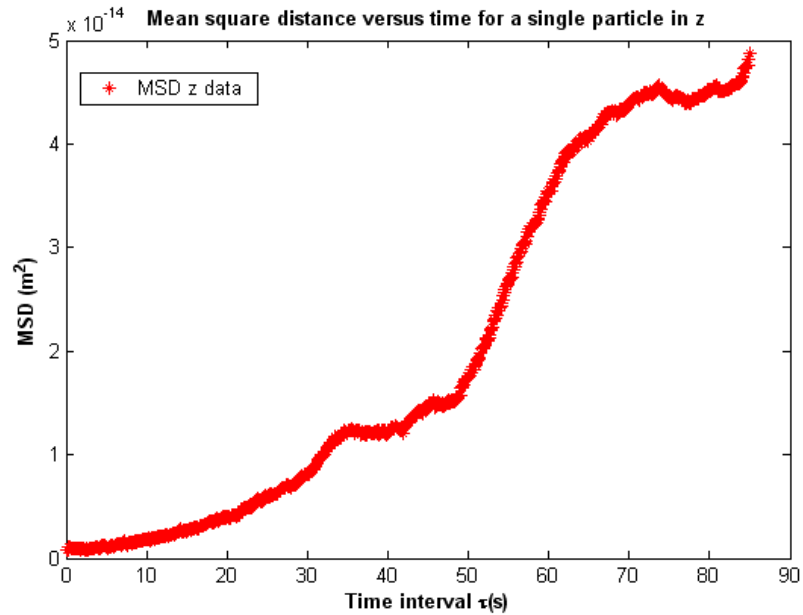

Figure. 7.8. The Mean-Square-Displacement in the Z direction Versus Time Intervals of an Optically Trapped Particle in Ethylene Glycol, along z axis, $\tau = 90s$.

Increasing the optical power of the trapping beam from 38 mW to 201 mW, the 3D distribution of the particle displacements becomes more compact as is shown in the Figure 7.9.
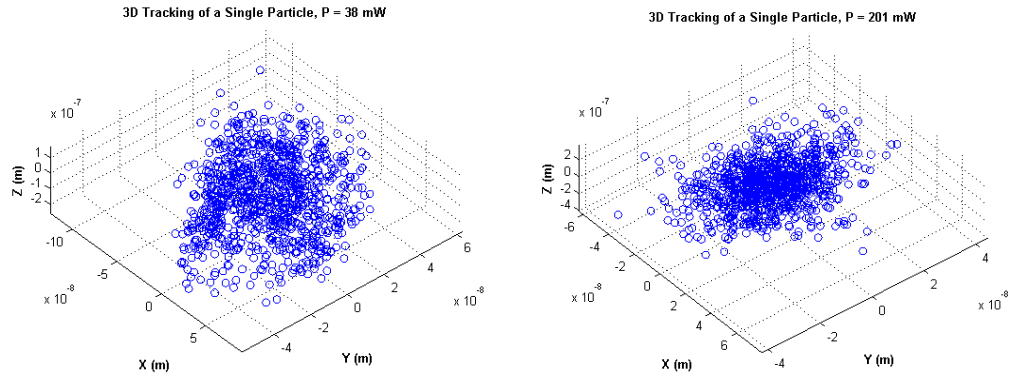
Figure. 7.9. 3D Scatterplots of an Optically Trapped Bead. a) The 3D distribution of the particle positions at the laser power P = 38 mW; b) The 3D distribution of the particle positions at the laser power P = 201 mW;

Using the equipartition theorem we calculated the spring constants k_x, k_y, k_z for each coordinate x, y, z and the results are graphed versus the laser power in Figure 7.10. The spring constant in the axial (z) direction is different from (and weaker than) the transverse (x and y) directions (in fact for nano/micro-particles the spring constants in x- and y- are also different from each other due to polarization induces symmetry breaking).
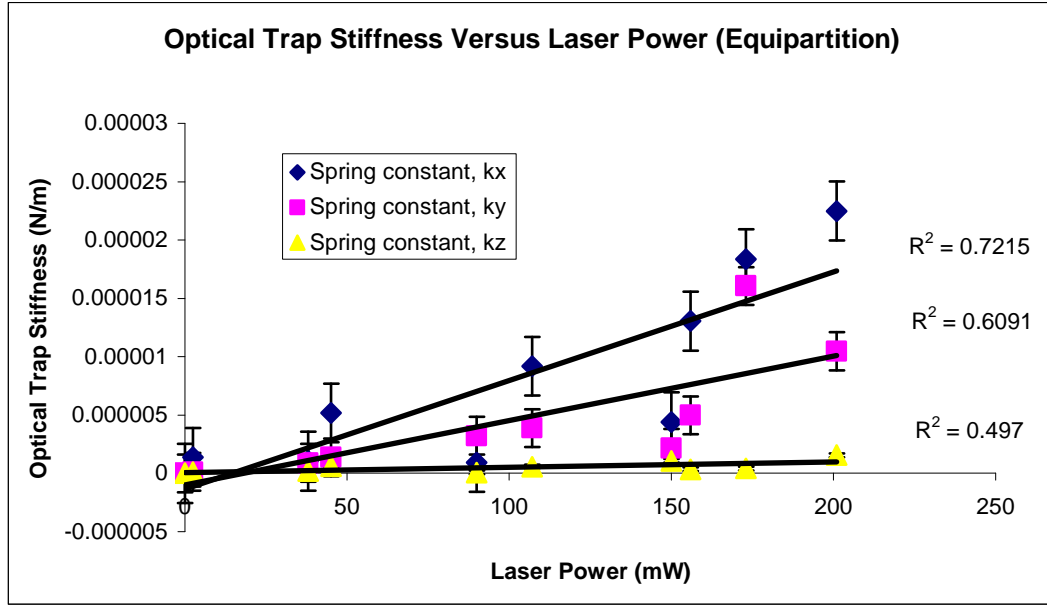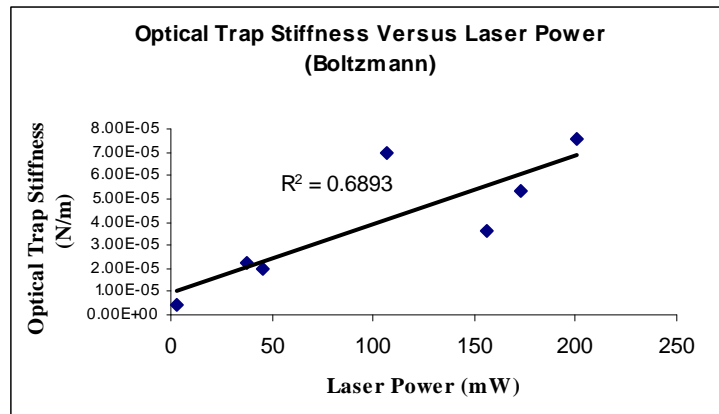
Figure. 7.10. Equipartition Calibration Method. Spring constant as a function of the laser beam power. R^2 (=Regression Sum Squares / Total Sum Squares) represents a figure of merit of curve fitting; $R^2 = 1$ means a perfect fit.

We also followed the procedure described by Equation (7.11). Probability distributions are fitted to a Gaussian curve to derive the potential energy for each x, y, z wells. In Figure 7.11a the optical parabolic potentials E(x), E(y), and E(z) are displayed for an optically trapped particle at P =38 mW. E(x) is stronger than E(y) and E(z). In Figure 7.11b the optical parabolic potentials E(x)'s for an optically trapped particle at P =2.5 mW, 45 mW, 107 mW, 156 mW, 173 mW, 201 mW are also shown. The correspondent spring constants are shown in Figure 7.12. The linearity between the spring constants and the laser power is preserved.
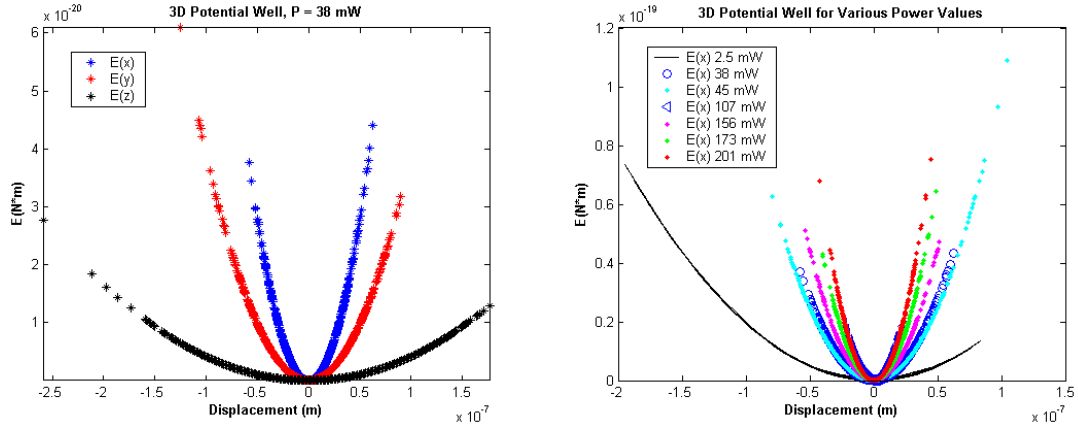
Figure. 7.11. Boltzmann Statistics Calibration Method. a) Optical parabolic potentials E(x), E(y), and E(z) for an optically trapped particle at P =38 mW. b) Optical parabolic potentials E(x)'s for an optically trapped particle at P =2.5 mW, 45 mW, 107 mW, 156 mW, 173 mW, 201 mW.

The narrow the displacement distribution is, the stronger the stiffness of the potential well is. As we see the E(x) becomes steeper and the force constant becomes larger and larger once the optical power increases.

Figure. 7.12. Boltzmann Statistics Calibration Method. Spring constant as a function of the laser beam power. R^2 (=Regression Sum Squares / Total Sum Squares) represents a figure of merit of curve fitting; $R^2 = 1$ means a perfect fit.

7. 5. Conclusions

We have demonstrated how one may calibrate an optical tweezers based on digital Gabor holography of a co-polymer particle. We have characterized the Brownian motion as an essential element for optical force calibration using optical tweezers. Spring constants and subsequently force measurements were measured from the statistical analysis of the oscilations of the optically trapped particle. The 3D position is tracked by analysis of the complex optical field reconstructed via the angular spectrum method. Stiffness of the optical trap is calculated by three calibration methods: equipartition theory, and Boltzmann statistics. The results confirm the linear relationship between the stiffness and the trapping laser power. The values of the spring constants of the radiation force, in the axial (z) direction is different from (and weaker than) the transverse (x) and (y). The digital Gabor holography microscope together with the optical trapping arm can be used as a new tool to study how cells ingest foreign particles through the process known as phagocytosisa, and to understand a variety of biophysical processes such as organelle–membrane interactions or the cytoskeletal rearrangements. Moreover, the digital interference holography techniques could be combined with optical tweezers to monitor and quantify membrane physical properties as a response to the evolution of the malaria parasite acting on erythrocytes. The three-dimension map of cell refractive index gives subsequently information of nanoscale cell membrane thickness fluctuation in infected erythrocytes, which is the leading factor in quantifying the cell deformation. Another possible investigation is to understand the cytoadherence of infected cell under physiological shear stresses in blood vessels and capillaries monitoring healthy and infected cells on various substrates.

Acknowledgments

7. 6. Bibliography

[1]. M.J. Lang, P.M. Fordyce, A.M. Engh, K.C Neuman, S. M. Block, "Simultaneous, coincident optical trapping and single molecule fluorescence," Nature Methods **1**, 133-139 (2004)

[2]. S. M. Block, "Fifty ways to love your lever: myosin motors," Cell **87**, 151-157 (1996).

[3]. Macdonald MP, Spalding GC, Dholakia K, "Microfluidic sorting in an optical lattice," Nature **421**: 421-424 (2003).

[4]. K. Ladavac, K. Kasza and D. G. Grier, Physical Review E **70**, 010901(R) (2004).

[5]. S. Kawata and T. Sugiura, Opt. Lett. **17**, 772 (1992).

[6]. M. Righini, G. Volpe, G, C. Girard, D. Petrov, and R. Quidant, "Surface Plasmon Optical Tweezers: Tunable Optical Manipulation in the Femtonewton Range," Phys. Rev. Lett. **100**, 186804 (2008).

[7]. P Domachuk, F G Omenetto, B J Eggleton and M Cronin-Golomb, "Optofluidic sensing and actuation with optical tweezers," J. Opt. A: Pure Appl. Opt. **9** S129-S133 (2007).

[8]. K. Uhrig, R. Kurre, Christian Schmitz, Jennifer E. Curtis, et al**.,"** Optical force sensor array in a microfluidic device based on holographic optical tweeze**",** Lab Chip**, 9**, 661 – 668 (2009).

[9]. A. Ashkin, "Acceleration and trapping of particles by radiation pressure," Phys. Rev. Lett. **24**, 156-159, (1970).

[10]. A. Ashkin and J..M. Dziedzic, "Optical levitation by radiation pressure," Appl. Phys. Lett., 1971.

[11]. A. Ashkin, J..M. Dziedzic, J.E. Bjorkholm, and S. Chu, "Observation of a single-beam gradient force optical trap for dielectric particles," Optics Lett., (1986).

[12]. J. E. Curtis, B. A. Koss and D. G. Grier, "Dynamic holographic optical tweezers, " *Optics Communications* **207**, 169-175 (2002).

[13]. D. G. Grier, "A revolution in optical manipulation*," Nature* **424**, 810-816 (2003).

[14]. B. Sun, Y. Roichman and D. G. Grier, "Theory of holographic optical trapping, " *Optics Express* **16**, 15765-15776 (2008).

[15]. M. K. Kim, "Tomographic three-dimensional imaging of a biological specimen using wavelength-scanning digital interference holography," Opt. Express; **7**: 305-310 (2000).

[16]. M. K. Kim, L. Yu and C. J. Mann. Interference techniques in digital holography. J. Opt. A: Pure Appl. Optics.; **8**:512-523 (2006).

[17]. M. C. Potcoava, and M. K. Kim, "Optical tomography for biomedical applications by digital interference holography," Meas. Sci. Technol**.** 2008; **19**: 074010 (2008).

[18]. G. Mie, "Articles on the optical characteristics of turbid tubes, especially colloidal metal solutions," Ann. Phys.-Berlin **25**, 377-445 (1908).

[19]. K. C. Neuman and S. M. Block. Optical trapping. Rev. Sci. Instr., **75**, 2787–2809 (2004).

[20]. L. P. Ghislain and W. W. Webb, "Scanning-force microscope based on an optical trap," *Opt. Lett.*, **18**, pp. 1678–1680 (1993).

[21]. L. P. Ghislain, N. A. Switz, and W. W. Webb, "Measurement of small forces using an optical trap," *Rev. Sci. Instrum.*, **65**, 2762–2768 (1994).

[22]. J. R. Moffitt, Y. R. Chemla, D. Izhaky, and C. Bustamante, "Differential detection of dual traps improves the spatial resolution of optical tweezers," PNAS, **103**, 9006–9011 (2006).

[23]. A. Carter, G. King, T. Ulrich, W. Halsey., D. Alchenberger, and T. Perkins, "Stabilization of an optical microscope to 0.1 nm in 3D," Appl. Optics. **46**, 421-427 (2007).

[24]. W. P.Wong, and K. Halvorsen, "The effect of integration time on fluctuation measurements: calibrating an optical trap in the presence of motion blur," *Optics Express* **14**, 12517-12531 (2006).

[25]. M. L. Salit and G. C. Turk, "A Drift Correction Procedure, "Anal. Chem. **70**, 3184-3190 (1999).

[26]. M K Cheezum, W F Walker, and W H Guilford, "Quantitative comparison of algorithms for tracking single fluorescent particles," Biophys J. **81**, 2378–2388 (2001).

[27]. S. F. Tolic-Nørrelykke, E. Schäffer , J. Howard, F. S. Pavone, F. Jülicher, H. Flyvbjerg, "Calibration of optical tweezers with positional detection in the back focal plane", REVIEW OF SCIENTIFIC INSTRUMENTS **77**, 103101 2006

[28]. Sako, Y., and A. Kusumi. 1994. Compartmentalized structure of the plasma membrane for receptor movements as revealed by a nanometer-level motion analysis. *J. Cell Biol.* 125:1251–1264.

[29]. L. Luo, G. D. J. Phillies, "Brownian motion through a two-dimensional glass: Trapping, hopping, and diffusion", J. Chem. Phys. 105 (2) (1996).

CHAPTER 8

CONCLUSIONS AND FUTURE WORK

8. 1 Conclusions

In this dissertation, I have demonstrated and applied the latest development of digital holography techniques. Results confirm the capability of digital interference holography instrument (DIH) to image in-vitro human macular, optic nerve tissue, and fingerprint patterns. This work is to my knowledge a novel and innovative approach to ophthalmic and fingerprint imaging. I have also successfully demonstrated the Brownian motion tracking of the optically trapped particles by digital Gabor holography. I have demonstrated the capability of digital interference holography to produce micron-size images without out-of-focus of the entire specimen.

First, I have characterized the digital interference holography systems in terms of wavelength scanning capabilities. The scanning time is 30 s and the signal-to-noise ratio (SNR) is about 50 dB. The axial resolution is a parameter that depends on the wavelength scanning range and is obtained by superposing all optical fields. The axial resolution of the system is $5 \mu m$. Calibration experiments using a resolution target demonstrates improvement of SNR with increasing number of holograms consistent with theoretical prediction. The SNR of tissue images, 50 dB is comparable to that of the resolution target, implying the imaging system is operating at close to theoretical optimum.

Tunable lasers are particularly sensitive to chromatic-dispersion, $n(\lambda)$, characteristics of materials, in particular second-order k'' and third order dispersion k''', which typically cause broadening of the axial point spread function. I introduced and demonstrated a phase-matching scheme to make consecutive wavelength phase differences as identical as possible.

Imaging experiments on retinal tissue reveal topography of blood vessels as well as optical thickness profile of the retinal layer. I have already demonstrated that, in vitro, DIH can measure the dimensions of the scleral ring and provide an answer regarding the size of the optic disk, a clinically important parameter. The disc diameter is about 1750 μm, and the cup depth is about 240 μm. The depth between the retinal fiber and the retinal pigmented epithelium layers is about 84 μm.

This method could be applied in ophthalmology as a noninvasive, high speed tool to image the retinal and choroidal sub-structure and have significant applications in a variety of retinal disorders, especially macular degeneration, diabetic retinopathy and glaucoma.

This research has also shown how the DIH technique could be used in the field of forensic science as a fingerprint scanner to identify and quantify Level 1 (pattern), Level 2 (minutia points), and Level 3 (pores and ridge contours) fingerprint characteristics from amplitude images.

The optical thickness profile of a transparent object can be obtained from quantitative phase images. Usually, two important parameters are subsequently derived from the optical thickness profile, the physical thickness and the index of refraction of the sample. Holographic phase microscopy DIH is used to produce images of thin film

patterns left by latent fingerprints. The optical thickness range of the latent fingerprints was 136 μm concerning with our experiment. These results have revealed the DIH is highly effective for biometry applications.

Furthermore, I have demonstrated a new technique for position and force calibration of optically trapped particles combined with digital Gabor holography. The system offers high-resolution 3D particle-tracking capabilities. The Gabor holography instrument is used to track and monitor co-polyester microsphere beads moving in depth over time, and when an optical trapping arm is attached to the microscope, the system can track and monitor optically trapped small objects undergoing Brownian motion. The 3D position is tracked by analysis of the complex optical field reconstructed via the angular spectrum method. Stiffness of the optical trap is calculated by two calibration methods: equipartition theory, and Boltzmann statistics. The results confirm the linear relationship between the stiffness and the trapping laser power. The values of the spring constants of the radiation force, in the axial (z) direction is different from (and weaker than) the transverse (x) and (y). The average values of the spring constants are: the spring constant along x axis $kx = 7.6 * 10^{-6} N/m$, the spring constant along y axis $ky = 4.8 * 10^{-6} N/m$, and the spring constant along z axis $kz = 5.0 * 10^{-7} N/m$.

Optical tweezers in addition to digital holography can investigate systematically the large deformation characteristics of the human red blood cell infected by malaria parasite and to perform quantitative assessment and optimization of a variety of surface attachment technique.

8. 2 Future Work

8.2.1 Tunable Source and the Wavelength Scanning System

I have developed a modification of the hologram exposure method so that the holograms are taken at equal intervals of wave vectors, not wavelengths (Figure D. 4). I noticed no improvement in the SNR of the reconstructed images. I believe the DIH imaging dynamic range or SNR will be improved by replacing the dye laser with a swept source, introducing a high-speed camera and increasing the number of recorded holograms.

The light source is one of the most important components in any wavelength scanning imaging system. At this point, our scanner has to overcome the signal-to-noise ratio issue, to provide clinically relevant information. The scanning time is 30 s and the signal-to-noise ratio (SNR) is about 50 dB. A swept light source with an appropriate actuator and a sweep function parameterized by time is desirable for the DIH system to improve the system performance. Important key parts of a swept source are the optical gain medium and the linearity of the light source (data recorded evenly in k space). Research based on the use of semiconductor optical amplifier (SOA) as optical gain medium was already demonstrated [1-3].

8.2.2 Multiplicative Noise (Speckle) Reduction

The digital interference holography apparatus needs improvement in terms of speckle, energy loss, and other noise introduced by the stray reflections or CCD.

There are two types of noise that we encounter in imaging systems, additive and multiplicative. The additive noise is not part of the signal and is spatially uncorrelated, this means the noise for each pixel is independent and identically distributed (*iid*). Also, it

may be caused by a wide range of sources, *e.g.* variations in the detector sensitivity, environmental variations, the discrete nature of radiation, transmission or quantization errors, *etc.* In multiplicative noise, speckle is dependent on image data and it arises when the radiation is scattered by the object.

Digitally recorded and reconstructed holograms contain not only spectral information but also the coherent noise, speckle, introduced by the illumination source, in our case the laser, which decreases the spatial resolution of the image. When coherent radiation is reflected, the surface imperfections of the illuminated object generate a random interference that corrupts the image with a diffuse pattern called speckle noise, which is very difficult to filter because of its random and multiplicative nature.

Speckle noise is a common phenomenon in all coherent imaging systems like laser, acoustic and SAR imagery [4, 7, 10]. Its undesired effect was recognized from the very beginning of holography [5, 8]. The digitally recorded and reconstructed data are stored in the computer as complex numbers. To improve the spatial resolution and image quality of holographic images, the complex noise stored with the data can be reduced by applying various speckle reduction filters [6, 7].

Our scanning digital interference system does not benefit from these approaches. The coherent noise level explodes with the increasing of the laser intensity in the time of the wavelength scanning and we cannot control it.

Goodman [8] showed that the speckle can be reduced by superimposing M uncorrelated speckle patterns using an active diffuser placed in an intermediary image plane. The active diffuser is moved in the intermediate image plane in a rotation about a display system optic axis in order to create a shifting phase at a display screen. Moreover,

all *M* independent speckle configurations have equal mean intensities and the speckle contrast is reduced from 1 to $1/M^{1/2}$.

In our noise multiplicative model the observed value E_2 will be modeled as a random variable resulting from the product of two independent random variables, which correspond to the image in the reconstructed optical field E_1 and the stationary multiplicative noise n.

After elimination of zero-order term and virtual image, the real image optical field E_2 can be represented as: $E_2 = nE_1$, where $E_1 = E_0 \exp(i\varphi_0)$, and $n = E_n \exp(i\varphi n)$, $E_2 = nE_1 = nE_0 \exp[i(\varphi_0 + \varphi_n)]$. The intensity distribution of this optical field becomes $I = E_2 E_2^* = E_n^2 E_0^2$. If *M* holograms of the same scene and wavelength are recorded, each of them is individually reconstructed and added on an intensity basis. The result contains the object information E_0^2 and a new noise n_{new}, where $n_{new} = \sum_{i=0}^{N-1} E_{n_M}^2$.

This noise can be characterized as random multiplicative noise, following a Gamma distribution as both real and imaginary parts of the speckle have zero-mean Gaussian density, and the contrast of this type of distribution behaves as $1/M^{1/2}$ [8, 11]. A motorized diffuser will be added in the front of the object, and it will rotate in N different positions but remain motionless during the detector's integration time.

8.2.3 Fundus Camera Adaptation for Digital Interference Holography Imaging

Imaging measurements and experiments will be performed using the fundus camera. The performances will be assessed and optimized to be compatible with current ophthalmic

imaging applications. The retinal camera is a model TRC-50X (mydriatic retinal camera); Topcon Corp., Tokyo, Japan equipped with a digital back piece, MEGAPLUS model 1.4; Eastman Kodak, San Diego, CA and a PC-based image-management system (Ophthalmic Imaging Systems Inc., Sacramento, CA).

The fundus camera will be incorporated into the optical design in the object arm, and the reference arm length has to be modified in order to match the coherence length of the laser beam. The light coming from the laser reflects back from the object (the fundus camera image) and the reference mirror, interfere both at CCD plane and form the interference patern.

A few methods have been previously reported [8] for holographic imaging of the eye using a fundus camera. A modified Zeiss fundus camera was used [9] to obtain holograms. Resolution near the resolution limit of the camera, 20 μ m, has been obtained in holograms of the fundus of anaesthetized cats.

Finally, the laser power has to be modified to agree with the American Conference of Government Industrial Hygienists (ACGIH) standards. Then, the DIH setup will be substantially improved and suitable for clinical usage.

8.2.4 Integrated optical diagnostics technique to investigate mechanical properties of single erythrocytes infected with malaria parasite

A *Plasmodium falciparum (Pf)* is a malaria parasite which infects human erythrocytes, resulting in changes in their biological functions and modifications to their physical properties. Notable changes in physical characteristics of the cell membrane, such as elasticity and permeability, have been observed and believed to be inter-related with the

147

adherence force of erythrocytes to endothelial cells. However, there has been no systematic, quantitative study of this aspect. Erythrocyte membrane provides a barrier maintaining the integrity of the cell and consists of three major components: a mixed lipid-protein bilayer; a cytoskeletal network structure whose main components are spectrin proteins [12, 13], and transmembrane proteins such as glygoproteins, band 3, and glygophorin. Stability in the macroscopic characteristics of the plasma membrane is the key to maintain the physical integrity and biological function of the cell. In the macroscopic scale, differences in mechanical properties between healthy and malaria-infected cells have been investigated in an effort to develop image-based single cell diagnostics. Healthy red blood cells experience numerous deformations and significant shape changes in flow, being squeezed and elongated through narrow capillaries [14]. On the other hand, the elasticity of *Pf*-infected cells is substantially decreased and tend to aggregate in a blood vessel. Furthermore, infected cells tend to adhere to endothelial cells, where *Pfs* export proteins to the erythrocyte plasma membrane to result in protein-rich "knob" regions in the membrane, enabling the infected cells to readily adhere to the receptors of endothelial cells [15] The expression of "knob" proteins on the membrane may induce sub-micron scale "flicker" motion of the membrane, which is also associated with the cooperative motion between its cytoskeleton and lipid bilayer. The key hypothesis of a future experiment will be that this sub micron scale membrane fluctuation influences the cytoadherence of erythrocytes to endothelial cells. In malaria disease, adherence of erythrocytes to endothelial cells is one of the key processes of human infection. Therefore, measurements will focus on inter-relating the cytoadherence properties with submicron scale mechanical motion of the membrane.

The idea is to develop a novel imaging method where digital interference holography technique is combined with optical tweezers to enable quantitative dynamical imaging of single erythrocytes in a native condition. The role of optical tweezers is two-fold: (1) immobilizing erythrocytes without attaching them onto a substrate to enable imaging them in a native condition; (2) assessing adherence force of erythrocytes on the surface of a monolayer of endothelial cells or on the surface of biomimetic substrates of endothelial cells. Erythrocytes which are attached onto a biomimetic substrate mimicking endothelial cell surface can be shear-stretched by optical tweezers to assess the stretching behaviors between normal cells and infected cells. Shear modulus calculation using digital interference holography will be performed and compared with the shear modulus obtained by the optical tweezers.

We expect to build up the 3D structure of the cell by digital interference holography, to extract the three- dimensional cell thickness fluctuation maps, and to quantify the elastic shear modulus using both optical tweezers technique and the digital holography on a variety of substrates. A list of potential impact areas includes better understanding of the pathophysiology of the disease, the development of medical diagnostic devices that are not only novel, portable and inexpensive, but also accessible to the developing world where some diseases are especially rampant.

8. 3 Bibliography

[1]. R. Huber, M. Wojtkowski, K. Taira, J. G. Fujimoto, K. Hsu, Amplified, frequency swept lasers for frequency domain reflectometry and OCT imaging: design and scaling principles, *Opt. Express* 13, no. 9, pp. 3513-3528, 2005.

[2]. R. Huber, M. Wojtkowski, J. G. Fujimoto, Fourier Domain Mode Locking (FDML): a new laser operating regime and applications for optical coherence tomography, *Opt. Express* 14, no. 8, pp. 3225-3237, 2006.

[3]. Youxin Mao, Costel Flueraru, Sherif Sherif, Shoude Chang, "High performance wavelength-swept laser with mode-locking technique for optical coherence tomography," *Optics Communications, 282, 1067(2009).*

[4] H. H. Arsenault, G. April, Properties of Speckle Integrated with a Finite Aperture and Logarithmically Transformed",

J. Opt. Soc. Am., Vol. 66, pp. 1160-1163, 1976

[5] D. Gabor, ,Laser speckle and its elimination', IBM J Res. Develop. 14, 509, 1970.

[6] L. Gagnon, ,Wavelet Filtering of Speckle Noise - Some Numerical Results', *Vision Interface '99, Trois-Rivières, Canada, 19-21 May,1999.*

[7] L. Gagnon and A. Jouan, Speckle Filtering of SAR Images - A Comparative Study Between Complex-Wavelet-Based and Standard Filters, SPIE Proc. #3169, conference "Wavelet Applications in Signal and Image Processing V", San Diego, 1997

[8] J. W. Goodman, Some Fundamental Properties of Speckle", J. Opt. Soc. Am., Vol. 66, pp. 1145-1150, 1976

[9] E. N. Leith and J. Upatnieks, ,Wavefront reconstruction with diffused ilumination and three-dimensional objects', J. Opt. Soc. Am. 54, 129, 1964.

[10] J. S. Lim, H. Nawab, Techniques for Speckle Noise Removal", Opt. Engineering, Vol. 20, pp. 472-480, 1981

[11] J. Trisnadi, „Hadamard speckle contrast reduction", Opt. Lett. 29, 11, 2004.

[12]. Browicz, T. 1890. Further observation of motion phenomena on red blood cells in pathological states. Zbl. med. Wissen. 28:625–627.

[13]. Parpart, A. K., and J. F. Hoffman. 1956. Flicker in erythrocytes; vibratory movements in the cytoplasm. J. Cell. Physiol. 47:295–303.

[14]. Skalak, R. and Branemark, P. (1969) Deformation Of Red Blood Cells In Capillaries. Science, 164, 717.

[15]. G. Crivat, J. M. Sa, F. Tokumasu, T. E. Wellems, and J. Hwang, Fluorescence Reporter Protein for Studying the Protein Trafficking of Malaria Infected Human Red Blood Cell, Conference Poster.

REFERENCES

J.W. Goodman, *Introduction to Fourier Optics*, *Third Edition*, Roberts and Company Publishers, Inc., Englewood, CO (2005).

P. Hariharan, *Optical Interferometry, Second Edition***,** Academic Press ISBN 0123116309 (2003).

U. Schnars, W Jueptner, *Digital Holography: Digital Hologram Recording, Numerical Reconstruction, and Related Techniques,* Springer; ISBN: 354021934X (2004).

C. Scott, *Introduction to Optics and Optical Imaging*, IEEE Press, ISBN: 078033440X (1998).

R. Jones and C. Wykes, *Holographic and Speckle Interferometry, Second Edition*, Cambridge University Press, ISBN: 052134417 (1989).

C. J. Kuo and M. H. Tsai, *Three-Dimensional Holographic Imaging*, John Wiley and Sons, Inc., ISBN: 0471358940 (2002).

L. Yaroslavsky and M. Eden, *Fundamentals of Digital Optics*, Birkhauser Boston, ISBN: 0817638229 (1996).

G. Saxby, *Practical Holography, Prentice Hall International* (UK) Ltd, ISBN: 0136937977 (1988).

D. Clarke and J. F. Grainger, *Introduction to Polarized Light and Optical Measurement*, Pergamon Press., ISBN: 080163203 (1971).

APPENDICES

Appendix A: Digital Interference Holography Wavelengths Superposition

The electromagnetic signal is represented as a pair of real and imaginary signals. By convention, the measured signal is the real signal. As an example, the sinusoidal time varying signal has the expression,

$$\psi(z;t) = Ae^{i(kz-wt)} = u(z)e^{-i(wt)} = Ae^{i\varphi(z)}e^{-i(wt)} \qquad (A.1)$$

where A is the amplitude, $(kz - wt)$ is the absolute phase, $k = \dfrac{2\pi}{\lambda}$ is the wavevector, $w = 2\pi f$ is the angular frequency, f is frequency, t is the time, z is the propagation distance. Also, the function $u(z) = Ae^{i\varphi(z)}$ is called phasor, or complex amplitude of the signal, and $\varphi(z) = kz$ is called the phase.

The real part of the Equation. (A.1) is $E = \Re[Ae^{i(kz-wt)}] = A\cos(kz - wt)$. Ignoring the time variation of Equation. (A.1), we obtain the expression:

$$u(z) = Ae^{i\varphi(z)} = Ae^{i(kz)} = A\cos(kz) \qquad (A.2)$$

In the digital interference holography, we perform wavelength scanning and a hologram is recorded for each wavelength. The superposition of the reconstructed optical fields or cosine waves $u_i(z) = A_i e^{i\varphi_i(z)} = A_i e^{i(k_i z)} = A_i \cos(k_i z)$ for each wavelength λ_i behaves as a periodic function of pulse-like picks with the period $\Lambda = \dfrac{\lambda_c^2}{\delta\lambda}$, and the width of each pulse $\delta z = \dfrac{\Lambda}{N} = \dfrac{\lambda_c^2}{N\delta\lambda} = \dfrac{\lambda_c^2}{\Delta\lambda}$. Here, N is the number of wavelengths, λ_c is the

central wavelength of the wavelength range, $\delta\lambda$ is the wavelength increment, and $\Delta\lambda$ is

the wavelength range. If we consider the amplitude of each wave, A_i, being constant over

the wavelength range, and each $k_i = \dfrac{2\pi}{\lambda_i}$ with an increment of

$\Delta k = k_{max} - k_{min} = \dfrac{1}{\lambda_{max}} - \dfrac{1}{\lambda_{min}}$, the addition of the N waves has the expression:

$$\sum_{i=1}^{N} e^{ik_i z} = e^{ik_1 z} + e^{ik_2 z} + e^{ik_3 z} + \ldots + e^{ik_i z} = e^{ik_1 z}(1 + e^{i\Delta kz} + e^{i2\Delta kz} + e^{i\Delta kz} + \ldots + e^{i(N-1)\Delta kz}) \quad \text{(A.3)}$$

The summation of the exponential function is a geometric progression with a

constant ratio of $r = e^{i\Delta kz}$. The Equation (A.3) becomes,

$$\sum_{i=1}^{N} e^{ik_i z} = e^{ik_1 z}(1 + e^{i\Delta kz} + e^{i2\Delta kz} + e^{i3\Delta kz} + \ldots + e^{i(N-1)\Delta kz}) = e^{ik_1 z}\dfrac{1 - e^{iN\Delta kz}}{1 - e^{i\Delta kz}}$$

$$= e^{ik_1 z}\dfrac{(e^{iN\Delta kz} - 1)}{(e^{i\Delta kz} - 1)} = e^{ik_1 z}\dfrac{e^{i\frac{N\Delta kz}{2}}(e^{i\frac{N\Delta kz}{2}} - e^{-i\frac{N\Delta kz}{2}})}{e^{i\frac{\Delta kz}{2}}(e^{i\frac{\Delta kz}{2}} - e^{-i\frac{\Delta kz}{2}})} \quad \text{(A.4)}$$

Using the exponential expression for $\sin x = \dfrac{e^{ix} - e^{-ix}}{2}$, we get,

$$\sum_{i=1}^{N} e^{ik_i z} = e^{ik_1 z}\dfrac{e^{i\frac{N\Delta kz}{2}}}{e^{i\frac{\Delta kz}{2}}}\dfrac{\sin(\dfrac{N}{2}\Delta kz)}{\sin(\dfrac{1}{2}\Delta kz)}. \quad \text{(A.5)}$$

We know the wavevector is proportional with the reciprocal of the wavelength,

$k = \dfrac{2\pi}{\lambda}$. The derivative of the wavevector is $dk = 2\pi\dfrac{\delta\lambda}{\lambda_c^2} = \dfrac{2\pi}{\Lambda}$, the period of the pulses

in the optical field superposition function has the form $\Lambda = \dfrac{2\pi}{\delta k}$, and the width of each

pulse is $\delta z = \dfrac{\Lambda}{N}$, where N is the number of wavelengths. We also call Λ the axial extent

of the object and δz the axial resolution of the system.

The simulation of the superposition of one (Figure A1.a), 50 (Figure A1.b), 100 (Figure A1.c), and 200 (Figure A1.d) optical fields versus the reconstruction distance ($z = 3000\,\mu m$) are shown below. The wavelength range is $\Delta \lambda = 35nm$ ($\lambda_{\min} = 0.565\,\mu m$, $\lambda_{\max} = 0.600\,\mu m$). The digital interference holography apparatus is an off axis holography setup in reflection geometry so all parameters from the graph with significance of distance have to be divided by 2. For the case with one optical field there is no periodicity so I will not give details about this graph (Figure A1.a). For the other cases, the parameters are:

- for N = 50 wavelengths, $\delta k = 0.013\,\mu m^{-1}$, $\Lambda = 242.1429\,\mu m$, $\delta z = 4.8429\,\mu m$.

- for N = 100 wavelengths, $\delta k = 0.0065\,\mu m^{-1}$, $\Lambda = 484.2857\,\mu m$, $\delta z = 4.8429\,\mu m$.

- for N = 200 wavelengths, $\delta k = 0.0032\,\mu m^{-1}$, $\Lambda = 968.5714\,\mu m$, $\delta z = 4.8429\,\mu m$.
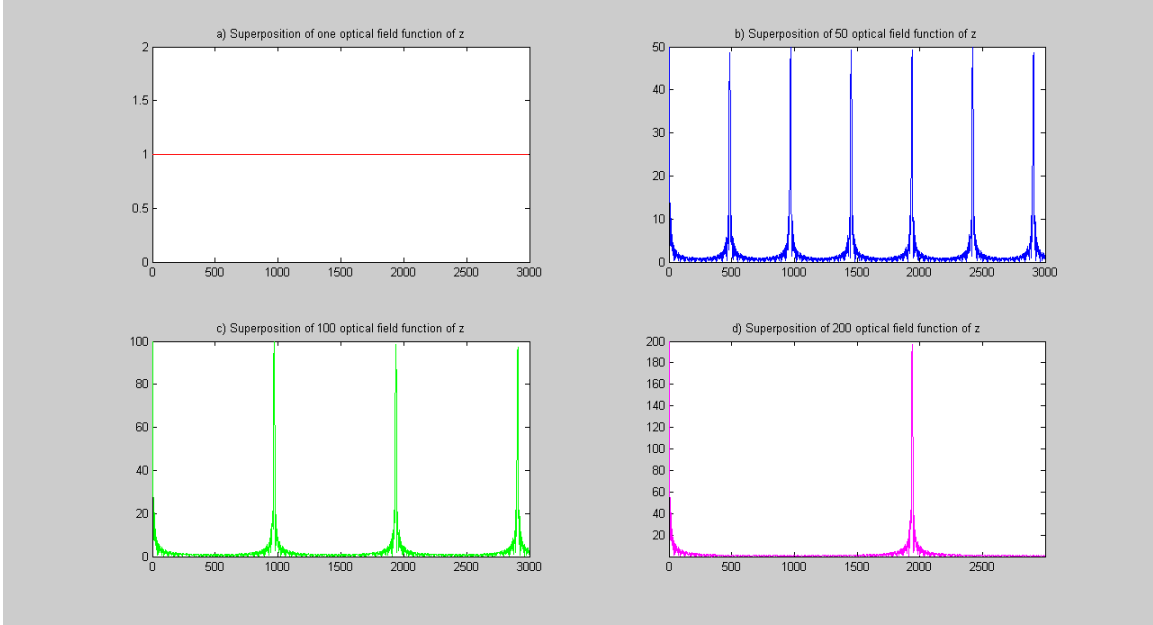
Figure A1. Optical field superposition simulation, $\Delta\lambda = 35nm$; a) One wavelength; b) 50 wavelengths; c) 100 wavelengths; d) 200 wavelengths.

If the wavelength range interval is doubled than before, $\Delta\lambda = 70nm$ ($\lambda_{min} = 0.560\mu m$, $\lambda_{max} = 0.630\mu m$), the width of the pulses are thinner by a factor of two. It means the axial resolution increases by increasing the wavelength range.

Figure A2 shows the optical field superposition $\Delta\lambda = 70nm$. The scanning parameters are:

- for N = 50 wavelengths, $\delta k = 0.0249\mu m^{-1}$, $\Lambda = 126\mu m$, $\delta z = 2.52\mu m$.

- for N = 100 wavelengths, $\delta k = 0.0125\mu m^{-1}$, $\Lambda = 252\mu m$, $\delta z = 2.52\mu m$.

- for N = 200 wavelengths, $\delta k = 0.0062\mu m^{-1}$, $\Lambda = 504\mu m$, $\delta z = 2.52\mu m$.
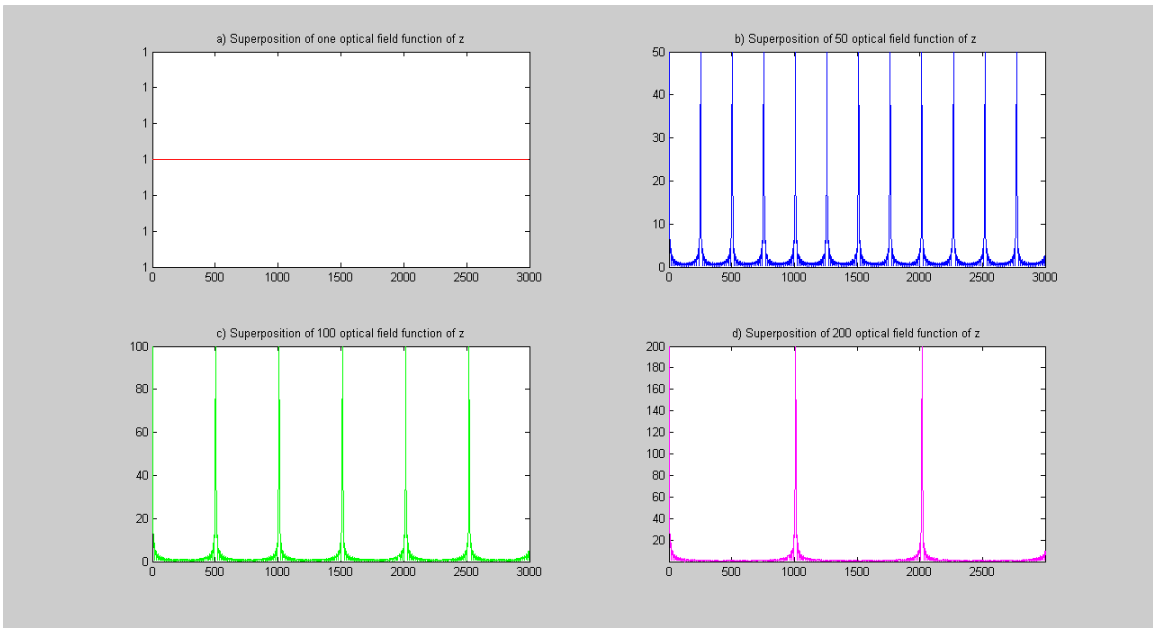
Figure A2. Optical field superposition simulation, $\Delta\lambda = 70nm$; a) One wavelength;

b) 50 wavelengths; c) 100 wavelengths; d) 200 wavelengths.

Appendix B: Diffraction Reconstruction Methods Comparison

This appendix contains two parts. The first part covers the derivation of the Fresnel transform from the angular spectrum of a plane wave. In the second part, the interface of the computer program written in LabView is presented which is used to reconstruct numerically a hologram using the angular spectrum and the Fresnel method.

B1. From the Angular Spectrum to the Fresnel Transform

The optical field can be reconstructed using any reconstruction distance using the angular spectrum method. The accuracy of the Fresnel integral is good to distances close to the aperture (Goodman). Here we want to derive the Fresnel approximation from the point of view of the angular spectrum method starting from the transfer function of propagation through space,

$$H(k_x, k_y) = \begin{cases} \exp[jz\sqrt{k - k_x^2 - k_y^2}] \\ 0 \end{cases} \tag{B1}$$

where the exponential is defined for $\sqrt{k_x^2 + k_y^2} < \dfrac{2\pi}{\lambda}$ and the transfer function is 0 otherwise.

The more usable expression for the Huygens-Fresnel principle needs approximations for the absolute distance $r = \sqrt{x^2 + y^2 + z^2}$, Equation (B2) and for the wavevector along the propagation distance $k_z = \sqrt{k^2 - k_x^2 + k_y^2}$, Equation (B3).

$$\sqrt{x^2+y^2+z^2} = [z^2(1+\frac{x^2+y^2}{z^2})]^{1/2} = z(1+\frac{x^2+y^2}{2z^2}-\frac{x^2+y^2}{4z^2}+.....) \cong z(1+\frac{x^2+y^2}{2z^2}) \quad (B2)$$

$$k^2 = k_x^2+k_y^2+k_z^2, \; k_z = \sqrt{k^2-k_x^2+k_y^2} = k-\frac{k_x^2+k_y^2}{2k}-\frac{k_x^2+k_y^2}{4k_z^2}+.....) \cong k-\frac{k_x^2+k_y^2}{2k} \quad (B3)$$

The optical field at the hologram plane is $E_0(x_0,y_0;z_0)$. A complex field $E_0(x_0,y_0;z_0)$ at a position vector $(x_0,y_0;z_0=0)$ can be decomposed into its spectrum of plane-wave components $A_0(k_x,k_y;0)$ defined by the Fourier transform,

$$A_0(k_x,k_y;0) = \iint E_0(x_0,y_0;z_0)\exp[-i(k_x x_0+k_y y_0)]dx_0 dy_0 \quad (B4)$$

The angular spectrum can then be propagated in space along the z –axis, perpendicular to the hologram plane, multiplying the Equation (B4) by $\exp[ik_z z]$.

$$A_0(k_x,k_y;z) = \exp[i(k-\frac{k_x^2+k_y^2}{2k})z]\iint E_0(x_0,y_0;z_0)\exp[-i(k_x x_0+k_y y_0)]dx_0 dy_0 \quad (B5)$$

The reconstructed complex wave-field $E(x,y,z)$ is found by:

$$E(x,y,z) = \iint dk_x dk_y A_0(k_x,k_y;0)\exp[i(k_x x+k_y y+k_z z)]$$

$$= \iint dk_x dk_y (\iint E_0(x_0,y_0;z_0)\exp[-i(k_x x_0+k_y y_0)]dx_0 dy_0)\exp[i(k_x x+k_y y)+i(k-\frac{k_x^2+k_y^2}{2k})z]$$

$$= \exp(ikz)\iint dk_x dk_y (\iint E_0(x_0,y_0;z_0)\exp[-i(k_x x_0+k_y y_0)]dx_0 dy_0)\exp[-i(\frac{k_x^2+k_y^2}{2k}z-k_x x-k_y y]$$

$$= \exp(ikz)\iint E_0(x_0,y_0;z_0)dx_0 dy_0 \iint \exp[-i(\frac{k_x^2+k_y^2}{2k}z)+ik_x(x-x_0)+ik_y(y-y_0)]dk_x dk_y$$

$$(B6)$$

To solve the exponential integral we need the identity:

$$\int_{-\infty}^{\infty} \exp(iax^2+ibx)dx = \sqrt{\frac{i\pi}{a}}\exp(-\frac{ib^2}{4a}) \quad (B7)$$

where $a = -\frac{z}{2k}$, and $b=(x-x_0)$ or $b=(y-y_0)$. Using this identity, the Equation (B6) becomes,

$$E(x,y,z) = -2\pi \frac{ik}{z} \exp(ikz) \iint E_0(x_0,y_0;z_0) dx_0 dy_0 \exp\left\{ \frac{ik}{2z}[(x-x_0)^2 + (y-y_0)^2] \right\} \qquad \text{(B8)}$$

Developing further this equation we get,

$$E(x,y,z) = -2\pi \frac{ik}{z} \exp(ikz) \exp[\frac{ik}{2z}(x^2+y^2) \iint E_0(x_0,y_0;z_0) dx_0 dy_0 \exp\left\{ \frac{ik}{2z}[(x_0^2 + y_0^2) + 2(xx_0 - yy_0)] \right\}$$

$$= -2\pi \frac{ik}{z} \exp(ikz) \exp[\frac{ik}{2z}(x^2+y^2) \mathcal{F}\left\{ E_0(x_0,y_0;z_0) \exp[\frac{ik}{2z}(x_0^2 + y_0^2)] \right\}[k_x,k_y]$$

$$\text{(B9)}$$

As a conclusion, we obtained the optical field based on the Fresnel approximation from optical field based on the angular spectrum method. The two optical fields are identical within the approximations (B2) and (B3).

B2. Diffraction Reconstruction Methods. Computer Main Screen.
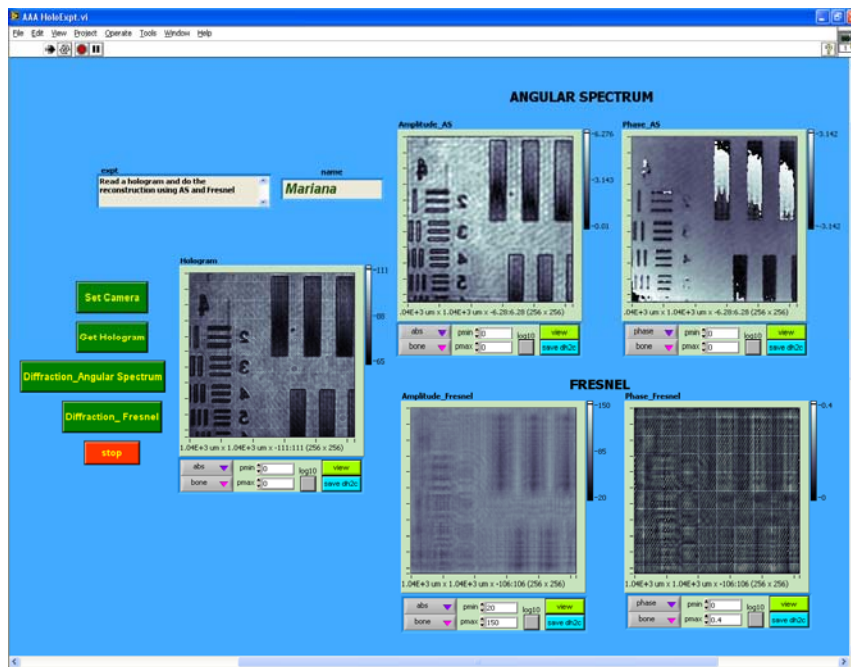
Figure B.1: Main screen of diffraction reconstruction methods Labview program.

Appendix C: Fourier Transform

FOURIER TRANSFORM

If f(x) is a reasonably well-behaved function, then

$$f(x) = \frac{1}{\sqrt{2\pi}} \int_{-\infty}^{\infty} F(k) \exp(ikx) dk$$

$$F(k) = \frac{1}{\sqrt{2\pi}} \int_{-\infty}^{\infty} f(x) \exp(-ikx) dx$$

$$F(k) = \mathcal{F}\{f(x)\}[k] \qquad f(x) = \mathcal{F}^{-1}\{F(k)\}[x]$$

FOURIER SERIES

If f(x) is a periodic function of period Λ, then

$$f(x) = \sum_{n=-\infty}^{\infty} F_n \exp(inKx)$$

$$F_n = \frac{1}{\Lambda} \int_0^{\Lambda} f(x) \exp(-inKx) dx$$

where $K \equiv \dfrac{2\pi}{\Lambda}$ is the fundamental frequency.

DISCRETE FOURIER TRANSFORM

f(x) defined in [-X/2, X/2]: $\qquad f(x) = 0$ for $x \notin \left[-\dfrac{X}{2}, \dfrac{X}{2}\right]$

$f_s(x)$ sampled at δx intervals: $\qquad f_s(x) = f(x) \cdot \text{comb}\left(\dfrac{x}{\delta x}\right)$

i.e., $f_s(x_i) = f(x_i)$ for $x_i \in \left[-\dfrac{X}{2} : \delta x : \dfrac{X}{2}\right]$
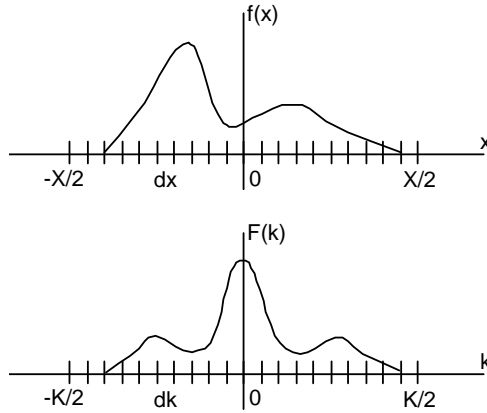
Fourier transform $F_s(k)$:

$$F_s(k) = F\ \{f_s(x)\}[k] = F\ \left\{ f(x) \cdot \text{comb}\left(\frac{x}{\delta x}\right) \right\}$$

$$= F(k) \oplus \frac{\sqrt{2\pi}}{\delta x} \text{comb}\left(\frac{k}{2\pi / \delta x}\right) = \frac{\sqrt{2\pi}}{\delta x} \sum_{n=-\infty}^{\infty} F\left(k - n\frac{2\pi}{\delta x}\right)$$

Therefore, if $F(k) = 0$ for $k \notin \left[-\frac{K}{2}, \frac{K}{2} \right]$, where $K = \frac{2\pi}{\delta x}$, then

$$F_s(k) = F(k) \ \text{for} \ k \in \left[-\frac{K}{2}, \frac{K}{2} \right]$$

Conversely:

F(k) defined in [-K/2, K/2]: $F(k) = 0$ for $k \notin \left[-\frac{K}{2}, \frac{K}{2} \right]$

$F_s(k)$ sampled at δk intervals: $F_s(k) = F(k) \cdot \text{comb}\left(\frac{k}{\delta k}\right)$

Fourier transform $f_s(x)$: $f_s(x) = f(x) \oplus \frac{\sqrt{2\pi}}{\delta k} \text{comb}\left(\frac{x}{2\pi / \delta k}\right)$

Therefore, if $f(x) = 0$ for $x \notin \left[-\frac{X}{2}, \frac{X}{2} \right]$, where $X = \frac{2\pi}{\delta k}$, then

164

$$f_s(x) = f(x) \text{ for } x \in \left[-\frac{X}{2}, \frac{X}{2} \right]$$

Therefore, if both f(x) and F(k) are discretized with N+1 points, then:

$$
\begin{cases}
K = N\delta k = N\dfrac{2\pi}{X} = \dfrac{2\pi}{\delta x} & \delta k = \dfrac{K}{N} = \dfrac{2\pi}{N\delta x} = \dfrac{2\pi}{X} \\[2ex]
X = N\delta x = N\dfrac{2\pi}{K} = \dfrac{2\pi}{\delta k} & \delta x = \dfrac{X}{N} = \dfrac{2\pi}{N\delta k} = \dfrac{2\pi}{K}
\end{cases}
$$

DIRAC DELTA FUNCTION PROPERTIES

$$\int_{-\infty}^{\infty} \delta(x - x_0)\,dx = 1$$

$$\int_{-\infty}^{\infty} f(x)\delta(x - x_0)\,dx = f(x_0)$$

$$\delta(\alpha x) = \frac{1}{|\alpha|}\delta(x)$$

$$\delta(-x) = \delta(x)$$

Appendix D: Digital Interference Holography Computer Interface

This appendix contains a few computer programs, for digital interference holography, written in Labview. The main Digital Interference Holography computer interface (Figure D.1) has designated buttons and each of them performs specific functions. They are:

- **set mike**, the micrometer setup which is used for the calibration

- **Holo EE,** the reconstruction of a hologram using the angular spectrum method

- **set camera**, the camera setting

- **ws HHH**, which is used to acquire holograms from the IMAQ CCD camera for each wavelength in the wavelength range.

- **DIH calc**, which has the option to perform/ not to perform the phase-matching correction, does the optical field superposition, and saves the stack of holograms.

- **DH View** which is used to visualize various image files already saved.
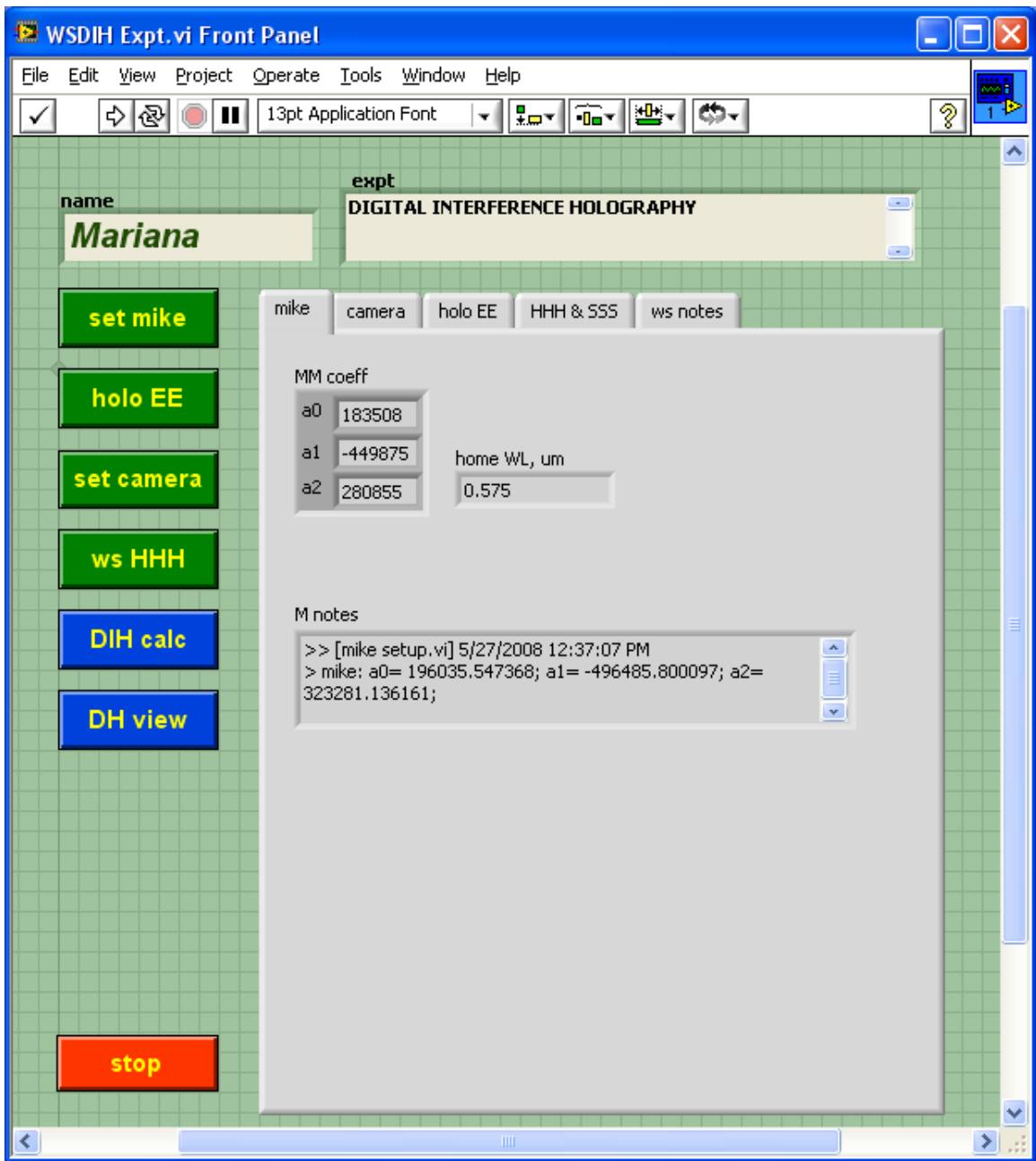
Figure D.1: Main screen of Digital Interference Holography Labview program.
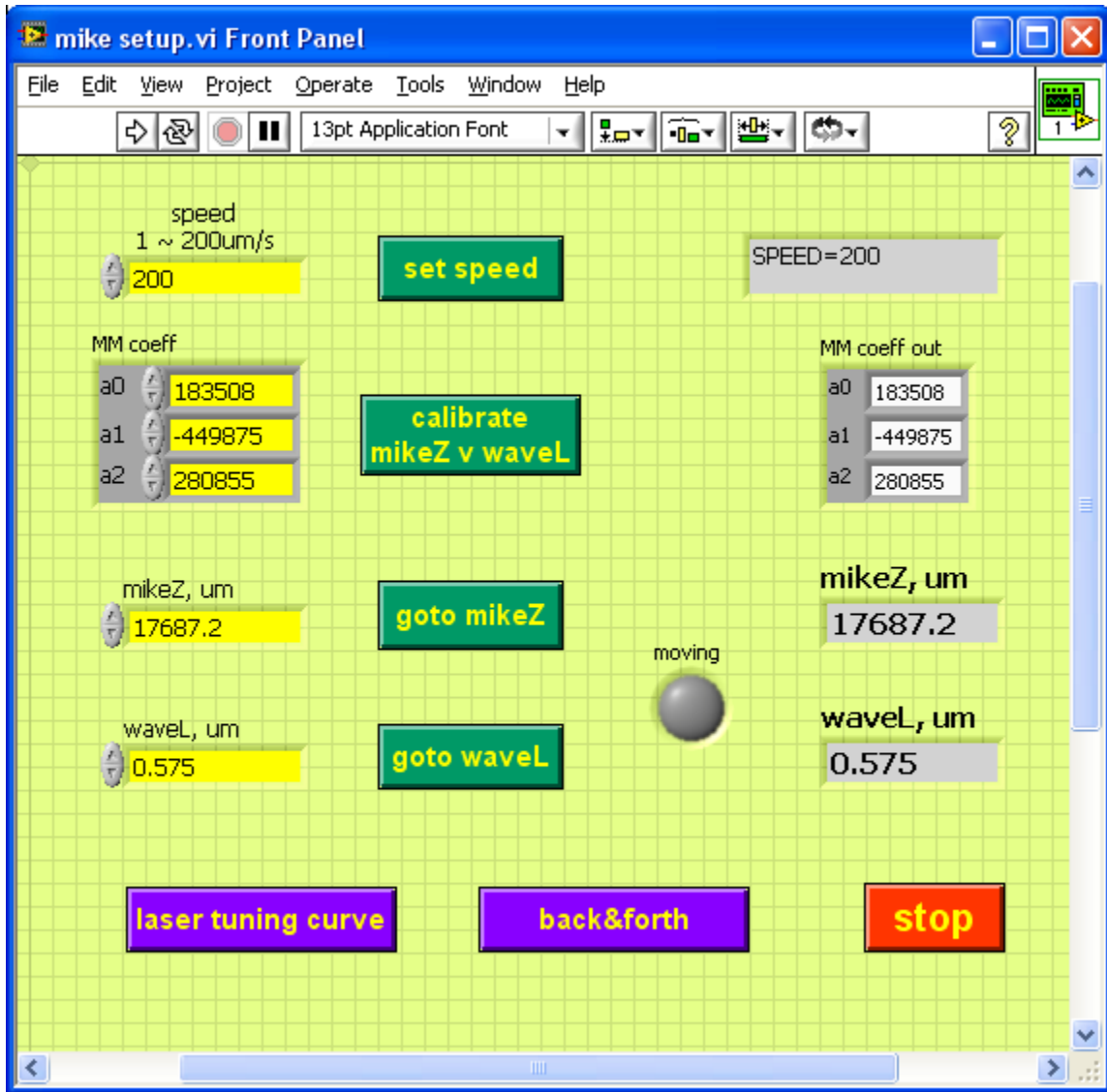
Figure D.2: Calibration via micrometer controller.
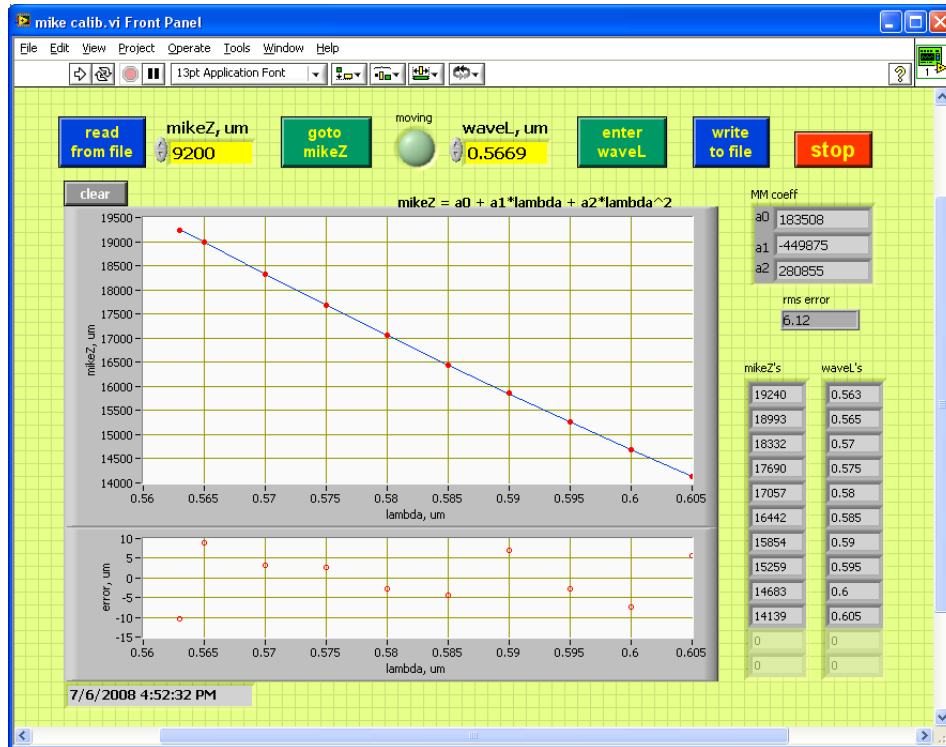
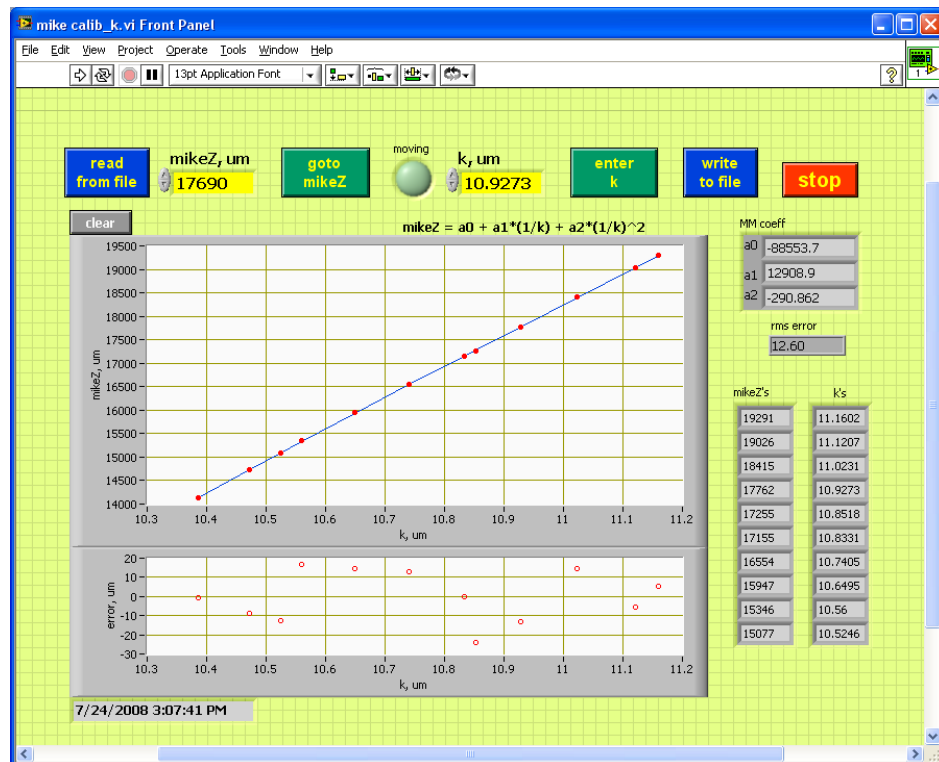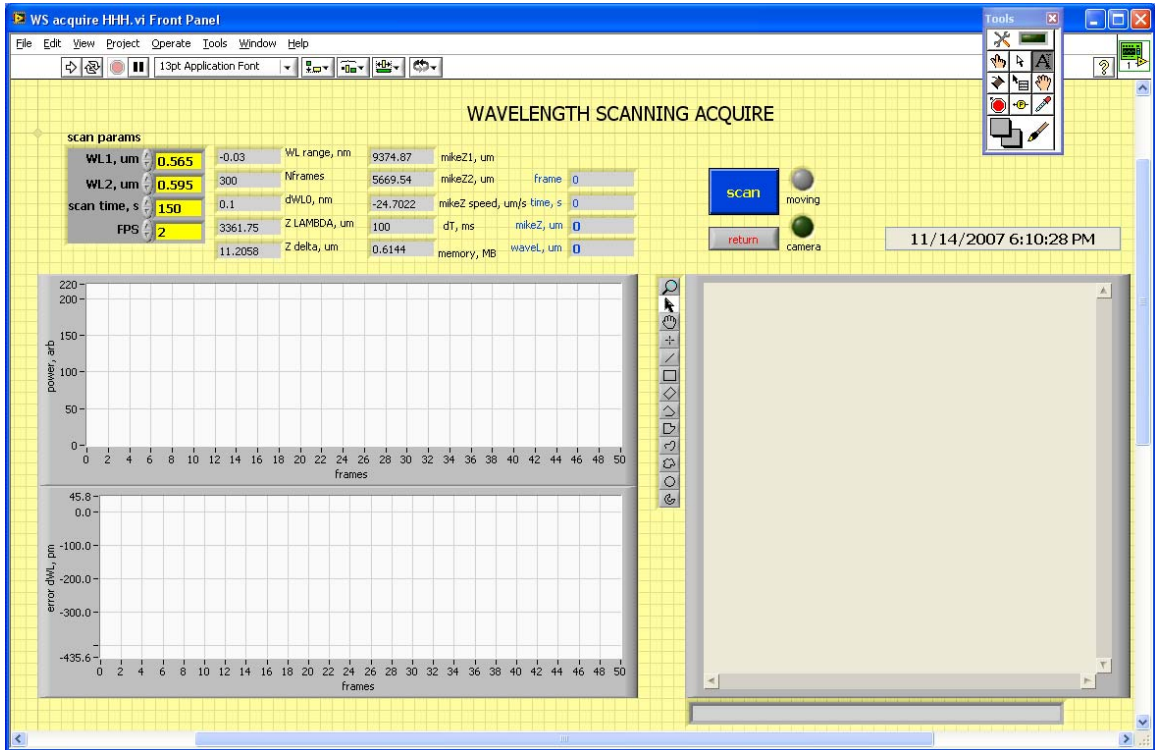**Figure D.3:** Calibration curve, micrometer position versus wavelength.

Figure D.4: Calibration curve, micrometer position versus wavevector.

Figure D.5: Digital interference holography, holograms acquisition from the IMAQ
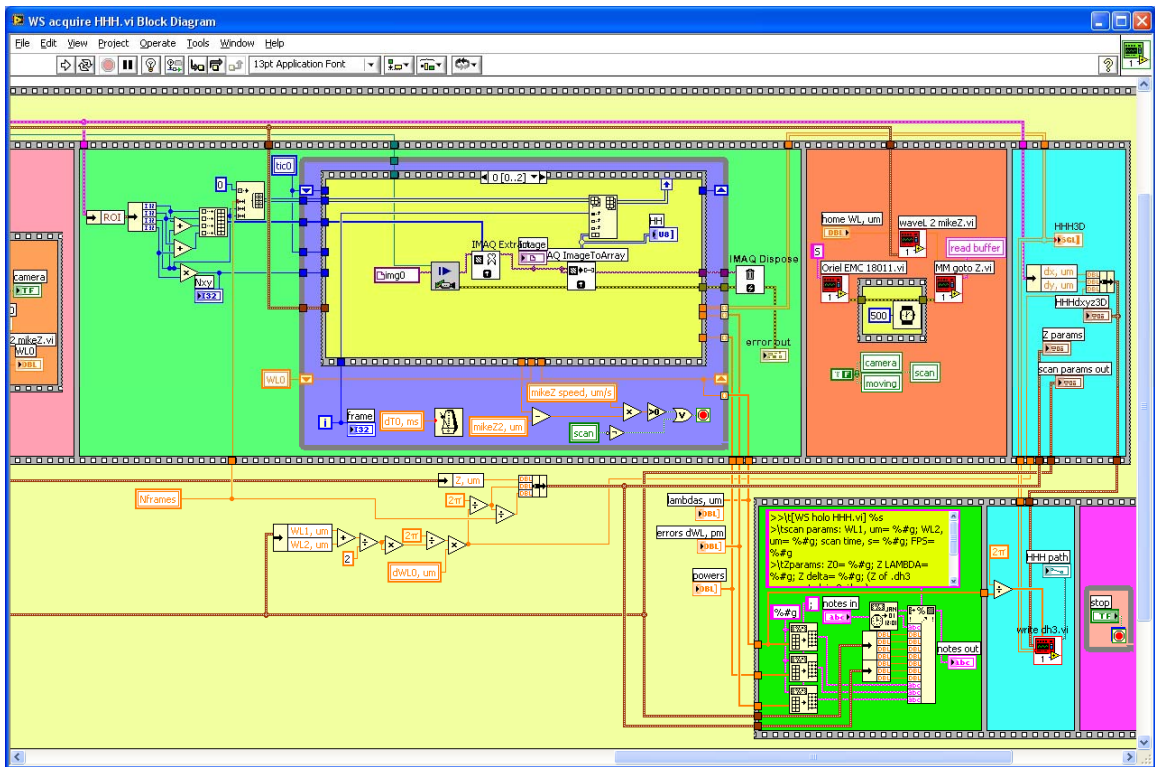
CCD camera

.

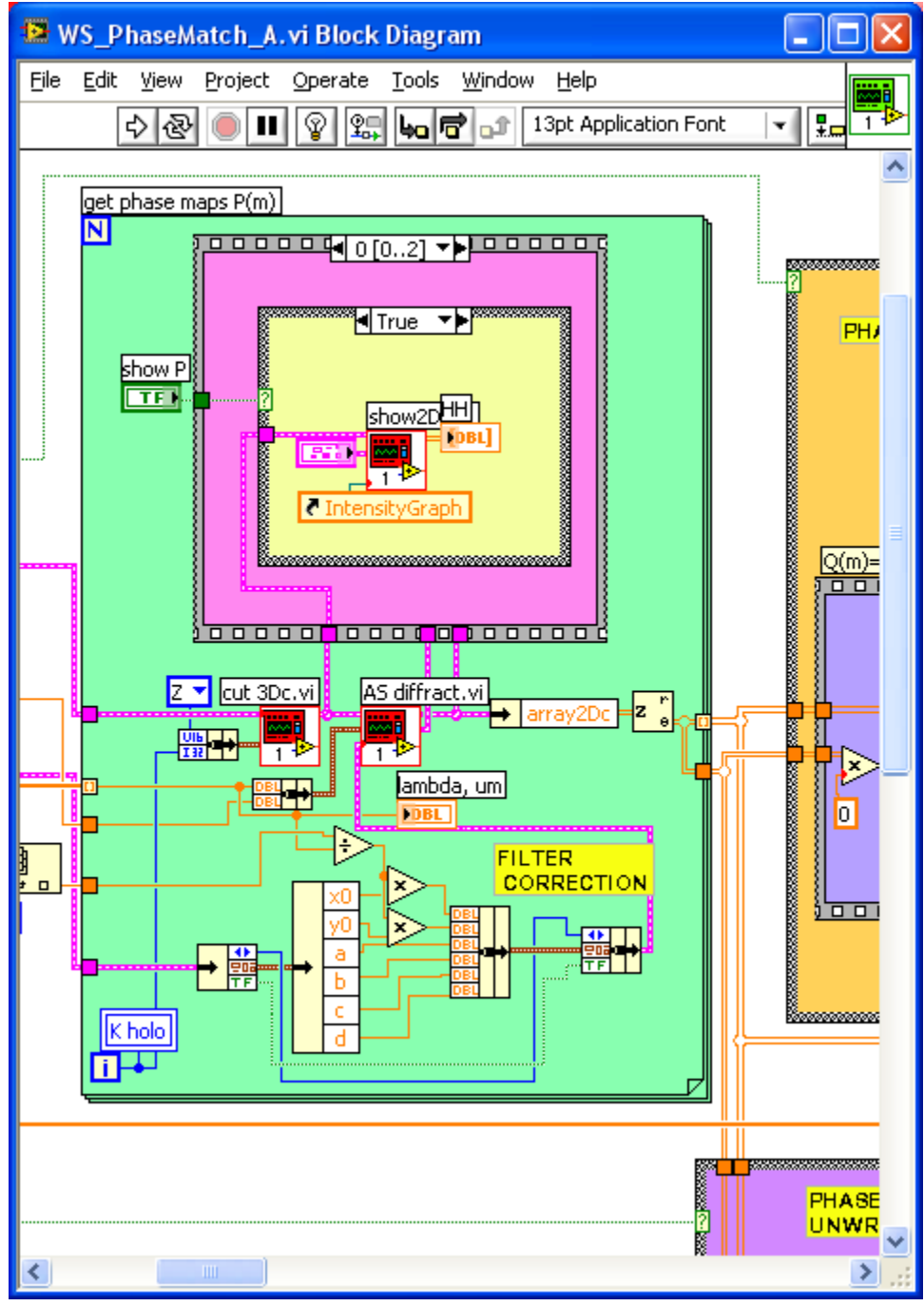**Figure D.6:** Holograms acquisition. Block Diagram.

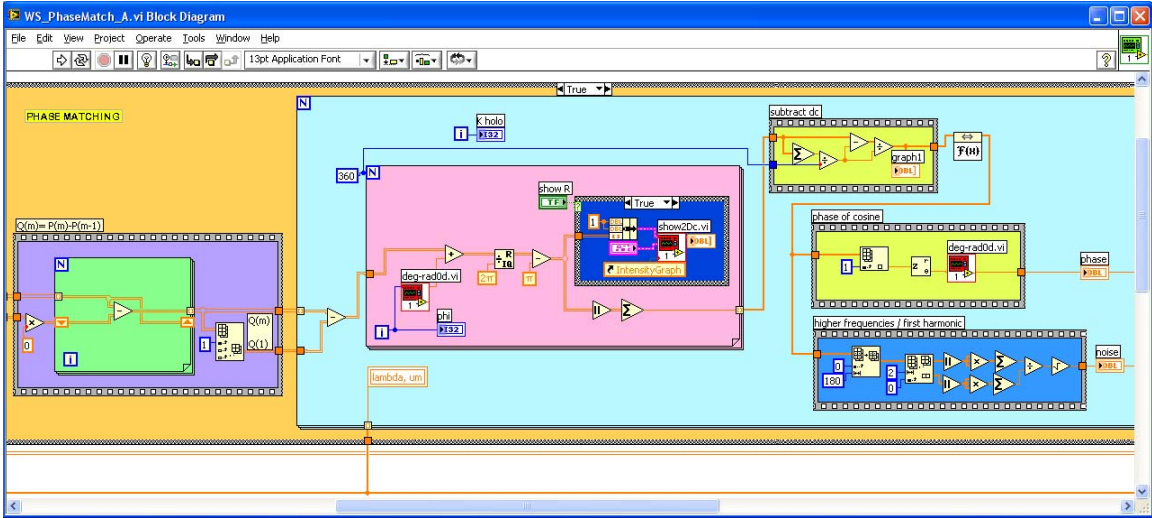**Figure D.7:** Phase-match, Filter correction. Block Diagram.

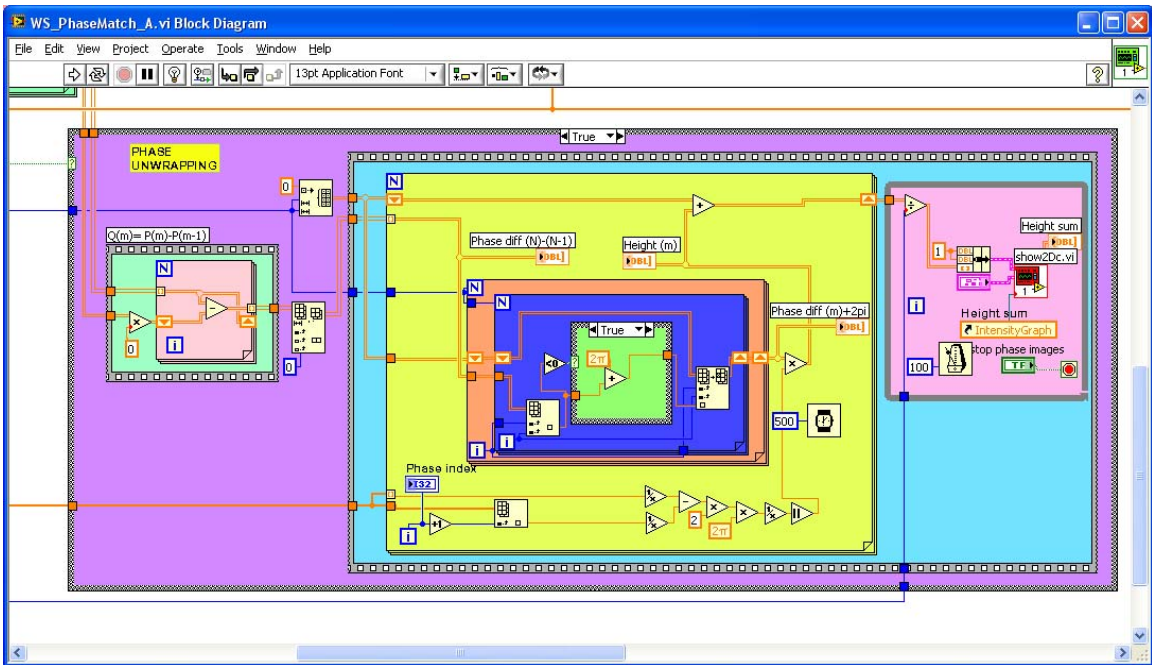**Figure D.8:** Phase-unwrapping using DIH. Block Diagram.



Figure D.9: Phase-unwrapping using DIH. Block Diagram.

Appendix E: Brownian Motion and Optical Trapping Computer Interface

This appendix contains selected computer programs, for Brownian motion and optical trapping, written in Labview. The main computer interface functions are:

- **set camera**, the camera setting

- **Reconstruction distance,** the reconstruction of a hologram using the angular spectrum method

- **Get holograms**, which is used to capture holograms from the IMAQ CCD camera for a time interval.

- **EE Rec**, has two option, to performs individual hologram reconstruction, and to perform hologram differences for particle tracking. In both cases the results are saved at the end.

- **Gabor View** which is used to visualize various image files already saved.
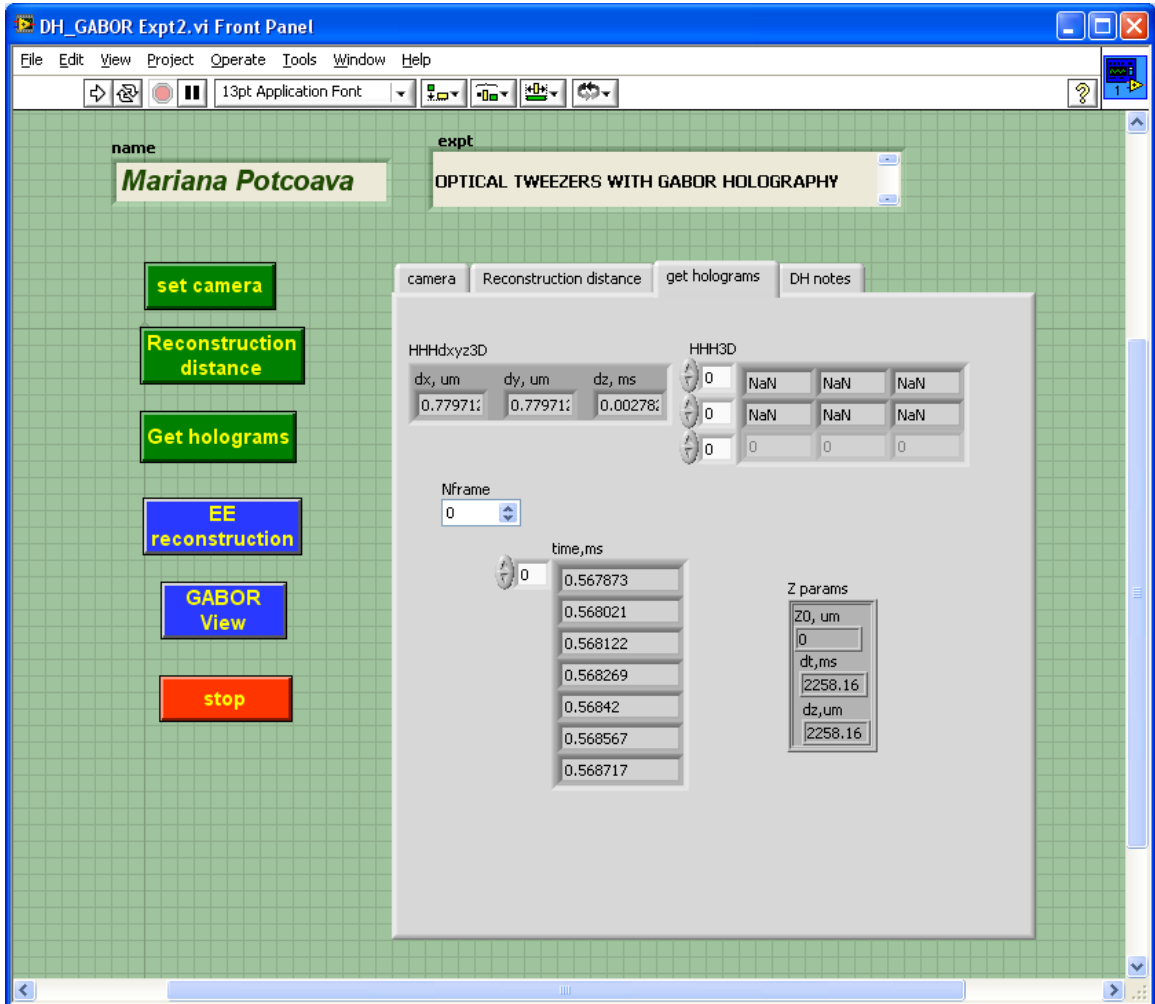
Figure E.1: Main screen of Brownian motion and optical trapping Labview

program.
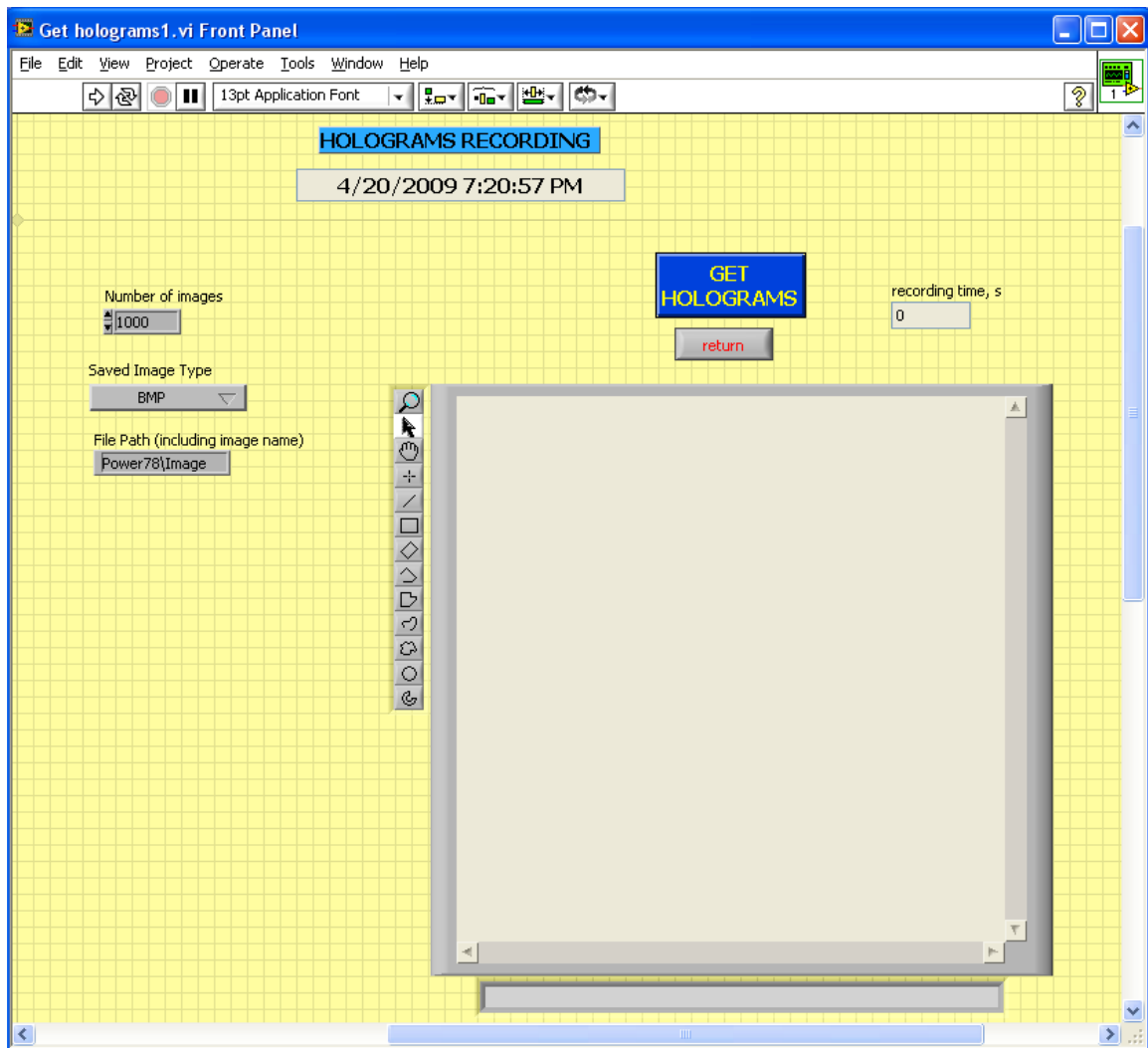
Figure E.2: Brownian Motion and Optical Trapping, holograms acquisition from

the IMAQ CCD camera.
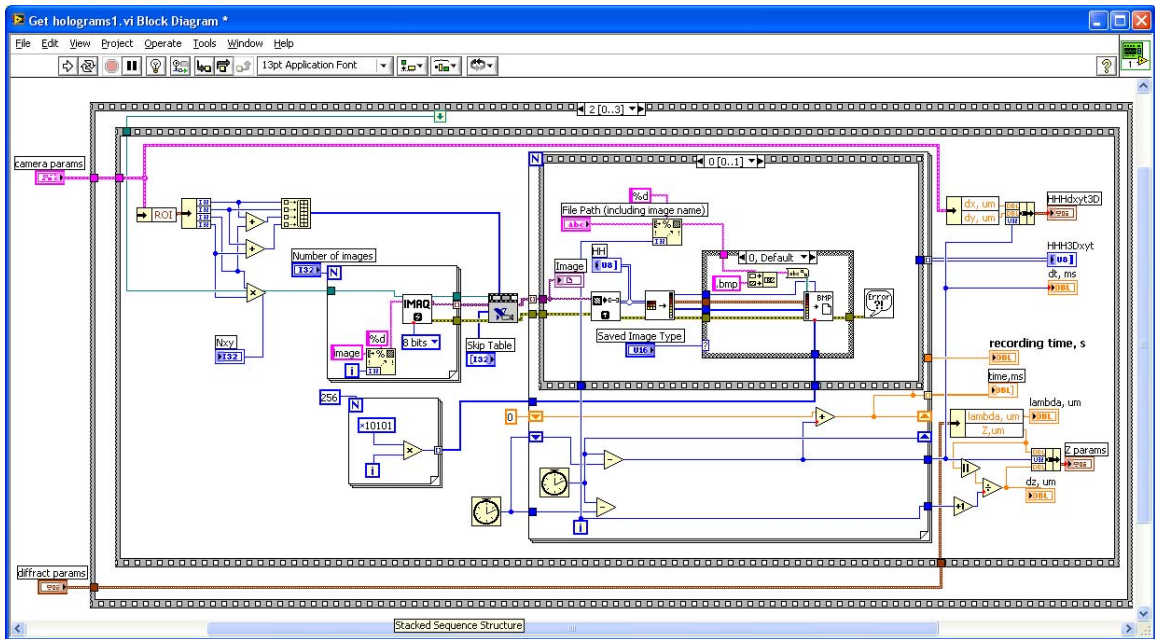
Figure E.3: Sequence acquisition of multiple holograms. Block Diagram.

Appendix F: List of Accomplishments

REFEREED PUBLICATIONS

- M. C. Potcoava and M.K. Kim, "Optical tomography for biomedical applications by digital interference holography" Meas. Sci. Technol. Vol. 19**,** 074010 (2008).

- M. C. Potcoava, C. N. Kay, M. K. Kim, and David W. Richards, "Digital Interference Holography in Ophthalmology", Journal of Modern Optics. (Accepted).

- M.K. Kim and M. C. Potcoava, "Fingerprint Biometry Applications of Digital Interference Holography", Applied Optics (In Review).

- M. C. Potcoava, L. Krewitza and M.K. Kim, "Brownian motion of optically trapped particles by digital Gabor holography" (To be submitted to Optics Express).

PROCEEDINGS

- M. C. Potcoava and M.K. Kim, "Fingerprints scanner using Digital Interference Holography ", in Biometric Technology for Human Identification VI, (SPIE Defense, Security, and Sensing 2009), paper presentation 7306B-80.

- M. C. Potcoava, M. K. Kim, Christine N. Kay, "Wavelength scanning digital interference holography for high-resolution ophthalmic imaging", in Ophthalmic Technologies XIX, (SPIE 2009 BiOS), paper presentation 7163-10.

CONFERENCES

- M. K. Kim and M. C. Potcoava, "Fingerprint Biometry Applications of Digital Holography and Low-Coherence Interference Microscopy" in Digital Holography and Three-Dimensional Imaging, Optical Society of America, Vancouver CA, 2009.

- M. C. Potcoava and M.K. Kim, "Fingerprints scanner using Digital Interference Holography ", in Biometric Technology for Human Identification VI, SPIE Defense, Security, and Sensing , Orlando FL, 2009, paper presentation 7306B-80.

- M. C. Potcoava, M. K. Kim, C. N. Kay, "Wavelength scanning digital interference holography for high-resolution ophthalmic imaging", in Ophthalmic Technologies XIX, SPIE BiOS, San Jose CA, 2009, paper presentation 7163-10.

- C. N. Kay, M. C. Potcoava, M. K. Kim, D. W. Richards, "Digital Holography Imaging of Human Macula", Florida Society of Ophthalmology Resident Symposium. Palm Beach, FL, 2008, paper presentation (Second place).

- M.C. Potcoava, C.N. Kay, M.K. Kim, D.W. Richards." Digital Interference Holography in Ophthalmology", ARVO, Fort Lauderdale, 2008, paper presentation 4011.

- M. C. Potcoava and M. K. Kim, "3-D Representation of Retinal Blood Vessels through Digital Interference Holography," in Digital Holography and Three-Dimensional Imaging, OSA, San Petersburg FL, 2008, paper presentation DMB2.

- M. C. Potcoava and M. K. Kim, "Animal Tissue Tomography by Digital Interference Holography," in Adaptive Optics: Analysis and Methods/Computational Optical Sensing and Imaging/Information

Photonics/Signal Recovery and Synthesis Topical Meetings, OSA Technical Digest OSA, Baltimore MD, 2007), paper presentation DWC6.

- M. C. Potcoava,"Digital Interference Holography in the 21 st Century", USF Graduate Research Symposium, Tampa FL, 2008, poster presentation, (First Place).

- M.C. Potcoava, C.N. Kay, M.K. Kim, D.W. Richards, P. R. Pavan, "Digital Holography Imaging of Human Macula", ASRS, Maui HI, 2008), poster presentation.

About the Author

Mariana Potcoava received a Bachelor's Degree in Physics from Bucharest University in 1994, a M.S. in Photonics from Politechnica University Bucharest in 1997 and another M. S. in Atmosphere Science in 2003 from University of Michigan. She entered the Ph.D program in Applied Physics at the University of South Florida in Fall 2004.

She has completed an Industrial Practicum at Imaging Eyes, Orsay France as part of the Applied Physics practical training.

While in the Ph.D. program at the University of South Florida, Ms. Potcoava presented her work in numerous technical conferences, such as OSA, SPIE, ARVO, and published the results of this dissertation in various academic journals including Measurements Science Technology Modern of Journal Optics, Applied Optics, and Optics Express.